MODELING OF THIN POLYMER FILMS

Maria Serral Serra

Dipòsit Legal: T 1011-2015

MODELING OF THIN POLYMER FILMS

BY

Maria Serral Serra

Supervised by Dr. Josep Bonet Ávalos

Molecular Simulation Group
Departament d'Enginyeria Química
Escola Tècnica Superior d'Enginyeria Química

Submitted to the Doctorate School
for the degree of Doctor of Philosophy

Universitat Rovira i Virgili

Tarragona May 2015

Avinguda dels Països Catalans,26
Campus Sescelades
43007 Tarragona (Espanya)
Tel. +34 977 559 603
Fax. +34 977 559 655

Declaration

I declare that the present study entitled "Modeling of Thin Polymer Films", presented by Maria Serral Serra for the award of the degree of Doctor, has been carried out under my supervision at the Department of Chemical Engineering of this university, and it fulfills all the requirements to be eligible for the International Doctorate Award.

Signature:

Dr. Josep Bonet Ávalos

Tarragona, May 2015

Abstract

This work is focused on the study of two different systems of thin polymeric films. In the first place, the viscoelastic response of multilayer polymeric films (sandwiches) of linear low-density polyethylene (LLDPE) and ethylene vinyl alcohol (EVOH) copolymer has been experimentally analyzed through dynamic mechanical analysis. We propose an equation to predict the mechanical response of the sandwich films from the data experimentally obtained for the monomaterial films. The equation is a *mixing rule* based on the hypothesis that the layers independently contribute to the final response and that there are no interfacial effects. The predictive character of the equation permits us to conclude that the response of the sandwich does not significantly depend on the individual layer thickness but only on the volume fraction of the EVOH in the system. More important, we find a strong sensitivity of the response to the processing conditions, which we quantitatively describe.

Based on the previous analysis, we have additionally proposed a more mesoscopic model for the viscoelastic response of the solid LLDPE and EVOH films and sandwiches. The model is formally a Generalized Maxwell (GM) model, which corresponds to a mechanical analog of the complex response of the material. The fitting of the model to the viscoelastic response for different temperatures allows us to obtain information on the spectra of relaxation times, which, to some extend, bear information on the microscopic structure of the system. In the first place, we have compared the spectra of bars and films of pure components, to see what is the effect of the processing in the individual spectrum of relaxation-times when passing from bars to films. We have also compared the response of the sandwich films with the one of the pure films, in agreement with the mixing rule previously described. We have checked that properly mixing the spectra of the pure films we recover the observed spectra for the sandwiches and tried to infer specific features of sandwiches. In particular, due to the fact that the GM model was unable to produce a good fitting of the experimental data and due to the assumed non-equilibrium conformation of the samples because of the processing, we have developed from scratch a nonlinear correction to the viscoelastic response, in the spirit of Eyring theory. This development includes the calculation of the corrections but also the identification of the physically relevant form of the corrections to the storage and loss moduli. With the addition of the nonlinear corrections, we find a quantitative

very good agreement with the experimental data. The spectra of the corrective terms are difficult to interprete, but at least indicate us which modes are mostly affected by the processing, due to the fact that these corrections are not required for materials processed in bars.

Finally, we have also studied a completely different system, with completely different techniques. This second system studied consists of films of sphere-forming diblock copolymers under external influences. Using mesoscale simulations based on the Otha-Kawasaky theory, which, has its roots on the Cahn-Hilliard theory of spinodal decomposition, we investigate the structure of sphere-forming diblock copolymers in thin films on chemically patterned surfaces. The numerical implementation of the technique on a lattice system is referred to as Cell Dynamics Simulation (CDS). CDS allows us to analyze events whose time-scale is too long to be described by classical molecular dynamics simulations. Hence, using 3-Dimensional CDS we demonstrate that on patterned surfaces, in the form of chemically attractive parallel stripes, arrays of spherical domains, with long-range order, can be obtained. However, this long-range order depends on the commensurability of the structure with both the band periodicity and slit thickness. The analysis indicates that there exists an inherent simplicity in the system due to the fact that its behavior seems to depend upon one single length d, which characterizes the distance between spherical domains. The comparison of the simulation results with experimental data shows an almost quantitative agreement between both, if the characteristic distance between mesophases, d, is used as the only scale. Furthermore, we show that the proper selection of the band periodicity and, consequently, of the film thickness, permits the system to switch from a hexagonal packing to a body-centered orthohedron. Therefore, we show a way to control the formation of long-range ordered structures of different types in this kind of systems.

Agraïments

Per començar vull posar de manifest el meu enorme agraïment al Dr. Josep Bonet Ávalos, per haver-me presentat ja fa uns anys l'apassionant ciència dels polímers, per haver-me ofert la possibilitat de desenvolupar la tesi doctoral en aquest camp, per haver confiat en mi i, finalment, per ser un gran mestre el qual considero que ha contribuït en el meu enriquiment científic, professional i també personal.

Vull mostrar la meva gratitut als membres del grup *Molecular Simulation*, especialment al Dr. Allan Mackie pel seu suport, i als meus companys de l'aula pont, entre ells en Sisco amb qui he tingut el plaer de compartir una pila d'anys i experiències a la universitat; així com a la Teresa pel seu el suport, pels seus consells i per transmetre'm en tot moment el seu optimisme. A la Dolors, la Núria i la Merche també els vull agraïr la seva amabilitat i la seva assistència des del Departament.

I would like to thank now Dr. Peter Sandkühler, Felip Vidiella and Marc Mangnus from Dow Chemical. They relied on us to solve an industrial problem, they provided us with proper experimental data, and finally they had a very meaningul implication in the project by conferring us a broader and more practical viewpoint.

Furthermore, I am very grateful with the hosts I had during the *PhD* stay in the Computational Physics group in the *University of Central Lanchashire* in Preston, specially with Prof. Andrei Zvelindovsky and Drs. Marcos Pinna and Manuela Mura. They offered me the possibility to work in their amazing research topic, the block-copolymers, which was new for me, and they introduced me to the basic physics of it.

Also, I want to thank the members of the thesis committee for having accepted to evaluate my thesis and being present in my thesis defence.

Per acabar, vull agraïr a totes les persones que durant aquest quatre anys han estat al meu costat, als que han estat els meus companys de pis, als meus companys de doctorat Irene, Valentin, Albert i David, i a les meves molt bones amigues de Sarral. A la meva parella a qui, de fet, he conegut gràcies al doctorat i qui s'ha convertit en un company imprescindible en la meva vida. Finalment, vull expressar la meva infinita gratitud a la meva familia, als meus pares i la meva germana Marta, d'ells rebo un encoratjament continu i això em fa sentir capaç de fer qualsevol cosa, probablement no són conscients que sense ells no em trobaria en aquest punt avui, moltes gràcies.

Contents

List of Figures

List of Tables

Chapter 1

Introduction

Polymers are widely used since their abrupt irruption in the middle of the 20th century, mainly because of the easy processability and attractive mechanical properties. As versatile materials, they can exhibit a wide range of properties such as rigidity or flexibility, ductility, elasticity, lightness as well as interesting optical and transport properties. Therefore, they are used not only in the development of new technologies, but also in our daily life, in which they have become indispensable materials. Current uses range from packaging and coating to textile, structural materials, electronic and medical devices as prostheses, among an innumerable quantity of applications.

Polymers can be processed in multiple ways and one of the most common formats are thin films, which are present also in a vast range of applications. Moreover, due to the rich variety of phenomena taking place in thin films as compared to the bulk, the description and comprehension of the underlying physics of that kind of systems is considered a research field itself. A complex interplay between the molecular structure, the processing, and the system geometry is what ultimately determines the performance of thin polymeric films. A good knowledge of the latter factors would allow designing an optimized manufacturing process to obtain materials with characteristics specifically oriented to the final application requirements. Additionally, the optimization of the design and the processes should allow the reduction of the consumption of raw materials and energy, which is one of the main goals of the industry nowadays.

In the present work, we focus our interest on two rather different types of polymer films that, correspondingly, are used for quite different applications. These are, in the first place, solid polymer films oriented towards more efficient packaging applications.

In the second place, films of sphere-forming block copolymers, with the aim put on nanotechnology applications. Due to their different nature and objective, a different methodology has been applied in each case. Despite of being rather different systems, both of them share the common characteristic of being affected by the confinement, and our final purpose, then, is to get a better knowledge on the basic consequences of the constraints imposed to the systems by the confinement.

First of all, there is a constantly increasing demand of polymeric films with enhanced properties for packaging. Conventionally, monolayer films and *coextruded* polymer films have been provided by the plastic industry for this purpose. The coextruded films consist of, at least, two different polymers, with different properties that one wishes to combine, which are extruded together giving films with 3 to 9 layers. These coextruded films present improved but also tailored properties as compared with monolayer films. However, it has been observed that if the thickness of each layer is reduced two or three orders of magnitude, through the so-called *multilayer technology*, further options for differentiation in the performance of the material exist. The multilayer technology consists of the conventional coextrusion unit followed by a series of multiplying die elements, giving rise to a forced-assembly of stacks of layers that can contain from four to thousands of individual layers[85,103]. The key technical hypothesis is that multilayer films can yield effective properties that are notably different from those of the pure constituents. Such an effect is related to internal structural changes that can be attributed either to the confinement of the polymer chains, the constrained growth of microscopic crystalline structures, the incidence of the interface between species, and the influence of the processing conditions, among others. The understanding of the role played by all these elements would allow a design of multilayer films, with new tailored properties, by modifying their architecture through the combination of different kind of polymers, the composition ratio between them, the number of layers and their thicknesses, as well as the flow conditions during their fabrication.

Up to date, the research on multilayer films has been approached mainly from the experimental side, particularly by characterizations of the morphology and the properties of the systems[11,12,56,59,85,93,99,115,134]. However, little has been done with regard to the theoretical description of their mechanical properties. Here, we will approach this general problem by using data of an observable mechanical property

(macroscopic), namely, the linear viscoelasticity. The analysis of this property will lead us to a certain knowledge of the internal mophology (microscopic) of *sandwich* films obtained by means of the modeling of the properties.

The systems, whose linear viscoelastic properties are studied in this work, are functional multilayer films of ethylene vinyl alcohol copolymer (EVOH) embedded in linear low-density polyethylene (LLDPE), with different relative compositions of the constituents and different overall film thicknesses. Particularly, these two specific polymers are chosen because they are commonly combined in food packaging applications. LLDPE is a ductile and tough material that shows excellent structural properties such as sealability, tear and impact resistance, as well as good optical properties and moisture resistance. In turn, EVOH is a widely used material for its excellent properties as gas barrier and resistance to organic molecules[55]. This latter material has higher elastic modulus and is less tough and ductile than LLDPE.

The microscopic structural changes experienced by multilayer films are mainly related to the hindered growth of the three-dimensional isotropic spherulites, which semicrystalline polymers, such as LLDPE and EVOH, develop in bulk[43]. Lamellae are plate-like crystals of polymer formed by the wiggling of the chains, forming parallel segments of the order of 100 monomers. In a bulky material, these lamellae grow into the aforementioned suprastructures named spherulites. Under confinement the lamellae adopt a different organization giving rise to much more microscopically anisotropic material, giving rise to discoids (or flattened spherulites) or single lamellae crystals, instead of spherulites, as a result of decreasing the system thickness down to the micro- or nanometer scale[1,25,87,92]. These changes have an effect on the viscoelastic properties and can be detected when comparing the relaxation response between bulky polymers and thin films. Experimentally, dynamic mechanical analysis (DMA) is used, among others, to study relaxation properties[17,18]. In particular, DMA is very sensitive to the motions of different segments of polymer chains and it is a good tool to detect dynamic transitions in solid polymers[72,84]. Regarding these transitions, in general one can distinguish between the glass transition, which involves motions of relatively large segments of the polymer chain, and secondary transitions, which occur, in contrast, due to more localized motions. Hence, the observation of the transitions provides details on the influence of the polymer structure on the thermo-mechanical behavior of the

system. This is due to the fact that the molecular motions, activated when passing through a transition, affect the overall mechanical and physical properties[70]. In our work, the linear-viscoelastic behavior is evaluated through DMA in a wide range of temperatures of practical use, for both, pure LLDPE and EVOH in compression moulded bars, monomaterial films of the same components, and multilayer LLDPE/EVOH films of different layer thicknesses.

The most interesting feature encountered during the analysis of the multilayer films is that their viscoelastic behavior can be directly related to the ones of pure LLDPE and EVOH constituents, through a simple mixing rule, despite the complexity of the viscoelastic response. Having a model for the response of the multilayer film has brought us to the second interesting, i.e. that the miximg rule can only be used when the processing conditions for the films of pure components and sandwich are the same (same extruding unit and draw ratio). Evidently, the extra knowledge introduced by the model allows us to state that the processing conditions are strongly modifying the response of films through significant microscopic structural changes. We also come to the conclusion that for, the systems under study, the influence of the processing conditions is by far more relevant than the effects due to the confinement or interfaces between the two polymer species.

Beyond the statement of the mixing rule, we have also attempted the analysis of the properties of these systems through the application of a viscoelastic model to be fitted to the experimental data. The spectrum of relaxation-times obtained as a result of this fit brings additional information of rather microscopic origin, which is interesting by itself. Mechanical analogs have been traditionally used to build the necessary viscoelastic models. For example, one finds in the specialized textbooks the simple Maxwell and Kelivn-Voigt models. However, one also finds multi-element models, which try to capture the viscoelastic response in a more realistic way. These latter models are based on the hypothesis that the mechanical response can be described as a superposition of elements each with their own characteristic relaxation-time[137].

In this work we have chosen the multi-elements approach, in the form of the so-called Generalized Maxwell model (GM), because it better suits the complexity of the response of our semicrystalline materials when cast into bars, i.e., as bulk materials. This model depicts very well their viscoelastic response for the temperatures studied.

For the case of thin films, however, the GM model has revealed unable to properly describe their viscoelastic behavior. We attribute this fact to the significant structural changes that films undergo during the processing of the experimental samples used in this study. To overcome such drawback, we have proposed to add non-linear corrections to the model of the mechanical response, and develop the theory associated to this new perspective. Then, a satisfactory fitting is obtained. The type of non-linearity introduced is contained in the Eyring theory. Typically, the Eyring viscosity has been used to describe the hardening of the polymers when they approximate the yield point. We consider that the stretching effect that the processing conditions confer to the amorphous parts of the films, when thinner films are manufactured, could be assimilated to the behavior of polymers close to the yield. The mesoscopic analysis in terms of the Generalized Maxwell model, including the non-linear corrections, permits us to identify the particular features underlying the particular behavior of our films and sandwiches. Moreover, the mixing rule has been used to compare the spectra calculated using the spectra of pure constituents, with the ones directly obtained from experimental storage and loss moduli. The breakdown of the superposition can be seen as the onset of genuine properties due to the confinement of the layers or due to the interfaces.

With regard to the second study in this thesis, block copolymer films (BCP) are considered systems with potential applications in nanotechnology, which range from semiconductors, nanopatterned surfaces, nanocrystals with exotic optoelectronic properties, to functional foods and pharmacological products[36,47,94]. The most relevant feature of these materials is their capacity of self-assemble giving rise to domains of different composition of a nanometric size. These domains arrange in space in different morphologies and geometries, which can reach sizes of 10-100nm, otherwise difficult to achieve with conventional techniques. Nevertheless, a long-range order of the domains, hard to obtain naturally, is needed in order to pave large areas with regular arrays as it is required in the applications. Hence, the work presented here is motivated by the need of understanding the complexity of the arrangements that spherical nanodomains can produce when diblock-copolymers self-assemble onto a chemically patterned substrate. This guiding technique has been proven to be effective for lamellae or cylinder forming BCP. In the case of spheres, it is more challenging because of the higher degree of discontinuity of the morphology. Therefore, our study is focused on investigating the

effectiveness of a strip-patterned surface to modify the ordering of spherical domains in a thin film. We analyze the effect of the of characteristics of the pattern together with the role of the total thickness of the films on the resulting structure.

The methodology used for such an analysis is a coarse-grained description within the so-called Cell Dynamics Simulation (CDS). The free-energy functional responsible for the thermodynamic force used in CDS, formally resembles a Grinzburg-Landau functional, plus a long-range contribution that accounts for the chain connectivity. From the free-energy functional a diffusive dynamics can be constructed in the spirit of the Cahn-Hilliard-Cook equation[91] for systems with a conserved order parameter. This coarse-grained level of description, with no explicit reference to microscopic details, allows us to describe the microphase separation phenomena in systems whose dimensions are comparable with the ones experimentally addressed. More microscopically rich descriptions, like molecular dynamics simulations, are hampered by its heave computational requirements, which limit the affordable sizes and times to be described within this framework.

Thus, using three-dimensional CDS we have found very good agreement with experiments in sphere-forming BCP systems, always that one uses the characteristic distance between domains as the scale for comparison. Going further we found that, with a proper selection of the pattern design, in terms of band periodicity, as well as of the film thickness, we can create well-order arrays of spherical domains with two different types of packing, namely, hexagonal or body-centered orthohedra. Therefore, we suggest a way to control the formation and morfology of long-ranged ordered structures of different types in this kind of systems.

The thesis is organized in two parts, each corresponding to one of the two systems mentioned above. The first part, related to the multilayer films, comprises Chapter 2, in which the description of the viscoelastic behavior of films is addressed, and Chapter 3, where we analize the spectra of relaxation-times, ultimately to infer microscopic properties. It is worth mentioning that the systems studied are industrial products and, therefore, are directly applicable, far from having only an academic interest. Hence these systems have eventually shown an inherent complexity, which will become apparent along Chapters 2 and 3. The second part is devoted to the study of the block copolymers and contains only Chapter 4. Finally, in Chapter 5, the main conclusions

of the thesis are summarized and the main lines for future work are presented.

Chapter 2

Viscoelastic response of multilayer films

Synopsis

In this chapter we will analyze the data of multilayer systems of LLDPE and EVOH polymers. The viscoelastic response of multilayer polymeric films (sandwiches) of linear low-density polyethylene (LLDPE) and ethylene vinyl alcohol (EVOH) copolymer has been experimentally analyzed. We propose an equation to predict the mechanical response of the sandwich films from the data experimentally obtained for the monomaterial films. The equation is based on the hypothesis that the layers independently contribute to the final response and that there are no interfacial effects. The predictive character of the equation permits us to conclude that the response of the sandwich does not significantly depend on the individual layer thickness but only on the volume fraction of the EVOH in the system. More important, we find a strong sensitivity of the response to the processing conditions, which we quantitatively describe.

2.1 Introduction

One of the major applications of polymers in common consumer goods is packaging. Particularly plastic packages play a crucial role in the food industry because the plastic properties significantly affect the transport of light, oxygen, nitrogen, carbon dioxide or water, the growth of microorganisms, the shelf life, and the quality of the products when at the hand of the final consumer. A good package material ultimately permits the supply of healthy, fresh and safe food to more people and for longer time. Such application requires in most of the cases thin films to be produced with specific functional features. The production of thinner films with enhanced properties is thus attractive for companies having activity in this domain. In the last decades, a technique of layer-multiplying coextrusion has been developed to obtain films for high added-value applications[85,103]. Using this technology, sheets formed by a stack of up to hundreds or thousands of layers that combine at least two different polymer species can be produced with individual layer thicknesses of up to tens of nanometers. Multilayer films, or *sandwiches*, may yield effective properties different from those of the pure constituents due to the internal structural changes induced by the particular processing, that can cause confinement of the chains, constrained growth of microscopic crystalline structures, relevant interfacial effects, among others. Despite its evident importance, little is known on the dependence of the sandwich properties on these factors.

In this chapter, we address the analysis of the mechanical response of sandwich films of ethylene vinyl alcohol copolymer (EVOH) embedded in linear low-density polyethylene (LLDPE), of different compositions and layer thicknesses. In particular we mainly focus our attention on their linear viscoelastic behavior, as studied experimentally in a range of temperatures of practical uses. Additionally, we will support our hypothesis with data on tensile properties such as toughness, tear resistance in machine and cross directions, and also provide data on yield stress and strain, rupture stress and strain, and dart-drop impact. This analysis allows us to gain knowledge on the influence that the changes in the internal structure have on the final properties of the sandwich. It is also remarkable, moreover, that studies on the response of the particular LLDPE/EVOH sandwiches have not been addressed yet, to the best of our knowledge.

The first aspect of relevance is the morphology changes when decreasing the layer thickness, as previously reported by other authors[1,25,87,92]. For materials processed

into compression molded bars no structural constraint due to confinement is expected. Thus, for common materials such as LLDPE and EVOH, crystals can form from the melt giving rise to three-dimensional spherulites, which are composed of highly ordered lamellae, with no preferred overall orientation[43]. In the case of thin films, below the micrometer scale, when the layer thickness is smaller than a typical spherulite diameter, the confinement induces changes in the organization of the lamellae, such as flattened spherulites, also referred to as discoids[87,92]. Lamellae in such kind of structures under confinement can be either flat-on or edge-on oriented, depending on the nature of the polymer, as well as on the type of interactions with the confining substrate[25,92]. Going even further, for layer thicknesses of the order of the lamellar thickness, stacks of lamellae are formed or also single lamellae, producing highly oriented structures with an associated anisotropy. All these effects among many others have been observed by different techniques such as atomic force microscopy, transmission electron microscopy, small and wide-angle X-ray scattering, and differential scanning calorimetry, which have been applied to different systems such as PEO (poly(ethylene oxide))[136], HDPE (high-density polyethylene)[11,12,93], LLDPE[57], or PP (polypropylene)[59]. For our systems, with layers of thicknesses from 100 to 1000 nm, however, only discoid structures are expected to form in the films.

It is thus expected that these changes in the structure of the layers influence the dielectric as well as the mechanical response of the sandwich films. Experimentally, dielectric relaxation spectroscopy (DRS), NMR spectroscopy, or dynamic mechanical analysis (DMA) are used to study relaxation properties in a wide frequency range, as reviewed by Boyd[17,18]. Baer and coworkers employed DMA to study the viscoelastic response of films and sandwiches[72]. In this reference, for instance, the dynamic mechanical response of systems obtained by coextruding PEO in thicker PS (poly(styrene)) or EAA (ethylene-co-acrylic acid copolymer) is analyzed. The authors consider the effect of the PEO layer thickness in the viscoelastic properties by increasing the number of layers in the system keeping the volume ratio PS/PEO (conversely, EAA/PEO) constant. In this way PEO layers ranging from 45 nm to 3700 nm are obtained. In general, it is observed that the layers are subject to two competing effects. On the one hand, the affinity of the PEO polymers with the confining layers of PS (EAA) causes interfacial effects due to polymer adsorption. Such a modified PEO structure produces

an interfacial layer whose relative importance increases by decreasing layer thickness. On the other hand, the confinement increases chain mobility lowering the transition temperatures, particularly the glass transition temperature T_g [17]. In this latter reference it is also pointed out that the change in the distribution and morphology of PEO crystals in the layer introduces additional constraints on the remaining amorphous phase, which is generally believed to be responsible for the relaxation processes taking place in the material. In comparison, in our system both pure LLDPE and EVOH are semicrystalline polymers that exhibit thermorheological complexity, due to different relaxation processes that are activated depending on the actual temperature [40], instead of a semicrystalline polymer embedded in an amorphous matrix as in the mentioned reference. The embedded component, EVOH, has a high T_g of about 55°C, particularly high due to hydrogen-bonding OH groups. The matrix polymer is LLDPE, of about 45% of crystallinity, with a weak β-relaxation around -30°C and a larger γ-relaxation below -100°C. Both relaxation processes have been claimed as being the glass-transition temperature [16,124], and to avoid confusion, here we will refer to either β or γ-relaxation when required. Therefore, the thermorheological complexity and the disparity of the transition temperatures of EVOH and LLDPE indicate that multilayered films of these two species shall present a complex rheological behavior.

Despite the apparent complexity that the ensemble of layers of EVOH and LLDPE presents, our study with sandwich films of 25 μm of total thickness (with thin EVOH layers from 160 nm to 470 nm in their structure) reveals that the sandwich properties can be predicted from the properties of the monomaterial films: the contribution of each layer on the total viscoelastic response is additive. Moreover, such additivity is not trivial. We have observed that, to obtain a reasonable agreement between the prediction and the experimental response, data obtained from measurements of bars (2.85 mm thick) of the pure components should not be used for sandwiches of 25 μm. Instead, one should use the response monomaterial films of the same 25 μm thickness. This fact indicates that the processing conditions play a very important role in the mechanical response of these systems. Structural transformations occurring in the extrusion of the plastic into films are likely to be similar in sandwiches as well as in pure films of the same overall thickness. Additionally, when sandwiches of an overall thickness of 100 μm (EVOH layers from 875 nm to 1560 nm) are analyzed, we can

still predict their mechanical behavior using the data on the response of pure EVOH films 100 μm thick as input in the superposition calculation. In our experimental setup, different film thicknesses are obtained by changing the draw ratio, i.e. the ratio between the melt velocity at the exit of the extrusion die and the draw velocity at the cooling roll. Particularly, in the experiments carried out, the melt velocity has been kept constant, while the draw velocity has been increased to produce thinner films. We thus arrive to the conclusion that the processing conditions introduce morphological changes at the microscopic level, likely to be caused by the extensional flow rate due to the draw process when the solid is formed. These morphological changes are analogous in all the systems at the same draw rate and, therefore, only films processed under the same draw ratio can be compared. The mixing rule is valid over a wide range of temperatures involving different transitions in each of the components.

In summary, we can therefore state that i) the mechanical response of these semicrystalline films significantly depends on the draw rate when solidifying, ii) the superposition of the responses of pure components is a good approximation to describe the observed behavior of sandwiches, if the processing conditions are the same, and iii) the agreement is maintained over a wide range of temperatures.

Together with the inherent interest of what we have just stated, the empirical knowledge of the system described is also intrinsically important. Thus, we not only provide data on the viscoelastic response on the range of temperatures indicated, but also data on tensile properties of the sandwiches such as the tear resistance, toughness, stress and strain at yield and at break, although a deep analysis of these properties lay beyond the scope of the work.

2.2 Fundamentals

2.2.1 Polymer Viscoelasticity

The study of mechanical properties is approached by classical physics through the theory of elasticity for solids and the theory of hydrodynamics for viscous liquids. According to Hooke's law, stress is always proportional to strain for solids while, according to Newton's law, stress is directly proportional to the strain rate for liquids. Polymers are materials that are in between these two limiting cases, they exhibit properties that

have common solid-like and liquid-like characteristics when undergoing deformation, i.e, they are viscoelastic materials[40]. In fact, the frontier between solid and liquids, from a mechanical point of view, depends on the observation time (the time associated to an external perturbation), which needs to be compared to the molecular relaxation-times. The relaxation-time is the joint effect of the friction and elasticity which implies that some of the energy input transferred by deformation is stored and recovered and the rest of the energy is dissipated as heat. Then, the viscoelasticity can be defined as the dynamic response to an external deformation[111].

When applying an external deformation to a polymeric material, for a general case, different regions can be identified on a stress-strain curve, as shown in Figure 2.1. During homogeneous deformation a fully reversible type of behavior can be appreciated, which corresponds to the linear viscoelastic region. Linear viscoelasticity holds when the strain and the rate of strain are infinitesimal, region in which the stress-strain relations can be described by linear differential equations with constant coefficients. For larger deformations the material becomes progressively nonlinear until it becomes irrecoverable at yield. Then strain softening and strain hardening can occur in the so-called plastic region. Whereas the strain softening is caused by stress-induced flow that starts changing the material structure and reduces the material's resistance, the strain hardening is caused by increased orientation of chain segments or the stress-induced crystallization. Finally, if increasing further the deformation, the material turns out to fail[137].

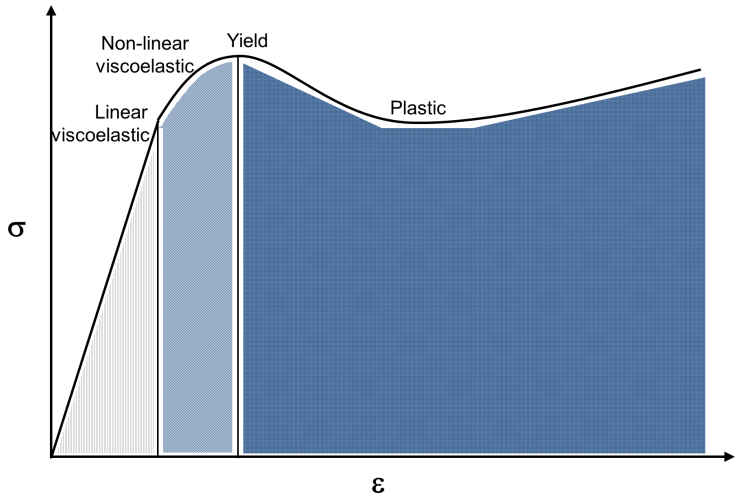

Figure 2.1: *Schematic representation of the stress-strain curve of a polymer material*

While for many conventional functional materials the viscoelastic anomalies are considered irrelevant, in the case of polymeric systems, they are the norm. The mechanical behavior of polymers is dominated by viscoelastic phenomena since any macroscopic mechanical deformation involves complex molecular adjustments. At microscopic scale, local movements can be relatively rapid but rearrangements involving larger segments of polymer chains can take much longer time. Hence, the viscoelastic properties in polymers are interesting, not only for practical reasons such as the mechanical behavior during processing or in the final applications, but also because the viscoelasticity is causally linked to a variety of microphysical processes. It can provide information about the nature of molecular mobility, and the disposition and interaction of the macromolecules in the short and long-range interrelations[40].

2.2.2 Multilayer technology

It is well known that the functional performance of a material is improved by the synergistic union in a layered structure of two or more materials with complementary properties. In fact, this is a strategy recurrently followed by natural biological systems, such as plant or animal tissues, among which we can found many layered architectures. The reason is that the layers are organized forming hierarchically composite systems, with the ability to hold up very complex functions[5,6].

One of the first technological achievements in this direction was done by combining polymers as association of hundreds of continuous layers into a thin film in order to obtain multilayered architectures. Co-extrusion, a series of multiplying die elements as observed in Figure 2.2, and a cast film line to reestablish the desired overall film thickness, are the main elements of the technology to produce such films. The described technology, known as multilayer technology, benefits from the viscoelastic nature of polymeric melts and uses forced-assembly to create polymer films composed of hundreds of micro or nanolayers[80].

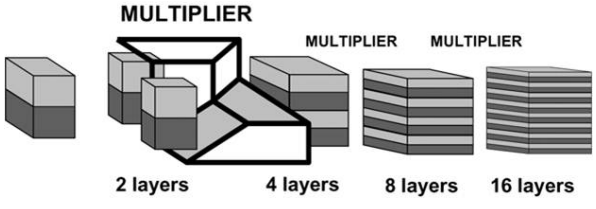

Figure 2.2: *Scheme of the multilayer technology*

2.3 Experimental Section

The linear low-density polyethylene (LLDPE) used in our experiments was produced with Ziegler-Natta catalyst from The Dow Chemical Company *DOWLEX* ^{TM} with a density (ρ) of 0.917 g/cm^3 and a Melt Index (MI) at 190°C of 2.3 $g/10min$. The ethylene vinyl alcohol (EVOH) was provided by *EVAL Europe*, and is a copolymer of ethylene and vinyl alcohol with $\rho = 1.19$ g/cm^3 and a MI at 190°C of 1.8 $g/10min$. This random copolymer contains a 0.32 molar fraction of ethylene monomer in its composition. The Poissons ratio for the LLDPE and for the EVOH was experimentally estimated to be $\nu = 0.5$ and $\nu = 0.33$, respectively. These properties are summarized in Table 2.1.

Resin	Specie	Melt Index [g/10 min]	Density [g/cm^3]	Poisson ratio
DOWLEX SC2107G	LLDPE	2.3	0.917	0.5
EVAL F171B	EVOH	1.8	1.19	0.33

Table 2.1: *Characteristics of the resines used in the study, namely LLDPE and EVOH*

Different samples were prepared for the tests. First, to study the viscoelasticity in bulk materials, bars of pure LLDPE and pure EVOH were produced by compression molding technique. Additionally, thin multilayer films were fabricated [85,103]. The first step for their production is a coextrusion cast line, which consists of four different extruders, three of them with LLDPE and one of them with EVOH split into two layers. The following step is a Dr. Collin five-layer coextrusion feed-block, where the precursor film to be replicated was formed. Therefore, such a precursor film consists of an external LLDPE layer (A, for ease of notation) of thickness d_1, followed by an EVOH (B) layer of thickness d_2, a central LLDPE layer (C) of thickness d_3 and then again layers B and the external A. The resulting structure is the five layer ABCBA, characterized by three layer thicknesses d_1, d_2 and d_3 whose relative dimensions eventually determine the volume fraction of each component in the resulting film. The subsequent elements are two layer multipliers (a 2 times and a 4 times multiplier), which allow to obtain films of alternating LLDPE/EVOH layers by the replication of the ABCBA structure, followed by a cast die (with dimensions of 0.7 mm for the die gap and 300 mm for

Film thickness [μm]	25	50	100
Melt velocity in die [m/min]	0.88	0.88	0.88
Film take-off velocity [m/min]	21	10.8	4.8
Melt-draw ratio	23.6	12.2	5.4

Table 2.2: *Processing parameters of the multilayer films*

the die width). Special care was given to match the rheological properties taking into account the melt viscosities and shear rate in order to ensure layer uniformity, and to prevent interlayer instabilities. The final step is a cooling unit, whose main component is the chill roll, where the solidifying stage takes place as the temperature decreases from 230°C to 20°C. The total output was kept constant at 8.3 kg/h for the three different thicknesses. Other constant parameters are the chill roll diameter and the distance between the die and the roll, which are, respectively, 144 and 18 mm. The variability in films thickness comes from the control of the velocity in the take-off roll (draw velocity), as typically done in industrial processes due to their interest in using the extruder at its maximum capacity. For the 25 μm films, the draw velocity was 21 m/min, 10.8 m/min for the 50 μm films, and 5.8 m/min for the 100 μm case. In Table 2.2 the velocity of the melt in the die, and the draw velocity, as well as the ratio between them, are shown. Sandwich films of 40 layers (the five-layer precursor film replicated 8 times) with total thicknesses of 25 μm and 100 μm were fabricated using the mentioned technique. An example of a resulting sandwich structure is shown in the SEM picture in Figure 2.3.

For the sake of comparison, LLDPE and EVOH monomaterial films were produced in the same way as the multilayer films, with the same set of parameters, so that the processing conditions were identical for equal overall film thicknesses.

We cannot report direct information on the individual layer thicknesses for the samples used. However, it was inferred from the information of the processing conditions, i.e., the total film thickness, the feed ratio, and the times the precursor film was multiplied. We checked that these estimated values agree well with the direct measurements of the layer thickness. Other studies also confirm the validity of this procedure[80]. In Table 2.3 the different systems studied with their compositions, total film and layer thicknesses are presented. A further mention should be made of the fact that an interface develops at the contact of the different layers, which depend on the

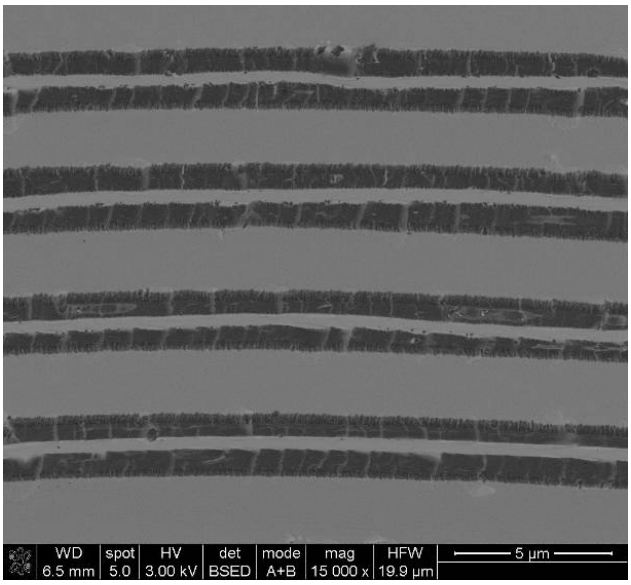

Figure 2.3: *SEM image taken of a LLDPE/EVOH multilayer film with the EVOH (B) layers (darker gray) embedded in LLDPE (A and C). The replication of the 5 layer precursor film ABCBA leads to a* $\cdots ABCBAABCBA \cdots$ *composite film*

nature of the constituent polymers. Its thickness is estimated as being in the range of 5-30 nm[79,80], which is much smaller than the thicknesses of the individual layers used in our study. Dynamic mechanical testing was conducted on bars and films with the *ARES* system of *TA Instruments* using the film or solid-state setup provided by *TA Instruments*. The storage (E') and loss (E'') moduli are obtained by recording the time-dependent stress while a sinusoidal strain is applied to the sample. Frequency sweeps from 1 to 100 rad/s, with a maximum strain of 0.1%, were performed at different constant temperatures. Steps of 5°C were taken in the temperature range from -100°C to 100°C using a soak time of 300 s to arrive at the thermal equilibrium prior to the frequency sweep. Although in principle this procedure is suitable for constructing time-temperature superposition plots, we have gathered data of a fixed frequency of 2.5 rad/s at all the temperatures analyzed aiming at the study of the temperature dependence of the viscoelastic response. Thermorheological complexity makes time-temperature superposition impossible for our system for the entire range of temperatures.

LLDPE/EVOH (v/v)	Total thickness [μm]	A-thickness d_1 [nm]	B-thickness d_2 [nm]	C-thickness d_3 [nm]	System ID
100/0	25	25,000	0	0	Control 1
0/100	25	0	25,000	0	Control 2
	50	0	50,000	0	Control 3
	100	0	100,000	0	Control 4
90/10	25	940	160	940	S10
86/14	25	910	220	875	S14_25
	100	3625	875	3500	S14_100
81/19	25	1030	300	470	S19
75/25	25	780	390	780	S25_25
	100	3125	1560	3125	S25_100
70/30	25	780	470	625	S30

Table 2.3: *Composition and thicknesses of the systems studied*

To analyze the bars, torsion experiments were carried out. Samples of 32 mm by 12 mm were cooled down to -100°C. Subsequently, steps of 5°C between frequency sweeps were performed until reaching a temperature of 100°C, or until the measured torque was below transducer sensitivity. Shear moduli and loss tangent were obtained. The tensile moduli (E) of the bars is estimated by using the relation $E = 2G(1+\nu)$, valid for isotropic systems, where G is the shear modulus experimentally obtained and ν is the Poisson ratio. In the case of films, instead, tensile experiments were conducted. Thus, pieces of a width of 7.6 mm were cut from monomaterial LLDPE and EVOH films and multilayer LLDPE/EVOH sheets. The films were tightly clamped to the grips in the experimental setup for tensile measurements in films. The samples were cooled down to -80°C and heated in steps of 5°C, using the same procedure described before for the bars, up to 50°C. Tensile moduli and loss tangent in the machine direction were in this way directly obtained. Additional experiments on the thin films were carried out for further mechanical characterization. In these measurements the film samples are deformed in the nonlinear viscoelastic region until material failure occurs. Elmendorf tear is a ASTM specified test (ASTM D 1922). A film specimen is prepared with a partial cut. Both flaps are fixed into a machine and, by a pendulum, the tear is

propagated through the film while the force to continue the tear is recorded (in grams). Dart drop impact is measured according to ISO 7765-1. The film is fixed in a circular frame and a dart with a specified tip and weight is released from a defined height. The dart weight at which the 50% of the film specimen breaks is identified and recorded. Stress and Strain at yield and at break are parameters of the engineering stress-strain curve measured in a tensile strength test according to ISO 5273. A 15 mm wide film specimen is fixed at a defined distance between grips and the engineering stress strain curve at 500 mm/min is recorded. Tensile toughness is the area under the stress-strain curve.

2.4 Results and Discussion

2.4.1 Dynamics of Pure LLDPE and EVOH in Bars and Films

The analysis of the pure components, for both bars and films of different thicknesses, is addressed to obtain previous knowledge on the variation of the viscoelastic response in temperature and thickness. The storage (E') and loss (E') moduli, as well as the loss tangent ($\tan\delta = E''/E'$), for pure LLDPE and EVOH, are shown in Figures 2.4 and 2.5. In these figures data collected from bars are compared to data from the films of the pure components for a single frequency of 2.5 rad/s.

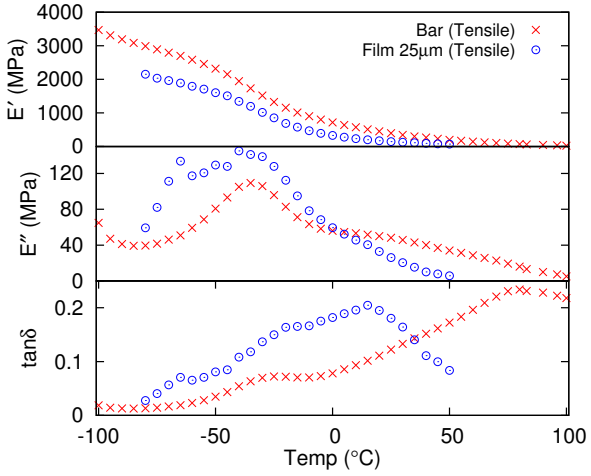

Figure 2.4: *Dynamic mechanical response of LLDPE bar and film of 25 μm (Control 1) at a frequency of 2.5 rad/s*

The loss tangent obtained for the LLDPE bars in the studied temperature range

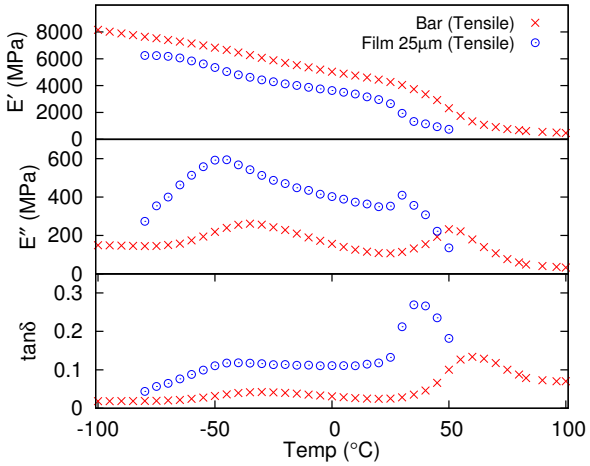

Figure 2.5: *Dynamic mechanical response of EVOH bar and film of 25 μm (Control 2) at a frequency of 2.5 rad/s*

shows two relaxation mechanisms customarily referred to as the α and β-relaxations, at 75°C and at -30°C, respectively. It is well known that a third mechanism, known as the γ-relaxation, appears at lower temperatures, below -100°C[18,54], which lays out of the range studied in this work. The β-relaxation has been associated to the motions of the amorphous fraction occupying the space between crystallites and with the rubber-glass transition. For the linear polyethylene this relaxation is very low due to the existence of an important fraction of *taut tie* chains of polymer between the crystals[88]. Some debate persists in the literature on the location of the true glass transition temperature T_g in LLDPE. Some authors[124] place the glass transition at the γ-relaxation, arguing that there are still segmental motions below the β-relaxation, while others[16] assign T_g where the weak β-relaxation occurs (-30°C).

The $\tan\delta$ plot for the bar of the EVOH copolymer also shows two relaxations. The first can be located around 55°C and the second, at about -30°C. These processes are identified as the α and β-relaxations, respectively[20]. According to this last reference, the size of the EVOH monomers prevents the existence of a γ-relaxation, understood as being caused by the motion of small sections of polyethylene comonomers of about 4 or 5 units. In this latter case, the α-relaxation in the loss tangent corresponds to the phenomena that take place around the rubber-glass transition of this particular polymer.

The peaks in $\tan\delta$ associated to the different relaxation processes, are the result of

contributions of different phenomena. In the first place, the system is microscopically non-homogeneous. The inhomogeneity is due to the presence of amorphous and crystalline phases, but also due to the inherent polydispersity of the polymer segments in the amorphous phase. In general, for the glass-rubber relaxation the position of the peak is determined by the value of the activation energies of the different modes of relaxation (relaxation-times τ). The distribution of relaxation-times, together with the functional form of the individual mechanical response of every mode can be affected by the temperature, as well as the processing conditions. Hence, as it is well known, when processing polymers to produce thin films the orientation of the molecules in the amorphous phase is modified, influencing the activation energies as well as the relaxation-time distribution. The orientation and morphology of the lamellae and spherulites can also be affected, introducing significant structural differences when compared to bars. The effect of these morphological changes on the dynamical response is customarily assumed to cause a higher intensity in the loss tangent and lower transition temperatures for the thin films. In many cases, the alignment of the chains in the amorphous phase also induces narrower peaks (due to a narrower relaxation-time distribution) [16,17]. We will see in Chapter 3 the analysis of the relaxation-time distributions and how our systems agree or not with this view. These effects together generally lead to films that are softer and more dissipative than bars [17,88,137].

The analysis of the E' curves in Figures 2.4 and 2.5 indicates that the storage modulus is lower in films than in bars, in agreement with the usual picture described above. Both materials show a crossover between two regimes through the rubber-glass transition temperature. However, while the EVOH shows a clear shift of the transition for LLDPE the crossover seems also broadened, although the curves roughly keep the same overall shape.

The E'' curves, however, show larger differences. On the one hand, for the LLDPE case, the peak corresponding to the rubber-glass relaxation is shifted to lower temperatures; in addition, it is broadened by the appearance of a secondary peak at lower temperatures. For the EVOH system, the loss modulus is shifted also to lower temperatures when compared to the bars. However, to better understand the nature of the shift and broadening of the peaks for this latter material it is illustrative to observe the changes introduced by the variation of the thickness of the film. In Figure 2.6 we

present the mechanical response of EVOH films of 25, 50, and 100 μm. We observe that, as the film thickness decreases, the dissipation (loss modulus) increases. A new peak develops in E'' for the film of 25 μm, while there is only a crossover in the films of 50 and 100 μm. In Figure 2.7 we give the detail of the $\tan\delta$. We observe precisely the appearance of the satellite peak more than a shift in a preexisting one. The change in this behavior and the appearance of the new peak in E'' should ultimately be attributed to the structural changes caused by the different processing conditions more than to the confinement of the system due to the thickness reduction, or to interfacial effets arisen from the contact between the materials.

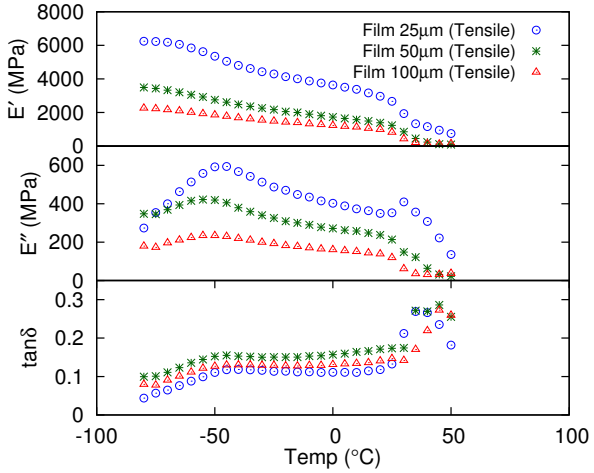

Figure 2.6: *Dynamic mechanical response of pure EVOH films of 25, 50, and 100 μm (Control 2, 3 and 4) at a frequency of 2.5 rad/s*

Moreover, the decrease of E'' is faster in films than in bars. This effect, which is present in both materials, is more significant at temperatures above the transition temperature. This faster decrease can be, in turn, attributed to the orientation of the polymer strands in the amorphous phase, which would lead to a narrower relaxation-time distribution due to the orientation and stretching of the chains. These facts suggest that the processing of the materials into films produces a more ordered amorphous phase, which is translated into the usual properties of the films as, for instance, softer and more dissipative materials. However, the fact that the thinnest film develops new peaks in E'' for both the EVOH as well as the LLDPE strongly suggests a significant structural change in the system, probably associated to the change in orientation of the crystalline phase as well as a change of the morphology of the discoids deformed

by stresses during the processing. Such changes in the crystalline phase would produce different constraints to the amorphous phase that, eventually, are responsible for a new relaxation-time distribution that overlaps with the usual one. The melt-draw ratio is roughly four times larger for the 25 μm than for the 100 μm systems. The solidification of the material under tension effectively implies that the surviving crystallites must lay mostly perpendicular to the flow direction. The latter is further confirmed by the difference in the tear resistance in the machine direction (MD) and the cross direction (CD), discussed later on.

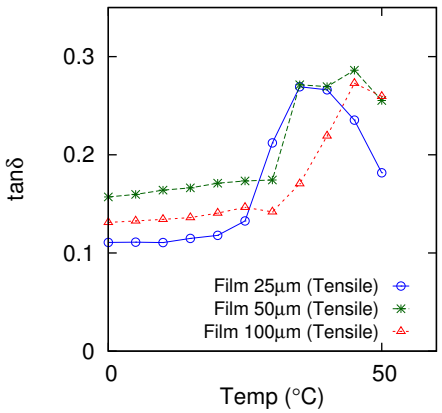

Figure 2.7: *Detail in the loss tangent of monomaterial EVOH films of 25, 50, and 100 μm (Control 2, 3 and 4) at a frequency of 2.5 rad/s*

The analysis of $\tan\delta$ can be understood to the light of what we have stated for E' and E''. We see that the shift in the peak of the glass-rubber transition is mostly due to the presence of the new peak at lower temperature, which also explains the broadening of the peak in the case of the LLDPE. The magnitude of the shift is determined by how fast E'' decreases at temperatures above the transition.

2.4.2 Dynamical Mechanical Analysis of LLDPE/EVOH Multilayer Films of 25 μm

2.4.2.1 Dynamical Mechanical Analysis

The mechanical responses of the sandwiches of overall thickness of 25 μm are analyzed in the first place. Figure 2.8 shows the experimental storage and loss moduli together with the loss tangent at a single frequency of 2.5 rad/s of three different sandwiches with a 10%, 19% and 30% of EVOH, indexed according to Table 2.3. We compare these

data with the predictions made using the response of pure materials. To rationalize the response, in eq. (2.1) we propose a model in which each separate layer contributes independently to the total stress with the constraint of all layers having the same strain. This simple analysis yields

$$E^* = \sum_i \phi_i E_i^* \tag{2.1}$$

where E^* is the viscoelastic complex modulus of the multilayer film, E_i^* is the complex modulus of the species i, and ϕ_i is its volume fraction in the system. The complex modulus can be split into a real (storage modulus E') and an imaginary (loss modulus E'') part, according to $E^* = E' + iE''$. Using the measured E_i^* for the monomaterial films as input, we have made predictions for the response of the multilayer films and compared to the experimental data obtained. In all cases, we observe a rather good agreement between the measured response for the sandwiches and that predicted by eq. (2.1). Notice that there are no fitting parameters. Furthermore, the error in the experimental determination either of E^* as well as of E_i^* is below the 10%, in our case. Hence, the presence of the EVOH layers in the LLDPE matrix induces an increase of the rigidity in the system. The overall effect then is that the contribution of each species in the sandwich is additive and proportional to each volume fraction, always taking as reference the behavior of films of pure components with the same thickness as the overall sandwich (same draw ratio). The more significant deviations between the predicted and observed response correspond to the loss modulus E'' below -30°C. This domain of temperatures roughly coincides with the region below the relaxation processes of both LLDPE and EVOH.

As mentioned, the use of data from bars of pure component as an input in eq. (2.1) produces results that significantly disagree with the experimental response for the 25 μm sandwiches. It is then clear that the structural changes due to the processing conditions are already present in the monomaterial films, as well as in sandwiches of the same thickness. As a consequence of the additivity, we find that the response of the sandwich films is fairly independent on the EVOH layer thickness, in the range of thicknesses comprised between 160 nm and 470 nm, corresponding to sandwiches comprised between 10% to 30% of EVOH respectively, and depends solely on the overall EVOH volume fraction.

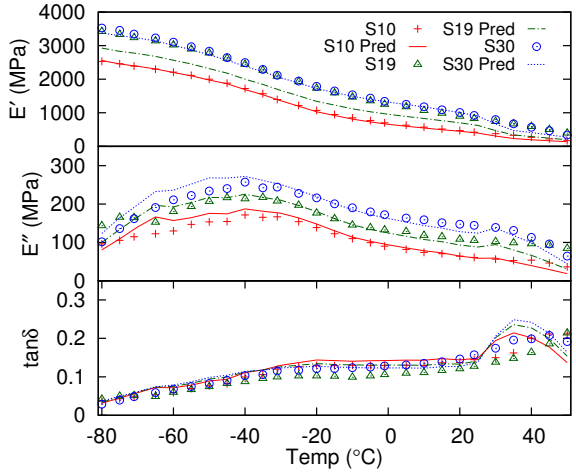

Figure 2.8: *Dynamic mechanical response: storage modulus, loss modulus and loss tangent curve of 90/10, 86/14, 81/19, 75/25, 70/30 LLDPE/EVOH systems (see Table 2.3). The solid lines are the predictions using eq. 2.1*

In Figure 2.9 as a typical case we show the predictions for the 25 μm sandwich of 10% of EVOH at all the frequencies tested, from 1 to 100 rad/s at different fixed temperatures in the range studied. We observe that the predictions roughly match the experimental results for all the frequency range. The same is observed for all the temperatures of our study as well as the sandwich compositions.

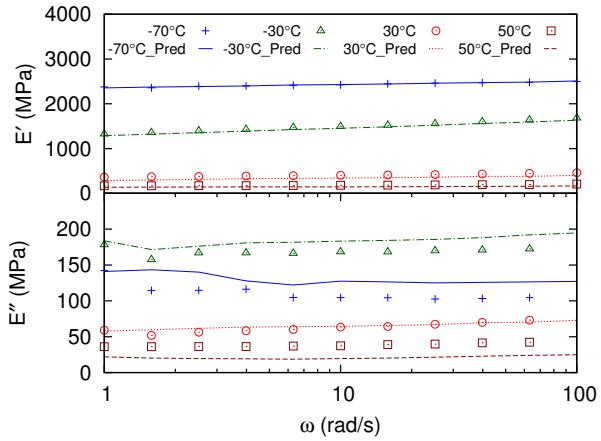

Figure 2.9: *Dynamic mechanical response: storage modulus of 90/10 LLDPE/EVOH 25 μm system at temperatures of -70° C, -30° C, 30° C, and 50° C. The solid lines are the predictions using eq. 2.1*

2.4.2.2 Destructive tensile properties

To complete the analysis of the 25 μm sandwiches we performed a series of destructive tests on them. In the first place, the tear resistance using the Elmendorf tear tester in the machine (MD) and cross directions (CD) is discussed. In our experiments we have considered the sandwiches with a 0%, 10%, 19% and 30% of EVOH, detailed in Table 2.3.

As far as the MD is concerned, the data indicates that the Elmendorf tear resistance parameter increases with the EVOH content of the system. The hypothesis of the additivity of the stresses should turn also the additivity of the energy spend in tear the film. The independence of each layer contribution is supported by the hypothesis that the strain is the same for each layer and that the total stress is the sum of each layer contribution. We can therefore see in this property whether the layers respond independently or not. Effectively, the energy up to tear, conceived as an integral over the stress-strain curve, is also a sum of contributions. Hence, denoting by ξ the measured parameter this fact can be stated as

$$\xi = \sum_i \phi_i \xi_i \tag{2.2}$$

For the particular case of two components, one has $\xi = (\xi_2 - \xi_1)\phi_2 + \xi_1$, where the subscripts 1 and 2 refer to LLDPE and EVOH, respectively, while ϕ is the EVOH volume fraction. As we can see in Figure 2.10-a, there is a linear trend but with a significant variation between the MD and the CD directions. The positive slope of the MD tear resistance suggests that $\xi_{EVOH} > \xi_{LLDPE}$, while the inequality is reversed for the CD, $\xi_{EVOH} < \xi_{LLDPE}$. This fact is a clear signature of the influence of the processing conditions in the properties of the final material, due to the tension hold by the film during the solidification. In particular, such a different behavior can be due to the anisotropic orientation of the crystallites, which will grow mostly in the direction orthogonal to the extensional flow during the solidification due to, first, the preferred orientation of the chains along the flow and, second, because the contraction of the material during the solidification is easier in the direction where no stress has to be withstand. Such an orientation confers larger rigidity of the material in the CD due to the crystallites as compared to the MD. Notice that in the Elmendorf tear experiment

we are proving the elastic properties of the material in the direction orthogonal to the tear. Therefore, the increase of ξ in the MD direction indicates an increase of the resistance of the system in the CD, and conversely, the decrease of ξ in the CD indicates a decrease of the resistance in the MD. The toughness experiment done in the MD confirms this result (see Figure 2.10-b). Furthermore, the difference in the slopes in Figure 2.10-a indicates that this process affects differently the EVOH from the LLDPE. We can conclude that the change in sign of the slope in the tear resistance indicates that the EVOH develops a more anisotropic structure. However, to confirm such a hypothesis more experiments directly revealing the microscopic structure should be undertaken.

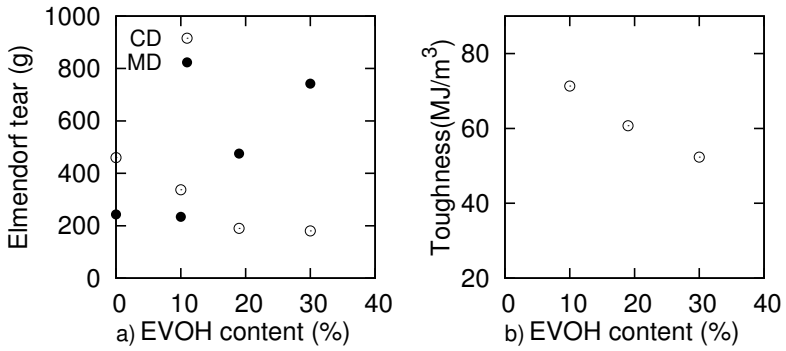

Figure 2.10: *(a): Elmendorf tear for LLDPE/EVOH 25 μm systems of different EVOH volume fractions, in the cross (CD) and machine (MD) directions. (b): Toughness experiment for different EVOH volume fractions in MD.*

Additionally, we performed the dart drop impact test, which measures the energy that causes the film to fail by a dart impact. We observe a tendency to decrease the weight of the dart at which the material fails with the amount of EVOH, the data is shown in Table 2.4. In comparison with the previously analyzed data, however, we can infer that the material fails in the MD direction, coinciding with the decrease of the toughness in this same direction with the increase of EVOH, and in agreement with the decrease of the weight of the dart in the test.

System ID	Elmendorf tear [g]		Toughness [MJ/m^3]	Dart Drop Impact [g]	Stress at yield [MPa]	Stress at break [MPa]	Strain at yield [%]	Strain at break [%]
	MD	CD						
Control 1	243	460						
S10	234	337	71.3	184	8.8	30.3	8.6	352
S19	475	190	60.7	185	13.8	35.4	4.9	254
S30	742	180	52.3	120	18.3	39.8	4.3	189

Table 2.4: *Destructive test properties of the systems studied*

Data on the stress and strain at yield and at break are also reported (see Table 2.4), both in the MD. For these properties the linearity cannot be directly checked without the knowledge of the complete stress-strain characteristics of every material. Therefore, we only report here the data. We generally observe the same trends as revealed by the previous measurements. These can be summarized as follows: the addition of EVOH, under the conditions of our experiments, increases the rigidity of the material along the MD direction but reduces its toughness. This is compatible with larger stresses but lower strain at yield and at break.

2.4.3 Dynamical Mechanical Analysis of LLDPE/EVOH Multilayer Films of 100 μm

The thicknesses of the embedded EVOH layers in 100 μm sandwiches are comprised in the range between 875 nm and 1560 nm, all thicker than any of the EVOH layers in the 25 μm sandwiches considered. Figure 2.11 shows the experimental values for two analogous sandwiches with equal EVOH fraction of 14%, but for an overall film thickness of 25 μm and 100 μm (220 nm and 875 nm for the inner EVOH layers, respectively).

We observe that the mechanical properties are not the same despite the fact that the EVOH content is the same in both materials. From eq. (2.1) we can again predict the behavior of the 100 μm sandwiches from the data of the monomaterial films processed under the same draw ratio, that is, pure films of 100 μm. Similarly, Figure 2.12 shows

the data and the predictions from eq. (2.1) for the systems that contain an EVOH volume fraction of 25% for an overall multilayer film thickness of 25 μm and 100 μm (EVOH layers with a thickness of 390 nm and 1560 nm, respectively).

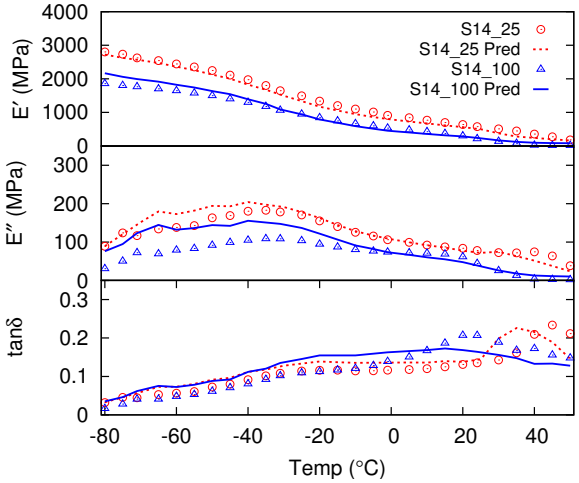

Figure 2.11: *Dynamic mechanical response of different thickness multilayer films: storage modulus, loss modulus and loss tangent curve of 86/14 LLDPE/EVOH systems of 25 and 100 μm. The solid lines are the predictions using eq. 2.1*

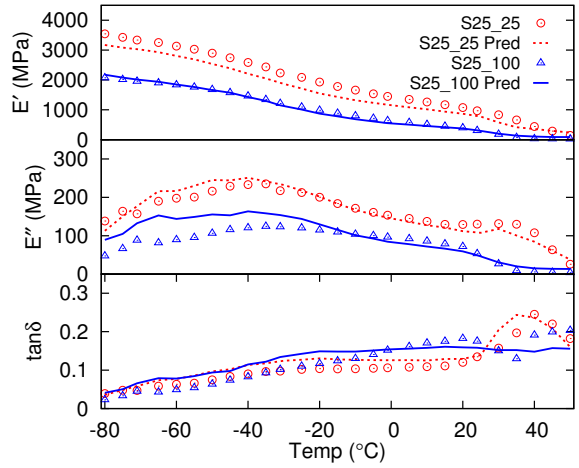

Figure 2.12: *Dynamic mechanical response of different thickness multilayer films: storage modulus, loss modulus and loss tangent curve of 75/25 LLDPE/EVOH systems of 25 and 100 μm. The solid lines are the predictions using eq. 2.1*

Therefore, the predictions of the response of sandwiches from the monomaterial films are very good for E'. The formula eq. (2.1) overestimates the loss modulus E'' at low temperature, below the β-transition of the LLDPE but describes fairly well the transition around the glass-rubber transition in the EVOH. The small differences in

both E'' and E' make that the differences between the prediction and the experimental $\tan\delta$ are more noticeable, precisely at around 30°, where the glass-rubber transition of the EVOH occurs.

Summarizing this section, the data presented support several statements. First, the additivity of the mechanical response indicates that the internal layer thickness of the sandwiches is not relevant with regard to the mechanical properties, in the range of thicknesses studied in this work. This does not preclude that smaller layer thicknesses, of the order of the lamellae, may significantly change this statement [72]. Interfacial effects between EVOH and LLDPE layers also seem irrelevant. Second, the draw ratio strongly influences the microstructure of the material, due to the fact that in the cooling section the solidification takes place under stress in the machine direction. We can assume that the microstructure of the system would then consist of discoidal spherulites distorted in the direction of the flow, with a strong tendency to form larger crystallites orthogonal to the flow (MD) than in the opposite direction. In addition, this property depends on the nature of the material, either EVOH or LLDPE. The influence of the draw ratio in the microscopic properties is, therefore, responsible of the strong anisotropy of the material and also in the dependence of the viscoelastic properties in the overall thickness of the films of pure materials used in the fit of eq. (2.1).

2.5 Conclusions

We have found that the mechanical response of the viscoelastic multilayer films of LLDPE/EVOH, in terms of their storage and loss moduli, can be very well predicted by a simple additive rule based on the mechanical independence of the layers and the negligible role of interfacial effects. We have also observed that the response of the different sandwiches with the same overall thickness depends only on the volume fraction of EVOH and is insensitive to the thickness and number of the individual EVOH layers, at least in the range of thicknesses studied along the paper. However, other studies using amorphous/crystalline PS/PEO [72] had found sensitivity to the individual layer thickness in systems with inner layer thickness in the range from 45 to 3700 nm. The predictive character of eq. (2.1) permits us to obtain an estimate of the response of

a given sandwich from the data of pure components. We have found that the agreement is obtained only in the case where the sandwich, as well as the films of pure component, has the same overall thickness i.e. the same draw ratio (see Table 2.2). The use of data either from bars or from other films thicknesses into eq. (2.1) yields disparate results.

The analysis of destructive tensile properties indicates that the material is strongly anisotropic with regard to the machine and cross directions, which is again a strong proof of the effect of the processing conditions on the material properties. The observed properties are compatible with a material formed by crystallites oriented preferably in a plane orthogonal to the draw direction, where no tension is applied, with bundles of rather oriented fibers in the draw direction. Furthermore, this effect seems to be more significant for the EVOH than for the LLDPE. Nevertheless, our macroscopic study cannot directly give insight on the particular structural changes giving rise to the differences, and should be complemented with direct observation of the microstructure of the films. We can conclude that the particular properties observed in our system are not due to the confinement itself or to the interfacial properties due to the contact between layers, but to the effect of the strain and molecular orientation of the film in the solidification process. This fact, however, does not preclude that the confinement may play a role on the analyzed properties, but such a role is not dominant. In this sense, one should notice the difference between the predicted loss modulus and the experimentally measured ones. The solution of these questions is clearly of interest for future studies.

Chapter 3

Modeling the viscoelastic properties

Synopsis

In this chapter we will propose a more mesoscopic model for the viscoelastic response of the solid LLDPE and EVOH films and sandwiches. The model is formally a Generalized Maxwell (GM) model, which corresponds to a mechanical analog of the complex response of the material. The fitting of the model to the viscoelastic response for different temperatures allows us to obtain information on the spectra of relaxation-times, which, bear information on the microscopic structure of the system. We have compared the spectra of relaxation-times of bars and films of pure components, to see what is the effect of the processing on them when passing from bars to films. We have also compared the response of the sandwich films with the one of the pure films, in agreement with the mixing rule previously described. We found that properly mixing the spectra of the pure films we recover the observed spectra for the sandwiches. In particular, since the GM model was unable to produce a good fitting of the experimental data and due to the assumed non-equilibrium conformation of the samples because of the processing, we have developed from scratch a non-linear correction to the viscoelastic response, in the spirit of Eyring theory. With the non-linear corrections added, we find a quantitative very good agreement with the experimental data. The spectra of the corrective terms indicate us which modes are mostly affected by the processing.

3.1 Introduction

Commonly, in the design of plastic materials the mechanical properties are tested experimentally and, by means of empirical rules, one approaches the sought material that complies with the desired requirements. An ideal modeling tool to design optimized materials, without an extensive use of trial-and-error experimental procedures, would require having *a priori* an accurate knowledge about the underlying molecular structure and its relationship with the macroscopic properties. The deformation of a viscoelastic material is governed by relaxation mechanisms, which have a particular origin at microscopic level, due to the inherent complexity of the molecules themselves. The relaxation mechanisms are conditioned by the microscopic structure of the material, which depends on the molecular nature of the polymeric constituents and on the processing conditions, as well. These mechanisms represent specific molecular motions activated by temperature and stress, and can be characterized by a spectrum of relaxation-times.

Although molecular detailed models are unapproachable for polymeric materials due to the large length and time scales that are involved in their behavior, the problem of modeling can be addressed by systematically studying the influence of molecular properties and processing on the evolution of the mechanical response in time or, conversely, in the frequency domain. Hence, using a phenomenological model with physical basis one could describe the experimentally observed deformation and relate it to structural information of great design interest. Such a model should account for the contributions of the various relaxation mechanisms in the material, the time dependence, and the temperature and stress dependence. Simple mechanical models, such as the generalized Maxwell or the Takayanagi models[137], have been proposed to come up with a spectrum of relaxation-times. This kind of models are considered as *constitutive* models for the viscoelastic response of solid polymers under stress.

In the present chapter, we aim at determining a constitutive model for the linear viscoelastic response of the LLDPE/EVOH multilayer films of Chapter 2, and extract the possible structural information. To the best of our knowledge, most of the works in literature on the subject followed the line of describing the morphology of this kind of materials and their functional properties[11,12,56,59,85,93,99,115,134]. However, little has been done with regard to the modeling of their mechanical properties, particularly for

semi-crystalline polymers. Thus, we approach the problem by using a simple model to describe, first, the linear viscoelastic response of pure LLDPE and pure EVOH in compression molded bars; secondly, we adapt this model to analyze the viscoelastic behavior of monolayer films of the same polymeric materials. Therefore, having modeled the viscoelastic behavior of the monolayer films, we can finally describe the response of LLDPE/EVOH sandwich films, of the same overall thickness, in agreement with the conclusions drawn in the Chapter 2. The systems used are the same for which we have already analyzed its linear viscoelastic responses in the previous chapter.

Mechanical models with elastic (Hookean springs) and viscous (Newtonian dashpots) elements were introduced to describe the linear viscoelastic deformation behavior of polymers. The Maxwell and the Kelvin-Voigt models are the most simple models that describe the stress relaxation of a viscoelastic solid and the creep behavior, respectively. A closer approach to the response of real polymers is achieved using combinations of several of these elements. Some examples are the standard-linear solid, that consists of a Maxwell unit in parallel with an extra spring; the Takayanagi model that takes into account the distinct phases of the polymer (either in an amorphous polymer blend or in a semicrystalline polymer with the amorphous and crystalline phases), or the generalized Maxwell model (a multi-element model), in which several elements are assembled in parallel taking into account that the relaxation occurs in a set, or spectrum, of relaxation-times[40,137]. On the other hand, the Debye-type models have been used in polymer physics to describe the dielectric but also the mechanical relaxation. To this latter type belongs the Havriliak-Negami equation, that describes the experimentally obtained storage (real part) and loss moduli (imaginary part) in the complex plane for each frequency of measurement. It usually applied after a previous time-temperature superposition of the viscoelastic data into a master-curve to describe the wider data range of frequencies the possible at the selected reference temperature[49]. The equation is an empirical relaxation function that expresses a superposition of individual relaxation-times by a distribution function[27,29,60,113,119]. Finally, to describe general viscoelastic behavior, the fractional models are also used with the subjacent idea of a generalized Maxwell or Kelvin-Voigt model but replacing the regular derivatives by fractional derivatives that could be related to the hierarchical nature of the relaxation processes[2,50,114].

Focusing in the multi-element models, the main interest lies on the calculation of the relaxation spectrum, since it can be used, together with the viscoelastic constants, to precisely describe the time-dependent part of the response of linearly viscoelastic materials, and to provide insight on the molecular morphology of the polymer. In the literature, one can find different procedures to determine the relaxation spectrum from experimental measurements since it cannot be obtained directly from experiments[9,10,35,51,131,138]. Additionally, in reference [138] Winter states that, despite spectra with discrete values are the output of the calculations, they are not meaningful by themselves. He presents a method to interconvert the discrete spectrum into a continuous one because the continuous spectrum is considered a representation with physical meaning on the macromolecular dynamics.

In the present work, we use experimental viscoelasic data on the storage and loss moduli in the range of frequencies from 1 to 100 rad/s and at temperatures from -100 to 100°C obtained through DMA, as in the previous chapter. A model based on a Generalized Maxwell (GM) approach is proposed to describe the experimental moduli. Data sets at different frequencies but at constant temperatures have been separately analyzed since no master curve from time-temperature superposition is not possible due to the inherent rheological complexity of the materials. By means of a curve-fitting procedure between the experimental data and the model, and using for the optimization a *Simulated Annealing* method, discrete spectra of relaxation-times have been obtained at different temperatures. In this way, very satisfactory agreement between the data and the model has been achieved for the case of polymeric bars of both LLDPE and EVOH, with the use of the simple GM model. Then, from the calculated discrete spectra at different temperatures, one can alanlyze distinguished features of the studied materials from the characteristic contributions at different relaxation-times. Conversely, for the case of polymeric films, the GM form by itself does not provide a good enough fit to the experimental data. We propose then a correction to the GM model in terms of an Eyring viscosity that results to be a good model to describe these materials stretched during the processing. In the Eyring theory, the newtonian viscosity present in the Maxwell element is substituted by a nonlinear stress-dependent viscosity. The non-linearlities are included in the numerical implementation to calculate the usual spectra with corrective terms. These corrective terms become relevant for some temperatures and for

some ranges of relaxation-times; in particular, when approaching the glass-transition temperature and below. Again, the calculated spectra at different temperatures show distinctive features of the polymeric whose structural origin can be glimpsed.

Along this chapter we obtain spectra at different temperatures for molded bar polymers of pure LLDPE and EVOH and films of the same materials. In the first place, we will center our attention in the differences between bars and films of pure materials, to elucidate what are the causes of the different mechanical behaviors, and speculate about the possible microscopic origins. In the second place, we apply the superposition principle and compare the predicted spectra for multilayered films and the calculated one from the experimental values of the storage and loss moduli. Again, the breakdown of the superposition is used as an indicator of additional morphological changes related to the confinement of the inner layers into sub-micrometric thicknesses, or interfacial effects in the contact between the two plastics.

3.2 Fundamentals

3.2.1 Molecular Motions and Transitions

The thermal energy available in the system determines the molecular mobility which enables the accommodation of macroscopic deformations. Therefore the viscoelasiticty of polymers has a strong dependence on temperature. Microscopically, the deformations require the rotation of segments of the chains and depend on the intramolecular and intermolecular interactions. These interactions result on energy barriers that restricts conformational changes of the main chain. When the temperature is raised, more thermal energy is available and more bonds in the structure become able to rotate. In this way, larger molecular rearrangements are allowed because the rate of change of conformations increases. Additionally, polymers also allow for mobility when secondary bonds are broken by applying stress.

The polymer's behavior changes from glass-like to rubber-like as the temperature is raised or the time-scale of the experiment is increased. The dependence on temperature of the relaxation modulus shows various regions: specifically, five regions of viscoelastic behavior can be identified for an ordinary amorphous polymer. The first region is the glassy region, in which the polymer's response is solid-like since only small and

fast displacements of the molecules from their equilibrium positions are possible. The glassy state can present a constant modulus but also various secondary sub-T_g transitions may be present. These secondary transitions may affect the impact strength of polymers. The second region corresponds to the glass-transition, in which typically the modulus drops a factor 1000 in $20 - 30°$C. This region can be interpreted as the onset of long-range, coordinated molecular motion because sufficient thermal energy is available to allow the movements in a coordinated manner. T_g itself has a notorious dependence with structure and other parameters. In the rubbery plateau region, which is the third transition when rising the temperature, the polymers exhibit long-range rubber elasticity. Two cases can be distinguished. If the polymer is linear, the modulus drops off slowly. However, if the polymer is cross-linked, it shows improved rubber elasticity with a modulus almost constant again. The semicrystalline polymers have some similar features to the cross-linked case because the crystalline regions behave as physical cross-links. The crystalline plateau extends until the melting point of the polymer and its height depends on the degree of crystallinity. In the rubbery region, the rapid and coordinated molecular motions are governed by the principles of reptation and diffusion. The fourth and fifth regions are the rubbery flow and the liquid flow regions, respectively. Increasing the temperature after the rubbery plateau, for amorphous polymers, the polymer is still elastic but also flows. Hence, for short time scale experiments, the physical entanglements do not relax. But, for longer scale experiments, the increased molecular motion permits assemblies of chains to move in a coordinated manner and thus flow. At still higher temperatures, the liquid flow region with increased thermal energy available consist of the polymer chains reptating out through entanglements rapidly and flow as individual molecules.

Hence, the molecular chemical and spatial configuration of a polymer determines its glass-transition and the relaxation mechanisms, which influence the deformation behavior of the polymer. In this way, the relaxation mechanisms, each representing specific molecular motions, provide the link between the molecular structure and the macroscopic deformation, and are commonly formally expressed through a spectrum of relaxation-times.

Experimentally, instead of measuring the stress relaxation, dynamic mechanical measurements as functions of frequency are generally employed to determine the modulus-

temperature curves. It is a simple procedure to study the influence of polymer structure on thermo-mechanical behavior and additionally in this kind of measurements the elastic and viscous forces are separately obtained.

In relation with the mentioned aspects, the polymers can be classified as thermorheologically simple or complex materials. For the simple materials the same temperature dependence is observed for all the relaxation-times associated with a relaxation mechanism and also the stress magnitudes show the same temperature dependence, which results in a time-temperature equivalence[137]. For thermorheological complex polymers, instead, the relaxation-times are not equally influenced by temperature. The origin is that, besides the primary transition governed by the main-chain mobility, there are the previously mentioned secondary transitions that involve movements of side-groups or smaller segments of the chain. The shape of the spectrum of relaxation-times reflects this complexity and the time-temperature superposition principle is no longer valid.

Semicrystalline polymers show thermorheological complexity as a sign of their internal structure. Only the amorphous portions go through the glass-transition while the crystalline portion remains hard. However, above the glass-transition temperature the relaxations mechanisms exhibited are related to the crystalline phase, and could be attributed to uncoordinated motions within the crystal lattice and to deformation of amorphous regions between crystal lamellae[17].

3.2.2 Molecular description of Polymer Viscoelasticity

A pure relaxation mode can be mechanically represented as a spring in series with a dashpot. The spring represents the inherent elasticity of the polymeric chains in the rubbery region

$$h \sim \frac{k_B T}{R_F^2} \tag{3.1}$$

where h is the spring constant of a polymeric strand of N Kuhn segments of length a, with a Flory radius $R_F \sim aN^{\nu}$, where $\nu = 1/2$ corresponds to ideal chain statistics (polymer melts) and $\nu \simeq 3/5$ applies to semi-dilute and dilute solutions. k_B is the Boltzmann constant and T, the absolute temperature. The spring constant macroscopically contributes to the Young modulus of the system E in an additive way, according to the theory of rubber elasticity. The dashpot represents the friction of the polymer

with the environment, resulting in a friction coefficient $\xi \sim \eta R_F \sim \eta a N^{3/5}$, according to the Stokes formula for the friction force a sphere of radius R_F in a fluid of viscosity η, at a negligible Reynolds number. This latter hypothesis is in the basis of the so-called Zimm model[31], mostly valid for semi-diluted solutions. Invoking force balance, namely, that the elastic force is compensated by the friction force, the relaxation of a deformation of a polymer strand satisfies

$$\eta R_F \frac{R}{\tau} \sim \frac{k_B T}{R_F^2} R \tag{3.2}$$

Here R is a characteristic deformation, taken as of the order of R_F, and R/τ is an estimate of the velocity. Hence, in this expression τ is an estimate of the relaxation-time of the deformation inflicted to the polymer, whose scaling form we readily obtain from eq. (3.2). It reads

$$\tau \sim \frac{\eta(T)\, R_F^3}{k_B T} = \frac{\eta(T)\, a^3 N^{9/5}}{k_B T} \equiv a(T) N^{9/5} \tag{3.3}$$

The so-called Rouse model[31], states that the friction coefficient does not scale with the Flory radius R_F but with the number of monomers in the chain, which all separately contribute to the friction, namely $\xi \sim \eta a N$. For this case, eq. (3.2) turns into

$$\eta a N \frac{R}{\tau} \sim \frac{k_B T}{R_F^2} R \tag{3.4}$$

since the friction coefficient of a monomer is estimated as scaling as ηa, also in agreement with Stokes formula. Furthermore, the chains behave ideally in melts, and as such also in the amorphous phase of a plastic solid in the rubbery plateau, therefore, $R_F \sim a N^{1/2}$ according to ref. [31]. Hence, the scaling form of the relaxation-time in the Rouse model reads

$$\tau \sim \frac{\eta(T)\, a^3 N^2}{k_B T} \equiv a(T) N^2 \tag{3.5}$$

However, in amorphous systems of entangled high molecular weight polymers, the relaxation of polymer deformations takes place through reptation[31,123]. In this limit, the relaxation-time is estimated as being

$$\tau \sim \frac{\eta(T)\, a^3 N^3}{N_e\, k_B T} \equiv a(T) N^3 \tag{3.6}$$

where N_e is the number of polymer Kuhn segments between entanglement points. N_e is estimated to be around 100. Hence, the crossover between Rouse to reptation behavior strongly depends on the molecular weight of the polymers. In semicrystalline polymers, the significant size is that of the threads of polymer giving rise to the amorphous fraction, which are much smaller than the original polymers themselves. Therefore, we expect that the relaxation of our systems to lay between these two limiting cases, namely, Rouse and Reptation. In general, we will write $\tau \sim a(T)N^{\gamma}$ with $\gamma = 9/5$ for semi-dilute solutions and $\gamma = 2$ or $\gamma = 3$ for polymer melts. The analysis done along this chapter considers the amorphous fraction of the solid polymer equivalent to a polymer melt and the latter exponent applies.

This simple estimate of the relaxation-time clearly reveals the essential elements of the polymer relaxation, which are the basis of the time-temperature superposition. On the one hand, the larger the polymer strand N, the larger the relaxation-time. On the other, the temperature dependence of the relaxation-time is contained in a prefactor $a(T)$ for all the polymer strands, regardless of their size. Therefore, the polydispersity in relaxation-times present in the amorphous fraction of a solid polymer is due to the polydispersity in the size of the different polymer strands and their different modes of motion. This statement should be valid at least in the rubbery plateau, where it is expected that the size-distribution remains constant between its limiting transition temperatures. Transitions in the system change the distribution of polymer elements contributing to the relaxation, breaking down the time-temperature superposition beyond the transitions[17].

Hence, for thermorheologically simple materials the temperature-dependence of viscoelastic behavior can be described using a time-shift factor (horizontal) and a modulus-shift factor (vertical) that make possible the superposition of dynamic moduli data obtained at different temperatures[73,129]. Accordingly, the scale transformation reads $E^*(\omega, T) = bE^*(\omega/a, T')$. This procedure avoids the difficulty of measuring polymers behavior over broad range of time by the fact that data obtained at several temperatures can be shifted to a common reference temperature. In this way, a master curve that describe the viscoelasticity can be generated since the curves of dynamic moduli versus relaxation-time (or frequency) obtained at different temperatures are superimposable in a double logarithmic plot.

However, for polymers exhibiting thermorhological complexity these simple relationships are no longer valid since the relaxation-times are not equally influenced by temperature. For this kind of materials, the inherent complex molecular morphology can arise as a non-simple response. The complexity is the result of the cooperative effect of a large number of different *species* (polymer segments of different length or nature) accounting for the polydispersity of the strands of polymers forming the amorphous fraction of the solid. Thus, each of these strands, either connecting crystals, loose loops, tails with dangling ends, or branches, etc. is considered to contribute with a distinctive *independent* response, whose cumulative effect is measured in the mechanical experiment. Such independence may be questioned[28] due to nonlinear couplings, as we will see here in the analysis of thin films. In addition, each of these strands does not respond in a single mode of relaxation but through a collection of *modes of motion*, commonly referred to as Rouse modes, which can be more or less hampered by the physical constraints of the chain environment, and excited by the external action of the stress or electric fields.

3.3 Model

Linear viscoelasticity can be described by rather simple models which traditionally have been assimilated to mechanical analogs consisting of a combination of pure elastic and viscous elements[40,137].

A Maxwell element is a mechanical analog of a collection of modes with the same relaxation-time, represented by a spring in series with a dash-pot, both holding the same stress. The *constitutive* equation that describes this element in its differential form can be written as

$$\frac{\dot{\sigma}}{E} + \frac{\sigma}{\eta} = \dot{\varepsilon} \tag{3.7}$$

where σ represents the stress and $\dot{\sigma}$ the stress rate, ε and $\dot{\varepsilon}$ stand for the deformation (strain) and the deformation rate, respectively, η is the viscosity and E is Young's modulus. For a sudden constant strain ε_0 at $t = 0$, the linear differential equation (3.7) has a solution of the form

$$\sigma(t) = \sigma_0 e^{-t/\tau} \tag{3.8}$$

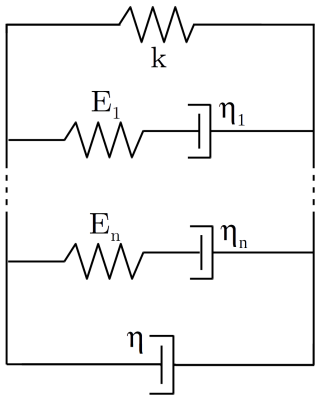

Figure 3.1: *Mechanical analogy to the Maxwell type model*

where $\tau = \eta/E$ is the relaxation-time whose microscopic description is given in eq. (3.5). σ_0 is the initial stress, related to the strain by $\sigma_0 = E\varepsilon_0$. Then, the time dependent ratio of tensile stress to strain, $\sigma(t)/\varepsilon_0$, known as the relaxation modulus $\tilde{E}$, is

$$\tilde{E}(t) = Ee^{-t/\tau}\,\Theta(t) \tag{3.9}$$

where the Heaviside Θ-function ensures the causality of the response. As a consequence of causality, the kernel $\tilde{E}(t)$ straightforwardly satisfies the Kramers-Kronig relations of its Laplace transform[13], writing $s = i\omega$, with s being the Laplace variable and ω, the frequency.

In general, if the system is subject to a time-dependent strain $\varepsilon(t)$ the response can be written in an integral form

$$\sigma(t) = \int_0^t dt'\,\tilde{E}(t-t')\dot{\varepsilon}(t') \tag{3.10}$$

where $\tilde{E}(t)$ is the Green's function of eq. (3.7), given precisely by eq. (3.9). Eq. (3.10) implies that the relation between stress and strain is linear. To introduce the harmonic analysis, let us assume that the Maxwell element is subject to periodic deformations of the type $\varepsilon = \varepsilon_0 \sin(\omega t)$. Then the response can be expressed in terms of frequency. The response can be embedded in a complex modulus, E^* which reads

$$E^*(\omega) \equiv E'(\omega) + iE"(\omega) = \frac{i\omega\tau E}{1+i\omega\tau} \tag{3.11}$$

which here is defined from the relationship $\sigma^* = E^*\varepsilon^*$, using $\varepsilon(t) = \varepsilon_0 e^{i\omega t}$. The real and

imaginary parts of the relaxation modulus are related to the so-called *storage*, $E'(\omega)$, and *loss*, $E"(\omega)$, moduli, which, respectively, describe the reversible and irreversible parts of the work done on the system in a cycle. In Appendix A.2 we give the details of an operational interpretation of the storage and loss moduli valid for general nonlinear systems.

The Maxwell model is clearly an idealization that can only describe relaxation processes with a single relaxation-time. For a real system, however, one has to consider that the response is the combination of multiple relaxation processes linearly superposed. Formally, one assumes that

$$\sigma(t) \quad = \quad \int_0^t dt' \left[\int_0^\infty dn\, P(n)\, E_n\, e^{-(t-t')/\tau_n} \right] \dot{\varepsilon}(t') \tag{3.12}$$

where we have introduced the subindex n to characterize the relaxation-time $\tau_n = a(T)n^\gamma$, as it would corresponds to the relaxation of n monomers involved in the motion. Here, however, is a dummy parameter of integration. Moreover, E_n is the Young modulus of the n mode, which scales as $E_n \sim k_B T/N^{2\nu}$. $P(n)$ is the distribution of the species of size n in the system, which we refer to as the spectrum of relaxation-times. $P(n)$ is positive-definite and such that

$$\int_0^\infty dn\, P(n) = \mathcal{N} \tag{3.13}$$

where $\mathcal{N}$ is the total number of modes in the system. Eq.(3.12) is known as the Generalized Maxwell model for a continuous spectrum of relaxation-times. A sketch of the discrete version is shown in Figure 3.1. In this discrete version, which will be eventually implemented in this work, the different Maxwell elements are in parallel, which effectively corresponds to the superposition implicit in eq.(3.12). After some algebra, the complex modulus for the Generalized Maxwell model reads

$$E'(\omega) = \int_0^\infty \frac{(\omega\tau)^2 H(\tau)}{1+(\omega\tau)^2} d\ln\tau \tag{3.14}$$

$$E''(\omega) = \int_0^\infty \frac{(\omega\tau) H(\tau)}{1+(\omega\tau)^2} d\ln\tau \tag{3.15}$$

The detailed derivation of eq. (3.14) and (3.15) is given in Appendix A.1. The func-

tion $H(\tau)$ summarizes the combination of the spectrum of relaxation-times $P(n)$, the Young modulus of the n modes, E_n, but also the transformation $dn \sim nd\ln\tau$, whose proportionality is valid regardless the exponent γ. It is important to realize that $H(\tau)$ is the only function that can be experimentally determined if no additional information of the dependence of E_n on n is a priori known. In the idealized case discussed so far, which should be valid only in the rubbery plateau, $E_n \sim k_BT/n$ (Rouse model) and, therefore, $H(\tau)d\ln\tau \simeq k_BTP(n)dn$.

3.3.1 Nonlinear Model for Films

In the forthcoming analysis of the experimental data on the relaxation of thin films used in this work, we will see that the Generalized Maxwell model (GM), described so far, cannot give a precise account of the observed response, even for the reduced range of frequencies of our experimental data. Moreover, in the previous chapter we have emphasized how crucial is in the analysis the explicit consideration of the draw rate, i.e., the processing conditions. We have seen, through observation of the properties, that the final material is strongly non isotropic depending on whether the *machine* or the *cross* direction is tested. Therefore, there are strong reasons to believe that the system is particularly stretched in the machine direction, even to cause morphological changes in the spherulites (or discoids), responsible for the anisotropy in the mechanical response.

Hence, we propose a nonlinear modification in the Maxwell model along the lines established by Tobolsky and Eyring in their analysis of the mechanical properties near the yield, which would be the situation of parts of the system after the processing. Their phenomenological model consists of a Maxwell element in which the dashpot responds with a non-Newtonian stress-dependent viscosity $\eta(\sigma)$[33,130]. The model can be written modifying eq.(3.7) in the form

$$\frac{\dot{\sigma}}{E} + \frac{\sigma_v}{\eta}\sinh\frac{\sigma}{\sigma_v} = \dot{\varepsilon} \tag{3.16}$$

where σ_v is a phenomenological constant characterizing the stress at yield. In ref. [130] specific molecular interpretation is given to the constants in eq. (3.16). Notice that the linear behavior is recovered at $\sigma/\sigma_v \to 0$.

This nonlinear equation predicts a logarithmic relaxation at initial times when the initial stress σ_0 is larger than σ_v, of the form

$$\sigma(t) = -\sigma_v \ln\left(\frac{t}{2\tau} + e^{-\sigma_0/\sigma_v}\right) \tag{3.17}$$

where $\tau = \eta/E$ is here the same as in the Maxwell model, with the parameters E and η defined in eq. (3.16). After some initial time $t \sim 2\tau \exp[-\sigma_0/\sigma_v]$, the decay is purely logarithmic $\sigma(t) = -\ln(t/2\tau)$. The crossover towards the linear relaxation occurs at a time $t \sim 2\tau/e \sim 1$. After this initial time, the relaxation would be similar to the corresponding Maxwell element. The reader is addressed to Appendix A.3 for the details.

However, we do not expect a strong deviation from the linear regime in our experiments done at small strain. Therefore, we use a Taylor expansion of the second term in the right hand side of eq. (3.16), and retain the first nonlinear contribution to the stress. Within this new model, a very good agreement with the experimental data, particularly for the thinner films, either of pure components or sandwiches, is achieved. Hence, in eq. (3.16) we replace $\sinh(\sigma \to 0) \simeq \sigma + \frac{\sigma^3}{3!}$, and perturbatively solve the differential equation in terms of the amplitude of the strain, which enters into the description due to the nonlinear coupling. The detailed calculation is shown in Appendix A.3. The modified storage and loss moduli read as eqs. (3.14) and (3.15) plus correction terms as follows

$$E'(\omega) = \int_0^\infty d\ln\tau \left(\frac{H(\tau)(\omega\tau)^2}{1+(\omega\tau)^2} - H_1(\tau)\frac{(\omega\tau)^4}{(1+(\omega\tau)^2)^3}\right) \tag{3.18}$$

$$E''(\omega) = \int_0^\infty d\ln\tau \left(\frac{H(\tau)\omega\tau}{1+(\omega\tau)^2} - \frac{1}{2}H_1(\tau)\frac{(\omega\tau)^3(1-(\omega\tau)^2)}{(1+(\omega\tau)^2)^3}\right) \tag{3.19}$$

where $H(\tau)$ is the spectrum of relaxation-times as in the Maxwell model. However, due to the presence of the nonlinear contributions, the knowledge of the spectrum is not enough to characterize the response of the system. One needs, in addition, the knowledge of a second distribution accounting for the impact of the non-linearities, namely $H_1(\tau)$.

3.3.2 Numerical Procedure

We determine the discrete spectrum of relaxation-times through a curve-fitting procedure with no regularization term, as suggested in ref. [138]. The least-squares method is carried out using the experimental measurements obtained of $E'(\omega)$ and $E''(\omega)$ and the model given by eqs. (3.14) and (3.15). Notice that, in addition, we have introduced the limiting cases of pure elasticity and pure viscosity plus two additional terms, accounting for the effect of the tails of the distribution of relaxation-times. Leaving aside for the moment the nonlinear correction, the function to be minimized is

$$\begin{aligned}\mathcal{E} \equiv &\sum_i^N \left[1 - \frac{1}{E'_{\exp}(\omega_i)}\left(\omega_i^2 R'_1 + \sum_\alpha^M \frac{(\omega_i\tau_\alpha)^2 H(\tau_\alpha)}{1+(\omega_i\tau_\alpha)^2}\Delta\ln\tau + k\right)\right] \\ &+ \sum_i^N \left[1 - \frac{1}{E''_{\exp}(\omega_i)}\left(\omega_i\eta + \sum_\alpha^M \frac{(\omega_i\tau_\alpha) H(\tau_\alpha)}{1+(\omega_i\tau_\alpha)^2}\Delta\ln\tau + \frac{R_2"}{\omega_i}\right)\right]\end{aligned} \tag{3.20}$$

where ω_i with $i = 1...N$ stands for the set of experimental frequencies. The range of frequencies available is $\omega \in [1, 100]\, s^{-1}$. In turn, τ_α with $\alpha = 1, ..., M$, α being an integer, is the ensemble of relaxation-times that we use for the fitting. Given the maximum and minimum relaxation-times, τ_{max} and τ_{min}, respectively, the values of τ_α that are representative of each relaxation-time interval are given by

$$\ln\tau_\alpha = \ln\tau_{min} + \frac{\ln\tau_{max} - \ln\tau_{min}}{M-1}\left(\alpha - \frac{1}{2}\right) \equiv \ln\tau_{min} + \Delta\ln\tau\left(\alpha - \frac{1}{2}\right) \tag{3.21}$$

where we stress that $\Delta\ln\tau$ is constant.

Moreover, since the range of experimental frequencies is limited, the information about the spectrum that we can extract is also very limited. Hence, if we bear in mind that $\omega_{min} = 1\, s^{-1}$ and $\omega_{max} = 100\, s^{-1}$, we choose the lowest relaxation-time $\tau_{min} = 10^{-2}/\omega_{max} = 10^{-4}\, s$, while the larger relaxation-time is chosen $\tau_{max} = 10^2/\omega_{min} = 10^2\, s$. Then, for $\tau < \tau_{min}$ it is always true that $\omega_i\tau \leq 10^{-2}$ and the response functions can be readily approximated yielding the following expressions with a trivial ω-dependence

$$\int_0^{\tau_{min}} \frac{(\omega\tau)^2 H(\tau)}{1+(\omega\tau)^2} d\ln\tau \simeq \omega^2 \int_0^{\tau_{min}} d\ln\tau\, \tau^2 H(\tau) \equiv \omega^2 R'_1 \tag{3.22}$$

$$\int_0^{\tau_{min}} \frac{(\omega\tau) H(\tau)}{1+(\omega\tau)^2} d\ln\tau \simeq \omega \int_0^{\tau_{min}} d\ln\tau\, \tau H(\tau) \equiv \omega\eta \tag{3.23}$$

Repeating the argument for $\tau > \tau_{max}$ it is always true that $\omega_i \tau \geq 10^2$, and we encounter

$$\int_{\tau_{max}}^{\infty} \frac{(\omega\tau)^2 H(\tau)}{1+(\omega\tau)^2} d\ln\tau \simeq \int_{\tau_{max}}^{\infty} d\ln\tau\, H(\tau) \equiv k \tag{3.24}$$

$$\int_{\tau_{max}}^{\infty} \frac{(\omega\tau) H(\tau)}{1+(\omega\tau)^2} d\ln\tau \simeq \frac{1}{\omega}\int_{\tau_{max}}^{\infty} d\ln\tau \frac{H(\tau)}{\tau} \equiv \frac{R_2"}{\omega} \tag{3.25}$$

In all cases, the error made in the use of the asymptotic expansion instead of the complete expression is of the order of 10^{-4} for the chosen values of the relaxation-time limits and the range of experimental frequencies. Expressions (3.22)-(3.25) are valid always that the frequency is kept inside the aforementioned range and do not represent the functional response of the system over the entire spectrum of frequencies. As we see, we can only obtain information about some *moments* of the relaxation-time distribution for the short and long relaxation-time limit. The explicit calculation of $H(\tau)$ outside the limits τ_{min} and τ_{max} defined would be nonsense without more data at lower and higher frequencies.

The parameters that we need to set a priori in our procedure are τ_{min} and τ_{max} and the total number of relaxation-time intervals M. However, if this number of points where we aim at obtaining the spectrum exceeds the number of frequencies, for which experimental data exist, the problem is then ill-posed. This implies that different spectra may in principle yield the same viscoelastic response at the set of the experimental frequencies. There are several methods to select the plausible spectrum but all of them require additional insight to be added to the problem of minimization of eq. (3.20). Honerkamp *et al.*[51], for instance, add a *Tikhonov* regularization term that smoothes out the obtained spectra. Others introduce terms of the type $H \log H$ making use of the hypothesis that the system would naturally prefer a homogeneous distribution of relaxation-times, as an ideal gas in a container tends to a homogeneous density, which seems unjustified in our case. The reader is addressed to ref. [104] to find a detailed description of different regularization methods commonly employed. In our case, we have checked that the spectra obtained with the annealing method, described below, is independent of the initial conditions. Effectively, we have repeated the calculation of the spectra about 10 times and found that the results are practically indiscernible.

In order to minimize the cost function we use the so-called *simulated annealing* technique. This meta-heuristic technique provides a good solution and, as implemented

here, enforces that $H(\tau)$ is positive-definite. One cannot guarantee that the solution found is the global optimum but still provides a more than a plausible answer to the fundamental question. The detailed description of the numerical procedure is given in Appendix A.4. Also in the same appendix we show the verifications carried out to assure the robustness of the method even outside the range of relaxation-times $[1/\omega_{max}, 1/\omega_{min}]$.

Finally, when we consider the nonlinear corrections, we introduce the nonlinear Eyring type modifications in the model, as in eqs. (3.18) and (3.19), and follow the numerical procedure. In the nonlinear case, however, in addition to the natural relaxation-time spectra $H(\tau)$, a second distribution $H_1(\tau)$ is also obtained.

3.4 Results and Discussion

3.4.1 Relaxation of pure LLDPE and EVOH bars

The viscoelastic response of LLDPE and EVOH compression molded bars, i.e. bulk polymers, can be described using the GM model, without nonlinear corrections, in all the experimentally analyzed temperature range. The curves for the storage and loss moduli predicted from the model, eqs. (3.14) and (3.15), properly match the experimental data, as it can be seen in Figure 3.2a and Figure 3.2b.

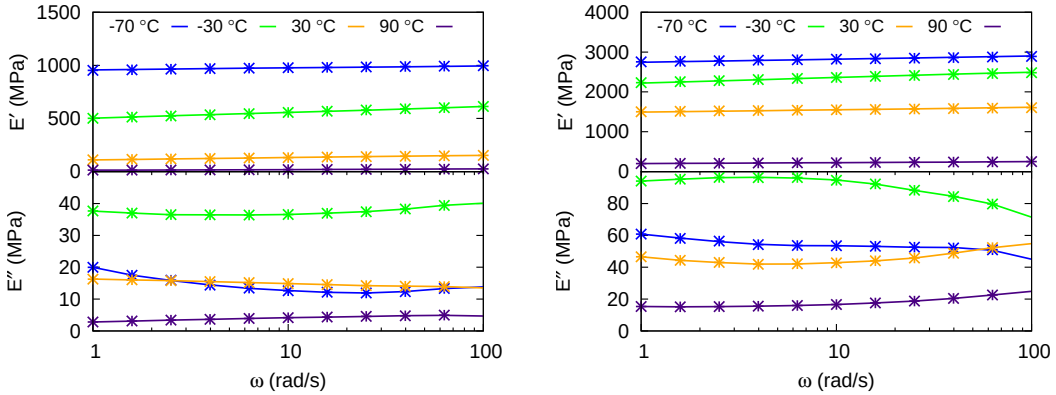

(a) *LLDPE bar* **(b)** *EVOH bar*

Figure 3.2: *Storage (E') and loss (E'') moduli, solid lines are the model prediction and points are the experimental data at temperatures of -70° C, -30° C, 30° C and 90° C.*

The fitting of the data using the GM model and setting $M = 100$ yields a discrete spectrum, $H(\tau_\alpha)$, at the selected $\alpha = 1, \ldots, M$ relaxation-times, according to eq. (3.21).

We obtain a rather rough distribution of relaxation-times (see Figure 3.3), since no smoothing has been included in the cost function. In general, we have to distinguish between three regions limited by $1/\omega_{max}$ and $1/\omega_{min}$. Within the region inside the range $1/\omega_{max} < \tau < 1/\omega_{min}$ lay the most relevant part of the spectra for the range of frequencies experimentally studied. However, restricting the minimization of the cost function only inside this region yields spurious peaks near the edges of the interval, despite the use of the asymptotic terms given in eqs. from (3.22) to (3.25). This is due to the fact that, on the one hand, the long relaxation-time part of the spectrum is relevant at the analyzed temperatures and, on the other, that variations in the position of a peak outside the most sensitive range do not cause a significant variation of the cost function (see Appendix A.4 for details about the sensitivity of the method in different regions of the spectrum). In Figure 3.3 we show the spectra obtained for LLDPE, molded in a bar, for two relaxation-time ranges and different number M of points. Notice that the implemented simulated annealing is able to locate peaks outside the most sensitive region (see also Appendix A.4, where we explain the procedure and checks done with regard to this point). However, we see that the narrower spectrum has a dominant peak next to the upper limit τ_{max}, while the wider spectrum does not. This is the case because, in this region of low sensitivity the wider spectrum distributes the effect of long relaxation-times in a wider range. Instead, the narrower spectrum has the handicap of a residual sensitivity of the order of $1/\tau$ near to the upper limit of the spectrum, which cannot be gathered into the limiting behaviors, namely k and R_2''. Hence, a spuriously high peak is produced if the upper limit is placed right in this region of residual sensitivity. Therefore, the evaluation of wider spectra permits to avoid this problem. We have thus determined the spectra in a wider relaxation-time range $\tau \in [10^{-7}, 10^{7}]$, but show the spectra within the relevant range, $\tau_{min} = 10^{-4}s$ and $\tau_{max} = 10^{2}s$, integrating the tails according to the asymptotic contributions in eqs. (3.22) - (3.25). Furthermore, it is also remarkable from Figure 3.3 that a part of the spectrum within the most sensitive region is repeatedly obtained from different initial conditions as well as ranges of relaxation-times. This fact implies that physical insight can be inferred from the fitting of the spectra of relaxation-times performed in this chapter.

Let us first consider the obtained spectra and asymptotic parameters for the two

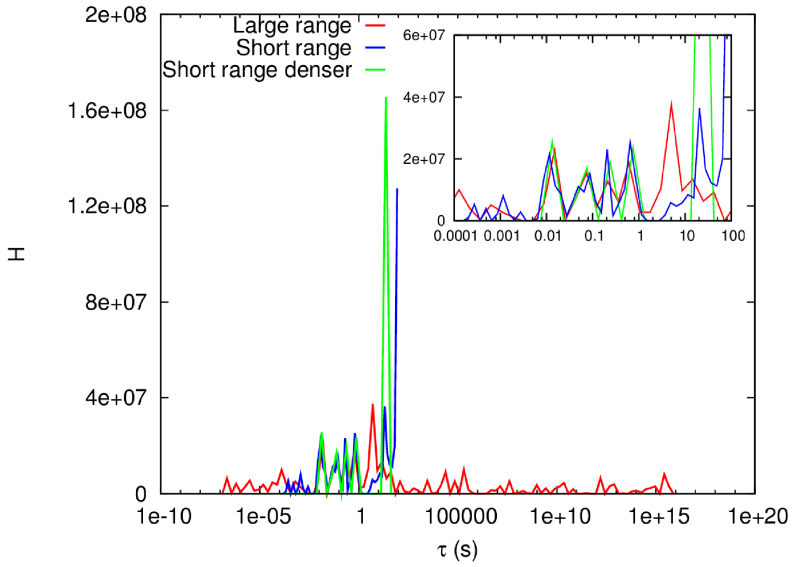

Figure 3.3: *Comparison of spectra obtained by the Simulation Annealing thechnique for LLDPE bar at* $30°C$*. The line corresponding to the large range (red) shows the peaks obtained when the* τ *range is* $[10^{-7}, 10^{16}]s$ *and* $\Delta \ln \tau \approx 0.5$*. The line for the short range (blue) shows the peaks obtained when* τ *is between* $[10^{-4}, 10^{2}]s$ *and* $\Delta \ln \tau \approx 0.5$*. The line corresponfing to the short range but with denser distribution of points (green) shows the peaks obtained when* τ *is between* $[10^{-4}, 10^{2}]s$ *and* $\Delta \ln \tau \approx 0.25$*.*

pure materials for different temperatures, to elucidate the most salient features of the spectra.

In Figure 3.4a we can see the spectra for LLDPE in three selected temperatures, namely, 90°C, 70°, and 50°C, which lay in the rubbery plateau, far from the assumed glass-transition temperature −30°C. In Figure 3.4b we show the spectra in the crossover region, for temperatures 30°C, 10°, and −10°C. Finally, in Figure 3.4c, we indicate the spectra at the glass-transition temperature and below, −30°C, −50°, and −70°C. The asymptotic parameters in the whole range of temperatures are given in Figure 3.5. The γ- and melt transition temperatures for this material, reported around −120°C and 120°C, respectively, lay outside the studied temperature range.

At high temperature, according to Figure 3.4a, one finds spectra essentially composed by a group of three well-defined peaks at 0.015s, 0.07s, and 0.5s. We also observe an isolated peak at around 8s. We observe that the spectrum is overall low, due to the softening of the material near the melt transition, but hardens as the temperature decreases. These peaks may correspond to the relaxation of characteristic polymeric threads on the amorphous phase, like bridges between crystallites or closed loops on them, according to the usual interpretation of the origin of the relaxation in semicrys-

talline materials[17]. However, without additional microscopic information, it would be reckless to pretend an association between the peaks and a particular microscopic mode. Furthermore, one should take into account that we observe no shift of the peaks with the temperature, as it would be prescribed by the strict application of eq. (3.5) or (3.6). Moreover, a rubbery material would also show a storage modulus that increases proportionally to the temperature, according to eq. (3.1). Hence, we should not expect a classical rubbery behavior of the material in this region.

The time-temperature superposition is based on the analogy between the spectra at different temperatures as introduced in Subsection 3.2.2. The so-called *thermorheological simplicity* is based on the hypothesis that the distribution of modes in the system is invariant with the temperature. Since we characterize the modes with the relaxation-time τ itself, our function $H(\tau, T)d\ln\tau$ for a system displaying thermorheological simplicity would be shifted and rescaled with a temperature change. Hence, the rheological simplicity can be expressed as

$$H(\tau, T)d\ln\tau = bH(a\tau, T')d\ln\tau \tag{3.26}$$

The parameters a and b are functions of both temperatures T and T'. Therefore, with regard to a time-temperature superposition, one can proceed by calculating the shift factor ($\ln a$, since we refer the shift in a logarithmic scale) and the rescaling factor b such that the two compared spectra are virtually the same. These factors are then the ones required to overlap the experimental data on $E^*(\omega)$ into a single master curve, if such underlying thermorheological simplicity exists in the material. Back to Figure 3.4a, we have calculated these shift and scale factors for the three temperatures. We find that, with the precision of our calculation, no shift with temperature is observed. Moreover, we see that the spectra are rather similar if the ones of 70°C and 90°C are respectively scaled by a factor 1.7 and 4.25 and compared with the spectrum of 50°C. Some differences between the relative heights of the first and fourth peaks are the more noticeable discrepancies. When the calculated factors are applied to the respective $E'(\omega, T)$, the resulting curves are rather close to each other. However, the differences are more relatively significant for the $E"(\omega, T)$ curves. Hence, we can state that i) the peaks indeed correspond to a rather stable distribution of modes of motion, although

the temperature-dependence of the spring constant h and of the relaxation-time are not as suggested by the theory discussed in subsection 3.2.2. Furthermore, ii) no time-temperature superposition can be achieved in view of the lack of sufficient analogy between the relaxation-time distributions at different temperatures.

As mentioned, Figure 3.4b shows how the relaxation-time spectra vary when we approach the glass-transition temperature. In comparison with the rubbery region just discussed, the part of the spectra, $\tau < 1$s, increases as the temperature is lowered. New peaks appear at around $\tau \simeq 10^{-3}$s, and $\tau \simeq 10^{-4}$s well below the position of the first peak in the rubbery region. Moreover, above $\tau \simeq 0.1$s also new peaks arise. Furthermore, we observe that the height of the fourth peak at around 10s, is lowered and broadened. These changes can be seen as the signature of structural modifications of the material taking place with the decrease of the temperature. They could be interpreted as the appearance of hindrances in the motion of the longest strands of polymer, particularly if believed that the peak at 10s is due to the relaxation of long polymer strands, possibly bridges between crystallites, although this statement is a mere speculation, lacking of microscopic confirmation. One outcome of the increase of the mechanical hindrances is the overall rise of the spectra towards the lowest relaxation-time region and the broadening of the spectra. When a polymer strand is mechanically hindered in a given intermediate monomer, it is as if the system loses one long relaxation-time mode in favor of two shorter relaxation-time modes, and that occur in a random manner due to the intrinsic randomness of the location of the hindrances. In this sense, it is particularly interesting the location of a new peak in the region $1 < \tau < 10$s, where before no mode existed. In this crossover region this range of the spectra are significantly populated, even affecting the third peak, who looses its identity, being divided into two or more peaks and separated from the others by shallow valleys. Therefore, we can state that around 30°C the effects of hindrances are the most relevant microscopic transformation. The hardening of the individual modes with the decrease of the temperature is also noticeable.

Figure 3.4c shows the spectra at the glass-transition temperature -30°C and below, at -50°C and -70°C. Right at T_g we observe an overall enhancement of the spectrum, particularly in the region of low relaxation-time. It is interesting the fact that the new peak at $\tau \simeq 10^{-3}$s is significantly enhanced. Moreover, we also observe a rise

of the spectrum at the other side, that is, at $\tau \simeq 10^2$s, right on the border of the selected relaxation-time range. At temperatures below T_g the spectra in the center of the analyzed region is slightly lower than at the transition. However, we see an increase of the contributions at the low and high relaxation-time region. Particularly, a new peak increases at around $\tau \simeq 40$s. Hence, we consider that below T_g the relaxation mechanisms also change. In this sense, it is interesting to remind the existing debate on whether the true glass-transition temperature for the LLDPE should be located at the β-transition around -30°C or, more properly much below, at the mentioned γ-transition[16,124]. Boyer[123], proposes that there are two glass-transition temperatures: a low T_g, which should be at around -80°C, corresponding to the true glass-transition for a completely amorphous sample of polyethylene, and an upper T_g, located around -30°C, which would correspond to the glass-transition of a semicrystalline sample. We assumed this interpretation in our analysis. Moreover, in view also of Figure 3.5, the high values of the asymptotic coefficients k and R_1' in this region sub-T_g, are a clear signature of the broadening of the spectrum, towards regions where the spectrum have been lumped into few coefficients. We will discuss these coefficients in more detail below (the numerical values of these coefficients can be found in Appendix A.5).

In Figure 3.5, the behavior of the calculated asymptotic coefficients is presented. In general, we see that the elastic contributions k and R_1', corresponding, respectively, to the effects on E' at the regions $\tau > \tau_{max}$ and $\tau < \tau_{min}$, are small at the rubbery region. Their behavior changes with the temperature in the aforementioned crossover region, which we may consider starting below 50°C, and ending at about -30°C, right at T_g. In this crossover region, k progressively increases more rapidly with the decrease of T while R_1' shows an inflection. As far as k is concerned, we observe that below T_g its variation with the temperature is rather linear and increases when decreasing T. On the other hand, at the rubbery region, k is practically constant. Notice the small values of R_1' compared to k. With regard to the loss modulus asymptotic coefficients, we observe again that the contribution of the $\tau > \tau_{max}$ region, namely R_2", is significantly more important than the $\tau < \tau_{min}$, embedded in η. However, η shows a very interesting behavior. On the one hand, around 50°C η we identify a broad peak. Moreover, below -30°C this coefficient is low and practically constant. One cal also observe a sharp peak at around -10°C. The crossover region between the aforementioned temperatures 50°C

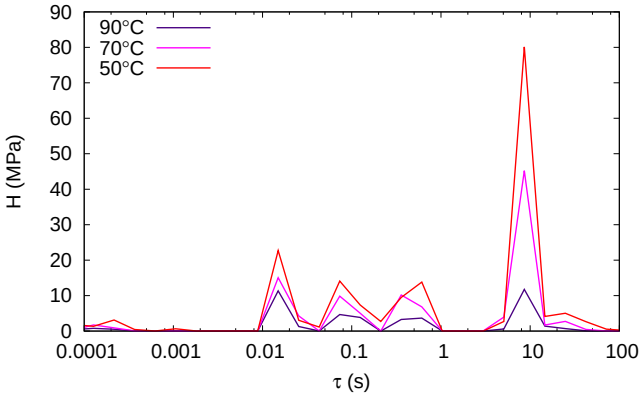

(a) *LLDPE bar in the rubbery region.*

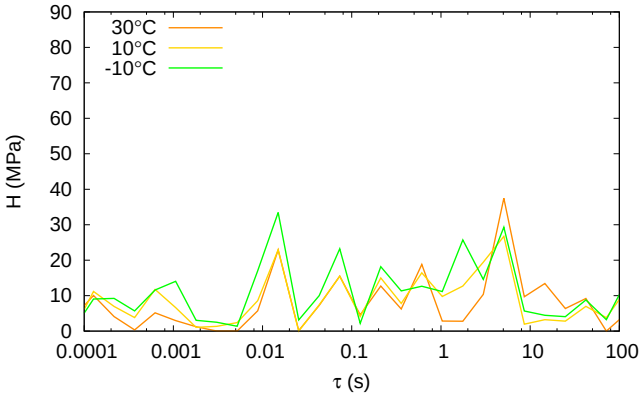

(b) *LLDPE bar in the crossover region.*

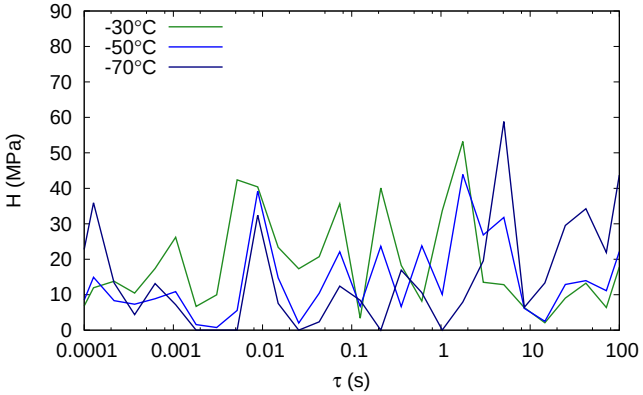

(c) *LLDPE bar in the glass region.*

Figure 3.4: *Time spectra for LLDPE bar at the studied temperatures of (a): 90° C, 70° C, 50° C, (b): 30° C, 10° C, -10° C, and (c): -30° C, -50° C, -70° C.*

and -30°C, corresponds to the region between these two peaks. We want to point out that the features of η are not visible in the direct analysis of $\tan\delta$, and permit to locate effects localized at the short relaxation-time of the spectra which are masked by the use of E' and E", which involve the whole spectrum of relaxation-times. Finally, if data

would allow us to integrate the spectrum over the whole relaxation-time distribution, we could have access to the true viscosity of the system $\eta_{visc} = \int_0^\infty d\ln\tau\, \tau H(\tau)$, which should agree with $E"(\omega \to 0)$. In the same way, the Young modulus of the material could be obtained as $k_{Young} = \int_0^\infty d\ln\tau\, H(\tau)$, which should agree with $E'(\omega \to \infty)$. These relationships are useful when interpreting the physical content in the asymptotic coefficients, as we attempt below.

The relationship between the asymptotic coefficients and moments of the relaxation-time distribution $H(\tau)$ is interesting by itself. Unfortunately, the limited range of frequencies does not allow for a calculation of the moments of H over the whole relaxation-time range and obtain relevant parameters as the true viscosity and Young modulus of the systems, just mentioned. Thus, we have to analyze them with regard to the portion of the relaxation-time domain where they are well defined. The existing similitude between the behavior of k and E', as well as between η and $E"$ suggests that there is valuable information in these coefficients to describe the transitions, in analogy with the extended use of $\tan\delta$[137] to this end. Let us propose two different coefficients bound to two separate regions of the relaxation-time domain. In the first place $\mathcal{R}_0$ is analogous to the ratio η/R_1', but we define this coefficient including part of the calculated spectrum up to a dividing relaxation-time $\tau_{min} < \tau_c < \tau_{max}$, which we choose around the mid of the spectrum as $\tau_c = 0.1$. Thus, the definition is

$$\mathcal{R}_0 \equiv \frac{\eta}{R_1'} = \frac{\int_0^{\tau_c} d\ln\tau\, \tau H(\tau)}{\int_0^{\tau_c} d\ln\tau\, \tau^2 H(\tau)} \equiv \frac{\langle\tau\rangle_0}{\langle\tau^2\rangle_0} \tag{3.27}$$

This ratio has dimensions of $1/\tau$. In the same way, we can define the ratio $R_2"/k$, which has the same dimensions of $1/\tau$, and covers the opposite side of the spectra (τ_c, ∞)

$$\mathcal{R}_\infty \equiv \frac{k}{R_2"} = \frac{\int_{\tau_c}^\infty d\ln\tau\, H(\tau)}{\int_{\tau_c}^\infty d\ln\tau\, \frac{1}{\tau} H(\tau)} \equiv \frac{\langle\tau^0\rangle_\infty}{\langle\tau^{-1}\rangle_\infty} \tag{3.28}$$

These coefficients contain complementary information to that of $\tan\delta$.

In Figures 3.5 we have also plotted $\mathcal{R}_0$ and $\mathcal{R}_\infty$ as functions of the temperature for the LLDPE bar. In the first place, we observe that both $\mathcal{R}_0$ and $\mathcal{R}_\infty$ have a distinctive peak at $-30°$C, which can be readily attributed to the glass-transition temperature (β-transition[17]), also in agreement with the interpretation from $\tan\delta$, as given in Figure 2.4 in Section 2.4.1. We can infer that at the transition temperature the weight

of the low relaxation-time part of the spectrum (left hand-side of the spectrum) is displaced towards even lower relaxation-times and, simultaneously, the right hand-side of the spectrum suffers a similar shift towards lower relaxation-times. Therefore, the β-transition for this material can be interpreted as a generalized shift of the spectrum towards low relaxation-times, in contrast to the interpretation that suggest that the peaks are compatible with the narrowing of the spectrum[16,17]. The general shift to the left hand-side of the spectrum when lowering the temperature near the β-transition would be compatible with the appearance of hindrances that reduce the relaxation-times of the preexisting treads of polymer, as we have already argued.

In the second place, as the temperature increases above -30°C, $\mathcal{R}_0$ progressively decreases, indicating that the weight of the spectrum is being displaced towards larger relaxation-times. At the same time, $\mathcal{R}_\infty$ progressively increases, which indicates the opposite tendency for the relaxation-times in this side of the spectrum. Hence, in this region, which we have identified as the crossover region, the material seems to concentrate the relaxation into a narrower window. The decrease of $\mathcal{R}_0$ proceeds as the temperature increases up to 50°C, where the narrowing of the spectrum seems to end. Finally, above 50°C, $\mathcal{R}_0$ rises again while $\mathcal{R}_\infty$ continues growing. This could be the signature that the material approaches the α-transition (assumed to be at around 75°C), as seen in Figure 2.4 in Section 2.4.1. However, the possible peak lays outside the studied temperature range.

The EVOH bar has an overall analogous behavior as the LLDPE, with some peculiarities related to this material. In principle, the glass-transition temperature of EVOH is customarily located at around 55°C[20]. Moreover, EVOH is considered to form hydrogen bonds between polymer threads, giving particular mechanical and thermodynamic properties to the material as, for instance, the high glass-transition temperature and a high Young modulus (compare, for example, the size of the peaks in Figures 3.4a and 3.6a). Assuming the aforementioned T_g, in Figure 3.6a we gather the spectra in the crossover region, according to the previous analysis of the LLDPE. The crossover region is characterized by an increase of the size of the peaks together with a progressive broadening of the spectrum, particularly with the appearance of new peaks at the low relaxation-time region. Below T_g, the spectra also show similar tendencies, specifically an overall broadening, as it can be seen in Figures 3.6b and 3.6c, the latter deep below

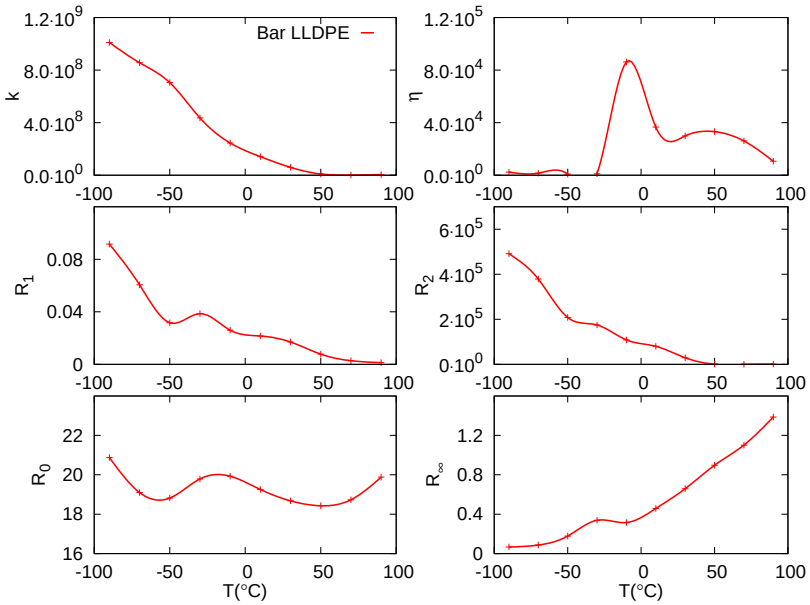

Figure 3.5: *Asymptotic coefficients k, η, R_1', R_2" and ratios $\mathcal{R}_0$ and $\mathcal{R}_\infty$ for the LLDPE bar*

T_g.

The asymptotic behaviors for this material are shown in Figures 3.7. Again, k shows a rather linear increase below T_g as the temperature decreases. In the same way, η also shows a bell shaped form with two maxima. R_1' and R_2" also follow analogous trends as in the LLDPE, provided that one uses T_g as the reference temperature. $\mathcal{R}_0$ and $\mathcal{R}_\infty$, as given in Figure 3.7, show a rather peculiar behavior. On the one hand, $\mathcal{R}_\infty$ has a peak at around 55°C, coinciding with T_g obtained from the analysis of $\tan\delta$. At the same time, however, $\mathcal{R}_0$ has a shallow valley with a minimum around the same temperature. These two features together clearly indicate that the weight of the right-hand side of spectrum is shifting to shorter relaxation-times, while the weight shifts in the opposite direction in the other side of the spectrum. Hence, this transition, which we identify as the α-transition, according to Chapter 2, could be characterized by a increase of the weight in a limited region of the central part of the relaxation-time spectrum, thus a narrowing. Hence, the interpretation of the transition as random hindrances progressively being created as the temperature is lowered cannot be straightforwardly applied to this case. It could be interpreted, however, as the vanishing of modes with long relaxation-time that progress in favor of modes with shorter relaxation-time. However, if there is a constraint for short threads of polymer, which cannot give rise

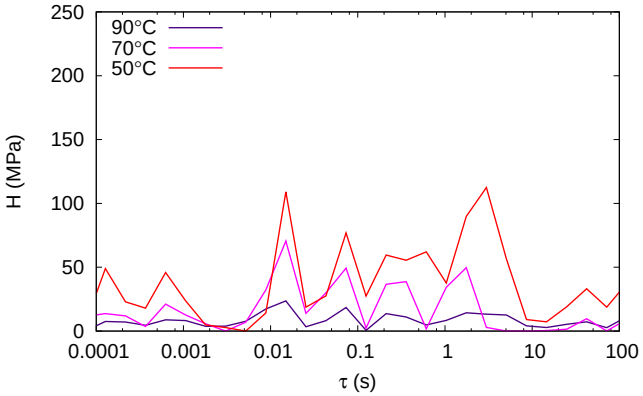

(a) *EVOH bar in the crossover region.*

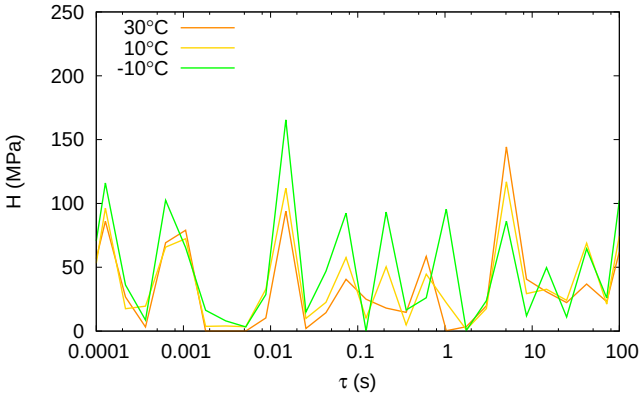

(b) *EVOH bar below the glass-transition region.*

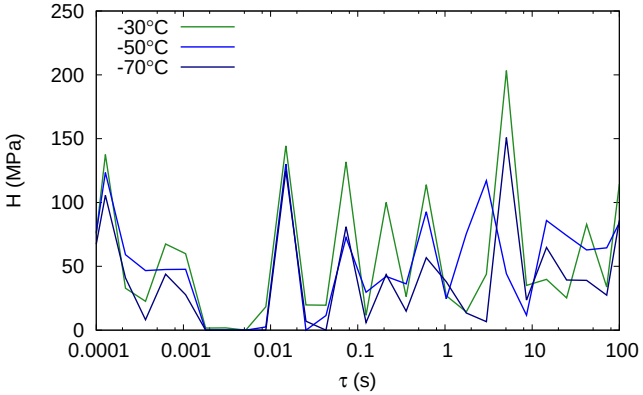

(c) *EVOH bar deep below the glass-transition region.*

Figure 3.6: *Time spectra for EVOH bar at the studied temperatures of (a): 90° C, 70° C, 50° C, (b): 30° C, 10° C, -10° C, and (c): -30° C, -50° C, -70° C.*

to shorter relaxation-times after being hindered at a given monomer, it would produce such an effect in opposite directions at both sides of τ_c. Moreover, we can identify the β-transition in the location of the second peak of $\mathcal{R}_\infty$ at a temperature of -30°C, also in agreement with the interpretation of $\tan\delta$ in Chapter 2 and also by other

authors[20]. This peak corresponds to the valley in $\mathcal{R}_0$. Thus, we assume the same interpretation as before, namely that this transition is caused by a narrowing of the spectrum. This interpretation may justify the lack of γ-transition for this material, namely, the existence of a constraint for the motion of short strands of polymer, as indicated by Cerrada *et al.*[20].

Before finishing this section, we can review the analogy between the ratios $\mathcal{R}_0$ and $\mathcal{R}_\infty$ with $\tan\delta$. Let us assume that we can approximate the latter by a combination of our ratios such that the meaning and structure is closer the possible to the own $\tan\delta$. We propose

$$\tan\delta \simeq \frac{\omega\eta + R_2"/\omega}{k + \omega^2 R_1'} \simeq \mathcal{R}_\infty \frac{1}{\omega}\left(1 + \frac{\eta\omega^2}{R_2"}\right) \tag{3.29}$$

where ω is taken as 2.5rad/s, as in the Section 2.4.1. In view of the Figures 3.5 and 3.7, R_1' is negligible in front of k and the second equality in eq.(3.29) then follows. Furthermore, the obtained values of $\eta\omega^2/R_2"$ are of order 1 in the studied temperature range. Hence, $\tan\delta$ is mostly proportional to $\mathcal{R}_\infty$ and, therefore, the distinctive features of $\tan\delta$ are also encountered in $\mathcal{R}_\infty$, at least approximately.

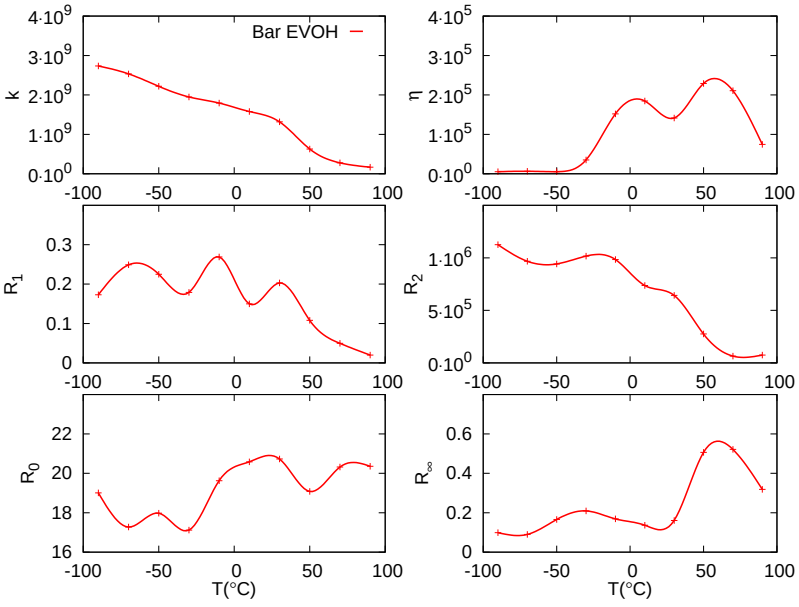

Figure 3.7: *Asymptotic coefficients k, η, R_1', $R_2"$ and ratios $\mathcal{R}_0$ and $\mathcal{R}_\infty$ for the EVOH bar*

3.4.2 Relaxation of pure LLDPE and EVOH films and LLDPE/EVOH multilayer films

The viscoelastic response of LLDPE and EVOH monomaterial films with a thickness of 25μm shows significant differences with respect to the bar counterparts, as we have seen in Chapter 2 (see Figures2.4 and 2.5). When straightforwardly applying the same treatment to find the spectra of relaxation-times, as in the previous section, we find systematic deviations between the predicted complex modulus using the GM model and the one experimentally reported, particularly for the thinnest films of 25μm, which is the only one considered this chapter. We have argued that the origin of such inability to find a good match was not due to the numerical process of finding the spectra but rather to the physical response itself. In Section 3.3.1 we have made the hypothesis that the processing conditions of fabrication of the films introduces stretching of the chains, which still remains when the solid is form. Therefore, part of the material is closer to the yield point than a material formed without external stresses and slowly cooled down. Hence, we have considered nonlinear corrections in the stress-strain relation, and used them for the fitting (see Appendix A.3 for details). Therefore, the DMA of the thin films is better predicted by using the GM model with the nonlinear correction given by eqs. (3.18) and (3.19), instead of using the linear GM model in eqs. (3.14) and (3.15). Figures 3.8a and 3.8b show the agreement obtained with the experimental data at different temperatures. The figures also show the discrepancies between the predicted and real behavior when only the linear GM model is used.

By the introduction of the nonlinear corrections, we have to fit an additional function, which describes the amplitude of the nonlinear part, i.e. $H_1(\tau)$. Together with this, one has to also determine the usual spectrum $H(\tau)$, which keeps its primitive meaning. On the other hand, the nonlinear spectrum can be used to identify the modes that are particularly stretched. Therefore, we apply the same minimization

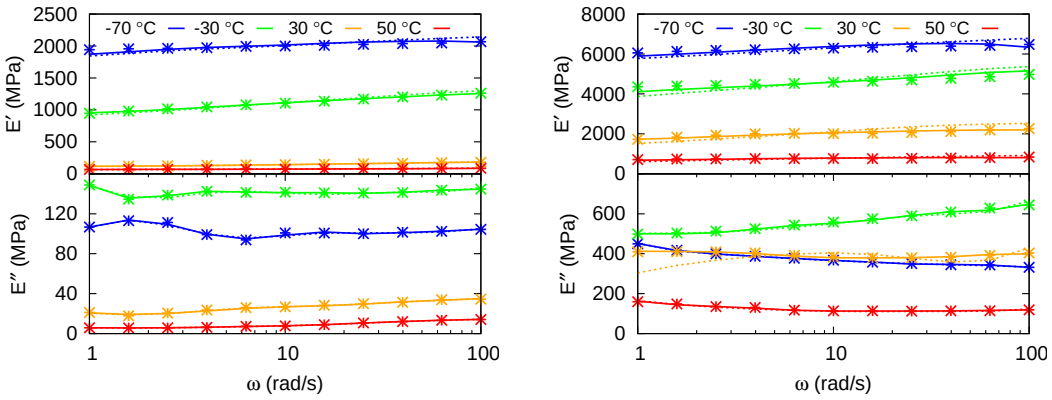

(a) *LLDPE film* **(b)** *EVOH film*

Figure 3.8: *Storage (E') and loss (E'') moduli for monomaterial film of 25 μm, solid lines are the predictions with the model plus the nonlinear corrections, dashed lines are the predictions with the linear model, and points are the experimental data at temperatures of -70° C, -30° C, 30° C and 50° C.*

procedure based on the simulated annealing with the cost function given by

$$\begin{aligned}\mathcal{E} \equiv \sum_i^N \Bigg[1 - \frac{1}{E'_{\text{exp}}(\omega_i)} \Bigg(\omega_i^2 R_1' + \sum_\alpha^M \frac{(\omega_i\tau_\alpha)^2 H(\tau_\alpha)}{1+(\omega_i\tau_\alpha)^2}\Delta\ln\tau + k \\ + \sum_\alpha^M \frac{(\omega_i\tau_\alpha)^4 H_1(\tau_\alpha)}{(1+(\omega_i\tau_\alpha)^2)^3}\Delta\ln\tau\Bigg)\Bigg] \\ + \sum_i^N \Bigg[1 - \frac{1}{E''_{\text{exp}}(\omega_i)} \Bigg(\omega_i\eta + \sum_\alpha^M \frac{(\omega_i\tau_\alpha) H(\tau_\alpha)}{1+(\omega_i\tau_\alpha)^2}\Delta\ln\tau + \frac{R_2"}{\omega_i} \\ + \sum_\alpha^M \frac{(\omega_i\tau_\alpha)^3(1-(\omega_i\tau_\alpha)^2) H_1(\tau_\alpha)}{(1+(\omega_i\tau_\alpha)^2)^3}\Delta\ln\tau\Bigg)\Bigg]\end{aligned} \tag{3.30}$$

which includes the nonlinear contributions.

For the LLDPE film, the spectra* obtained can be observed in Figure 3.9 for both, the spectra and nonlinear spectra. In the first place, Figure 3.9a gathers spectra analogous to the previous ones for bars in the rubbery plateau region. The material is rather soft in this region and the spectra have various peaks in regions similar to these of bars. While in the bars the peaks are invariably found at 0.015s, 0.07s, 0.5s and 8s, being the latter separated by a gap, here we only observe two peaks and the isolated one. At 90°C the peaks are located at 0.025s, 0.2s, and 8.6s, while the peak at 0.5s, has vanished. Decreasing the temperature causes the height of the peaks to increase but also

*We refer to "spectrum" only the weight of the linear contribution $H(\tau)$. The nonlinear correction will be referred to as "nonlinear spectrum" $H_1(\tau)$

to shift towards short relaxation-times. The spectra also notably broadens. In Figure 3.9b, one finds the temperatures that we associate to the crossover towards T_g. Here the spectra are significantly broadened and a new peak arises in the gap region existing at higher temperatures. These features were also observed when approaching T_g in the bar. Finally, in Figure 3.9c, we show the spectra sub-T_g. The spectrum is broad, and has lost any coherence when compared with the same spectra for the bar. As far as the nonlinear corrections are concerned, notice that in Figure 3.9a its contribution is negligible. This result is relevant because shows that no nonlinear contributions are required at high temperature, in regions where the GM model is expected to fully apply. However, near T_g and below, the nonlinear contribution is significant. It is interesting that the main contribution is found in the relaxation-time domain $10^{-3} < \tau < 10^{-2}$, at the border of the most sensitive region at short relaxation times. In the other side of the spectrum, only at the assumed glass-transition temperature 30°C the nonlinear contribution seems more relevant. Hence, the short relaxation-time modes are the most affected by the non-linearities above T_g. One may argue that short pieces of chain of a given characteristic relaxation-time imposed by the processing conditions are the ones stretched enough to show a nonlinear behavior. Shorter strands are unaffected by the processing because they quickly relax to its equilibrium, and longer strands do not leave the linear domain. Again, the fact that the most relevant nonlinear contribution lays at the border of the sensitive region suggests that peaks in $H_1(\tau)$ casts some doubt in the physical interpretation of the nonlinear spectra and, therefore, the conclusions drawn from its analysis should be handled with prudence.

With regard to the asymptotic coefficients, in Figure 3.10 we indicate the obtained coefficients as functions of the temperature and in comparison with the the ones of bars for the same material. The changes are significant. In particular, the coefficients are overall larger in the film than in the bar. This fact suggests that the spectra are much broader for the film, particularly at temperatures below -10°C. Moreover, the analysis of $\mathcal{R}_0$ shows a peak at around 50°C, which indicates that the left hand-side of the spectrum is shifted to short τ. However, $\mathcal{R}_\infty$ has the peak at a slightly lower temperature than 30°C. We attribute both peaks to a displacement of the α-relaxation, which has overall shifted down to a lower temperature. A second transition at around -30°C is observed as a shoulder in $\mathcal{R}_\infty$, although it is hardly noticeable in $\mathcal{R}_0$. We

attribute this peak to the glass-transition (β-transition) for the film, located at the same position as in the bar. With respect to the analysis of the $\tan\delta$, its profile is analogous to the one of $\mathcal{R}_\infty$, which is the dominating part of the spectrum for the case of the films, as we have indicated in eq. (3.29). In conclusion, films of LLDPE have in general a broadened spectra, the α-relaxation seems quite affected by the processing of the material in films, while the β-relaxation is found around the same temperature as in the bars.

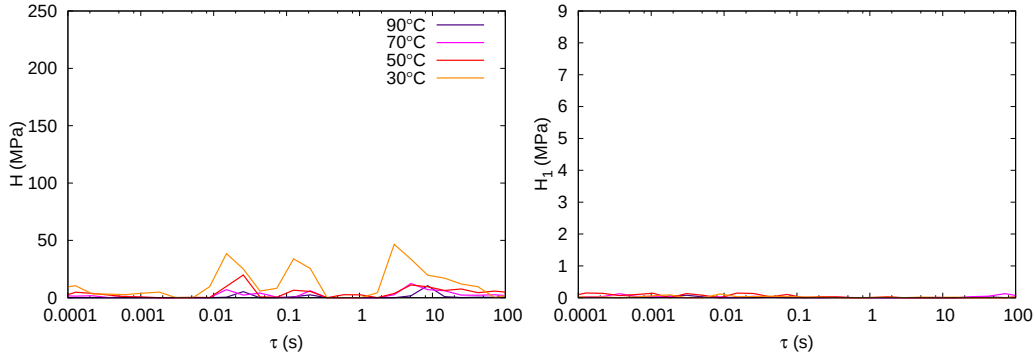

(a) *LLDPE film in the rubbery region.*

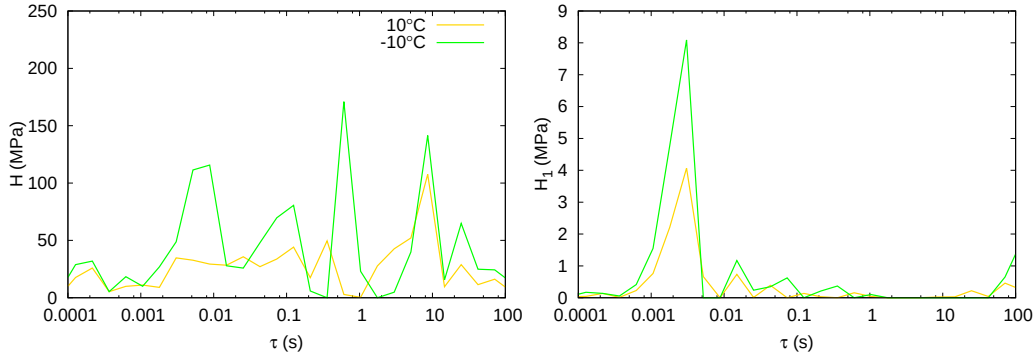

(b) *LLDPE film in the crossover region.*

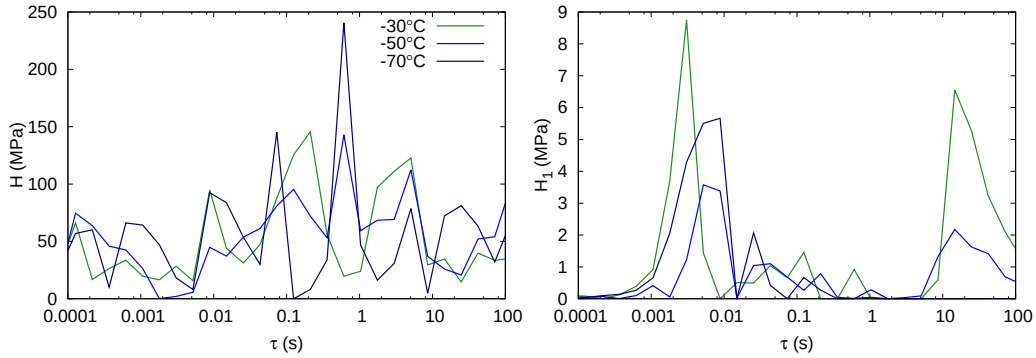

(c) *LLDPE film in the glass-transition region.*

Figure 3.9: *Time spectra for LLDPE film at the studied temperatures of (a): 90° C, 70° C, 50° C, 30° C, (b): 10° C, -10° C, and (c): -30° C, -50° C, -70° C.*

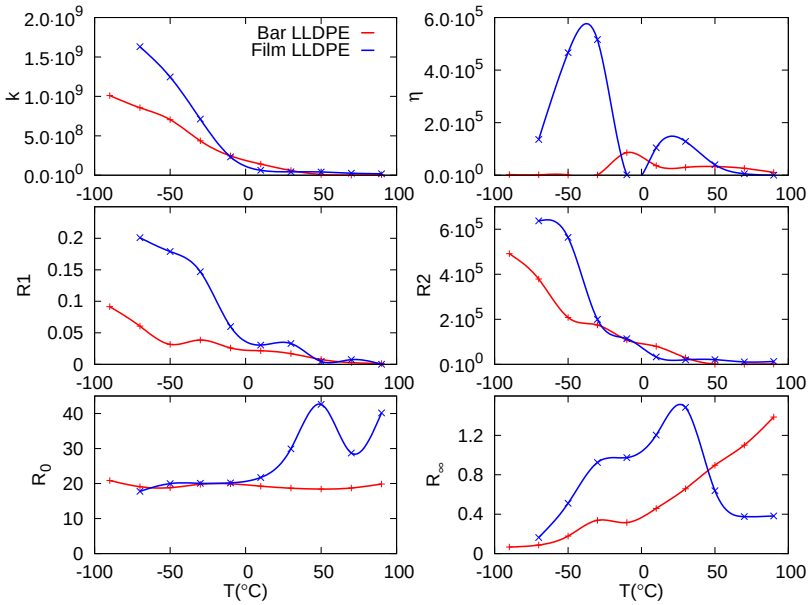

Figure 3.10: *Asymptotic coefficients k, η, R_1', R_2" and ratios $\mathcal{R}_0$ and $\mathcal{R}_\infty$ for the LLDPE film as compared to the bar*

The EVOH 25μm monomaterial film presents also a spectrum higher than the compression molded bar in agreement with our observations described in Chapter 2. The spectra are shown in Figure 3.11. In more detail, Figure 3.11a covers a range of temperatures around the glass-transition, the latter assumed to be around 30°C, in view of Figure 2.4 in Chapter 2, as well as the asymptotic ratios given in Figure 3.12, which we discuss below. In passing from 50°C to 30°C the height of the peaks is increased and new peaks arise near the edges of the spectrum, in the same way observed before for the bars of both materials (see Figures 3.4a and 3.6a). Hence, data from the $\tan\delta$ as well as this analysis confirms that the α-transition is shifted towards lower temperatures than for bars. The nonlinear spectra are significant in this region although their overall relative importance remains small as compared with the one of the linear spectrum.

In Figure 3.11b, the spectrum rises particularly in the region between 0.1s and 1s. accompanied by the increase of peaks at both sides of the spectrum, as we have already seen before in bars when one lowers the temperature below T_g. The nonlinear spectra are significantly low in this range of temperatures, precisely embracing the β-transition of the material. It is also interesting the close similitude of the two spectra at these temperatures separated 20°C. Finally, Figure 3.11c shows that the previous

peak disappears when lowering the temperature in favor of an increase of the peak at 0.015s and broad shoulders near the edges of the relaxation-time range. The nonlinear spectra shows the same features as in the case of the LLDPE, including the relevant region $0.001 - 0.01$s and the increase of the peak at the region $10 - 100$s near the glass-transition.

The most distinctive features of the spectra for both films of pure materials compared to the bar counterparts is, on the one hand, the appearance of an important peak in the region $0.1 - 1$s for both materials, which increases below T_g. On the other, the relevance of the nonlinear contributions, particularly below and around T_g. We believe that both are signatures of the processing in the obtained material. The microscopic restructuring of spherulites due to the draw ratio (cf. Chapter 2), which gives the anisotropic response in the machine and cross directions, can affect the distribution of sizes of the threats in the amorphous fraction. The draw change the crystallite orientation from an isotropic distribution, as in the spherulites existing in the bar, to a distribution that favors its orientation orthogonal to the flow direction. This ordering should favor the growth of threads with given dimensions and properties, as it would be the case for bridges between these crystallites. Moreover, the concentration of the nonlinear spectrum in a region $0.001 - 0.01$ below T_g also is an indication that the modes in this range are strongly affected by the processing. These modes can be regarded as being quenched at exit of the dye while they have been strongly stretched by the extensional flow of the melt prior to its exit through the dye.

To end our analysis of the pure materials, in Figure 3.12 the asymptotic coefficients for the EVOH film are depicted. The overall behavior is similar to that of the LLDPE film (see Figure 3.10), taking again the glass-transition temperature as the reference. The most distinctive feature of the EVOH film, however, is that both α (glass-transition temperature) and β-transitions are shifted to lower temperatures with respect to the bars. In LLDPE film, however, only the α-transition seems to shift to lower temperatures while the β-transition (glass-transition) remains essentially unchanged.

The analysis of the multilayer films is attempted through the comparison between the spectra obtained directly from the experimental data on the storage and loss moduli (see Figure 2.8) with the predicted behavior from the superposition of the spectra of the individual pure films. The application of eq. (2.1) straightforwardly implies the

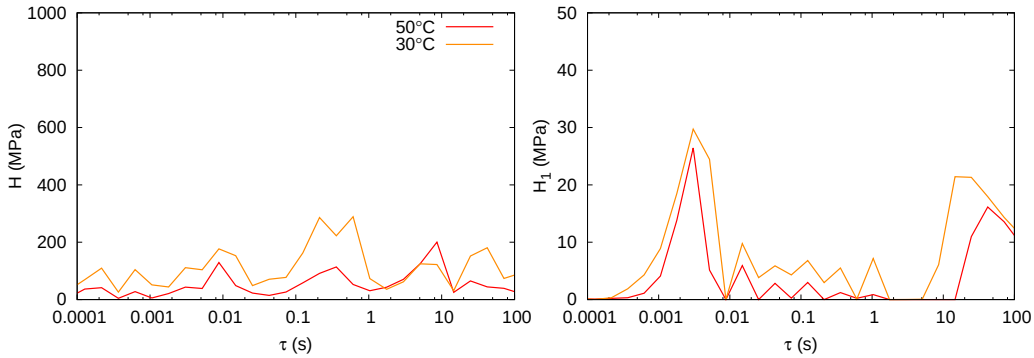

(a) *EVOH film in the glass-transition region.*

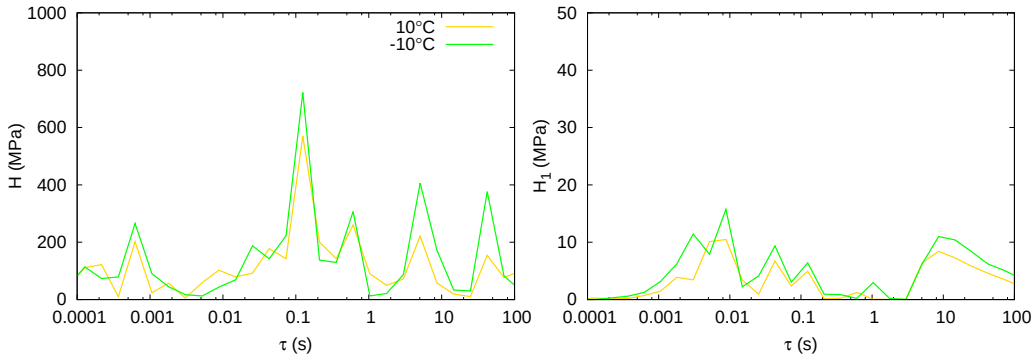

(b) *EVOH film below the glass-transition region.*

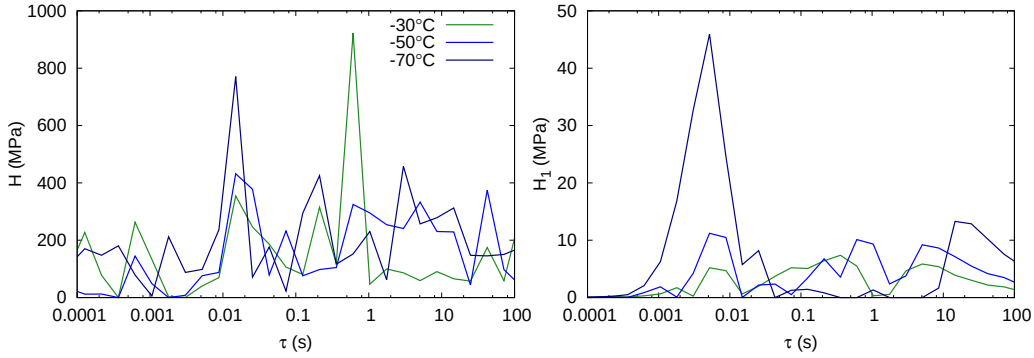

(c) *EVOH film deep below the glass-transition region.*

Figure 3.11: *Time spectra for EVOH film at the studied temperatures of (a): 50° C, 30° C, (b): 10° C, -10° C, and (c): -30° C, -50° C, -70° C. We can only report on temperatures below* T_g

superposition of the linear but also nonlinear spectra, due to the fact that we assume superposition of the stresses, regardless whether their relationship with the deformation is linear or not. In addition, the deformations are assumed to be the same for all the layers. Hence, the spectra and asymptotic coefficients obtained from the fitting of the experimental data should be compared to the direct superposition of the spectra and the nonlinear spectra, separately, of the pure components. Due to the good accuracy of the predictions of the storage and loss moduli of the pure components using the GM

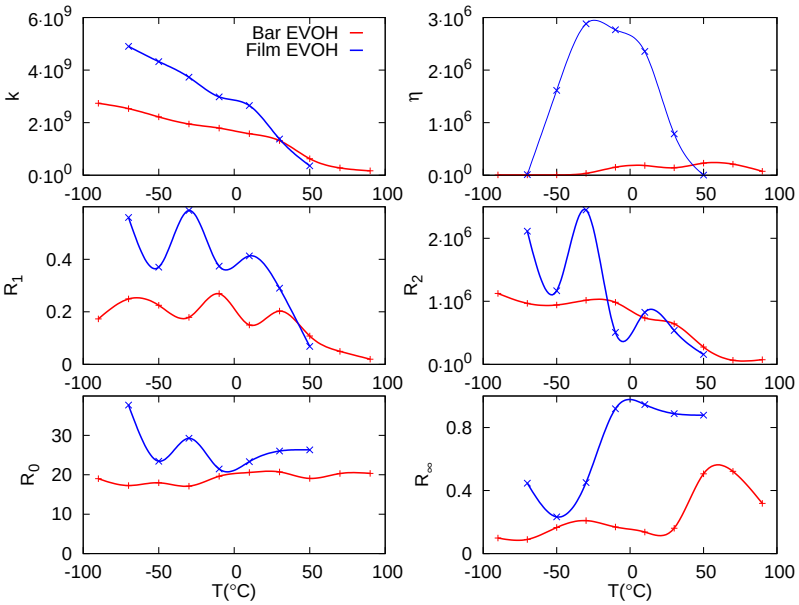

Figure 3.12: *Asymptotic coefficients k, η, R_1', R_2" and ratios $\mathcal{R}_0$ and $\mathcal{R}_\infty$ for the EVOH film as compared to the bar*

model with nonlinear corrections (see Figures 3.8a and 3.8b), the direct superposition of the spectra yields again the predictions given in Figure 2.8. In Figures 3.13 we show the comparison between the predicted spectra and the fitted ones for the multilayer film of 10% of EVOH. Moreover, in Figure 3.14, the corresponding predicted and calculated asymptotic coefficients are also depicted. For this particular sample a good fit of the moduli is achieved. However, the differences of the spectra are important, although we identify reminiscences of the obtained spectra in the predicted by superposition of that of pure films. For example, for -30°C the overall shape and location of the peaks, as well as the nonlinear contribution are rather coincident. However, the other three show discrepancies which could be related to genuine effects of the confinement, since the individual EVOH layers are about 160nm, cf. Table 2.3. Nevertheless, interfacial effects between the two polymer species could also lead to deviations from the mixing rule eq. (2.1). The general trend is that at the higher temperatures studied the region $1-10$s seems the more affected by the presence of a new peak in the calculation of the spectrum directly from experimental data. The presence of this peak also corresponds with the decrease of the nonlinear component in the region $10-100$s. For 50°C the profile of the direct distribution is overall higher than the prediction but also narrower. In view of Figure 2.8, is precisely in the temperature range between $30°-50$°C where

the discrepancy is more noticeable in the $\tan\delta$. As far as the asymptotic coefficients are concerned, the discrepancies are more noticeable, although we cannot distinctively locate them in the temperature range just mentioned. Moreover, the tendencies and the overall size of these coefficients are in agreement. Obtaining relevant information about the transitions seems not appropriate, in view of the composite nature of the material and the rather different peaks and valleys shown by the curves.

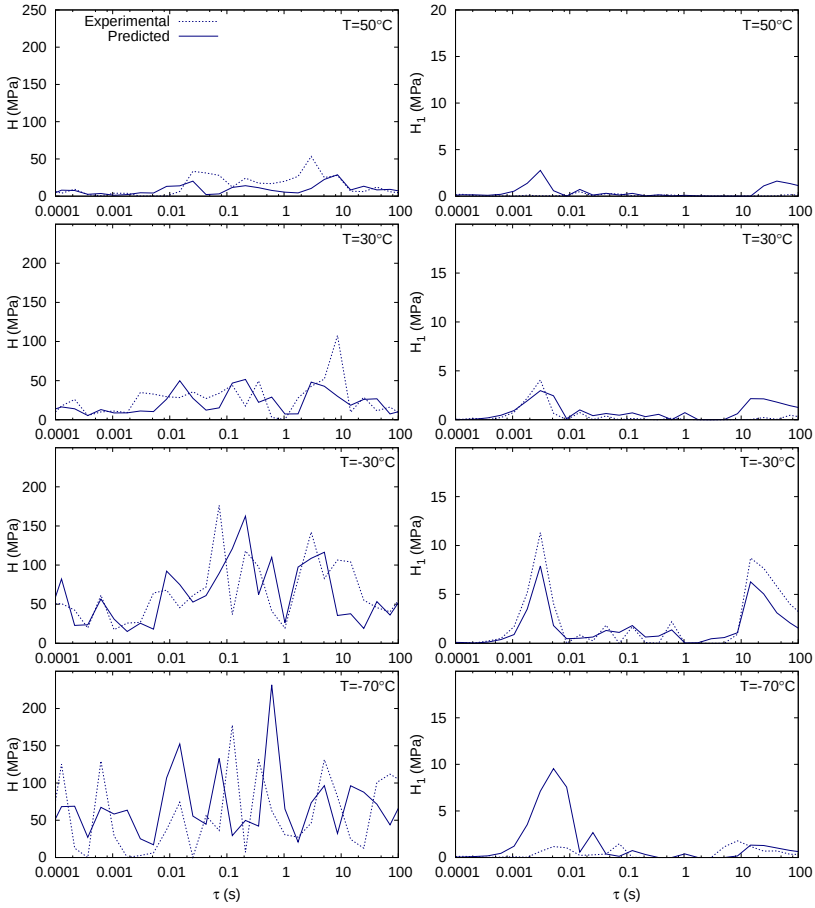

Figure 3.13: *Time spectra for 90/10 LLDPE/EVOH 25μm film. Dashed lines represent the spectra calculated directly from the experimental data of the sandwich while solid lines represent the spectra predicted using eq.*(2.1)

3.5 Conclusions

In this chapter we have analyzed relaxation-time distribution of different samples of pure LLDPE and EVOH in compression molded bars and films of 25μm as well as for multilayer sandwiches of the same materials. To obtain the spectra of relaxation-

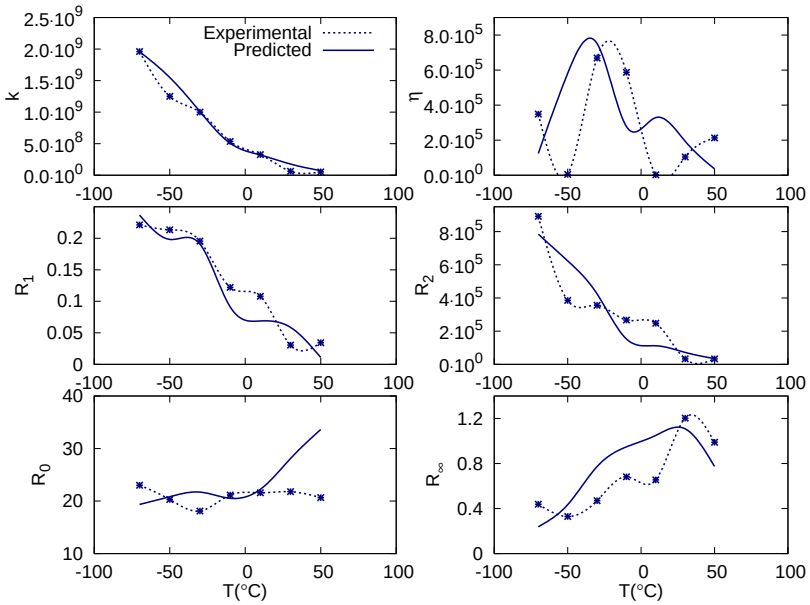

Figure 3.14: *Asymptotic coefficients k, η, R_1', R_2" and ratios $\mathcal{R}_0$ and $\mathcal{R}_\infty$ for the 90/10 LLDPE/EVOH 25μm film. Dashed lines represent the coefficients calculated directly from the experimental data of the sandwich while solid lines represent the spectra predicted using eq.*(2.1)

times we have used the Generalized Maxwell (GM) model extensively described in the literature[40,137]. From a numerical point of view, we have developed a simulated annealing that preserves the positiveness of the spectra and allows for the location of peaks in a range larger than the one comprised between $1/\omega_{max} < \tau < 1/\omega_{min}$, limited by the lost of sensitivity of the method in the tails. The detailed spectrum in this region of the tails has been replaced by four asymptotic coefficients which gather information of some moments of the distribution in these distant tails. In the analysis of the thin films of 25μm the GM model is unable to describe the experimental data of the storage and loss moduli. This inability is not of numerical nature but a characteristic of the response of the material itself. We have then proposed nonlinear corrections to the GM model based on the Eyring theory for the mechanical response of polymers near the yield. With this procedure we obtain a very good fit of the moduli in the range of frequency experimentally studied.

The spectra as well as the asymptotic coefficients yield relevant information which can be related to the microscopic structure of the material, which can be modified either by the processing conditions, interfacial properties between layers, or by the confinement into sub-micrometric layers in the sandwiches. Unfortunately the lack of

additional microscopic information impairs an analysis of the mechanical response in terms of the microscopic details. According to Chapter 2, the processing conditions have a mechanical effect on the properties of the films as compared to molded bars. The comparative study between the spectra of films and bars of pure components has revealed shifts of some transitions and also a distinctive peak in the region between $0.1 - 1$s, which we can qualitatively relate to the reorientation of the crystallites by the effect of the drawing during solidification, which give rise to modes non-existing in both polymers. Moreover, the nonlinear contribution to the spectra is only relevant for films and at temperatures close and below the glass-transition, which supports the original idea that the material does not respond linearly to the deformation even at the small deformation of our experiments.

Finally, in view of eq.(2.1), along the lines of Chapter 2, we can anticipate the spectra for the sandwiches by a weighted superposition of the spectra of films of the pure components obtained with the same draw ratio as the sandwich. Then, we have compared with the spectra obtained from the direct fitting of the experimental data for the moduli of the sandwiches. The comparison reveals interesting features that appear in both, although the roughness of the profiles make the identification quite complicated. In general, we can conclude, as in Chapter 2, that a substantial part of the mechanical response of the sandwiches is the reflect of the mechanical response of the individual layers. However, the discrepancies also put on the table the deviations of the response of the sandwiches with respect to the pure superposition, which we have attributed to the effects of the confinement and to the appearance of modes in the region $1 - 10$s in the spectrum.

The most of the interpretations done in this chapter have to be taken as purely speculative by all sources of uncertainties either experimental, theoretical or numerical, and the evident lack of complementary microscopic information. However, analysis of this type for semicrystalline materials are very rare in the literature and therefore we believe that the study that we have carried out can be useful in approaching a better understanding of this complex materials of such a great economical importance.

Chapter 4

Cell Dynamics Simulation

Synopsis

In this chapter we will describe the mesoscale simulation technique which we used to study diblock-copolymers under external influences[24]*. Using Cell dynamics Simulation we studied the behavior of diblock-copolymer thin films on pattern surfaces. This technique allows us to analyze events which happens on a time scale which is too long to be described by classical molecular dynamics. Using 3-Dimensional Cell Dynamics Simulation we demonstrate that long-range order can be obtained, which depends on the commensurability of the structure with both the band periodicity and slit thickness. The comparison of the simulation results with experimental data [Park, SM.et al, Macromolecules* **2008***, 41, 9124] shows an almost quantitative agreement between both, if the characteristic distance between mesophases, d, is used as the only scale. Furthermore, we show that the proper selection of the band periodicity and, consequently, of the film thickness, permits the system to switch from a hexagonal packing to a body-centered orthohedron. Therefore, we show a way to control the formation of long-range ordered structures of different types in this kind of systems.*

4.1 Introduction

Supramolecular structures of nanometric size are of great interest due to potential applications in nanotechnology, which range from nanopatterned surfaces, nanocrystals with exotic optoelectronic properties, to functional foods and pharmacological products[36,47,94]. The main technological problem is to achieve the control and reliability of the final product when traditional manufacturing processes cannot be down-scaled to the nanometric size. Hence, physical systems that spontaneously form supramolecular assemblies under appropriate conditions are so important, as far as they can be externally controlled to produce the desired target structure[86]. Block copolymers (BCP) are one of these valuable materials. because of their ability to self-assemble into different nanostructures[48,64,95,117,128].

In this chapter we address the analysis of the problem of how external effects, like the presence of a chemical mask on a surface, affects the two- and three-dimensional structure of thin films of sphere forming BCP. This question was experimentally analyzed by Park *et. al.*[96], showing some interesting aspects of the self-organization of BCP in the presence of a structured wall. Here we apply Cell Dynamics Simulation (CDS) to widen the range of conditions experimentally analyzed and, more important, to infer the relationship between the aforementioned external constraints and the particular features of the structure obtained. We find that, inside the range of naturally produced arrangement of the polymer blocks in microphases, the surface pattern allows to selectively produce different types of structures.

BCP consist of blocks of chemically different monomers covalently bond. In particular, the simpler systems are (A-B) diblock copolymers. If monomers A and B are highly incompatible, the system can spontaneously segregate into two distinct nanodomains (microphase separation). The size of such nanodomains is on the range between 10 and 100 nm. Depending on the nature of the monomers, such as their degree of polymerization, interaction between the components, and the relative size of each block, these microphases can be either lamellae, cylinders, or spheres, although other more exotic morphologies, like the gyroid phase, can be observed[8,45,83].

Morphologies not accessible in the bulk can exist under confinement due to the additional constraints on the system imposed by the bounding surfaces[41]. Constraints are, for instance, spatial frustration, preferential attraction of one of the blocks to the walls

with respect to the other, and structures build at the interfaces, among others. The confinement geometry can hinder the system in one, two or three-dimensions [120,135], as in confinement between two parallel surfaces or in thin films, in cylindrical pores [30,121,136,140], or into spherically-shaped pores [4].

Centering our attention on thin films, a variety of domain architectures can be obtained influenced by the boundary conditions at both, the top and bottom interfaces [52,61,66,68]. BCP can serve to pattern large areas of regular arrays of nanostructures for nanolitography, for the synthesis of highly-ordered dispersions of inorganic particles, they can be used for semiconductors, magnetic storage media, photonic crystals, and nanostructured membrane applications, among many others [48,64,95,117,128]. Almost invariably, microdomains with a long-range order are required for these applications. However, in real systems long-range order is hindered by a rather degenerate free-energy landscape as well as by the slow diffusion of the polymers in the process of domain reorganization after quench [118,147]. For example, refs. [3,69] show that perfectly ordered arrays of domains in thin films of BCP are not expected even at equilibrium, since in a nearly 2D system the translational order is at best quasi-long-range, due to a finite concentration of thermally activated defects permanently present. Hexatic phases with no long-range translational order appear at temperatures close to the melting of the structure into a disordered phase of domains [118].

Various techniques have been proposed to tailor the arrangements of nanoscale domains, or to accelerate the slow dynamics of the ordering near equilibrium, to produce the aforementioned well controlled long-range order. One can find, for instance, the modifications in the supporting substrates, such as topographically or chemically patterning, the application of external fields, like shear or electrical fields, etc. [36,63]. In more detail, for symmetric BCP (lamellae forming) the commensurability between the periodicity of the pattern substrate and the natural length scales of the BCP was found to play an indispensable role to obtain a particular lamellar morphology in thin films [110]. Subsequently, regular quasi defect-free linear conformations in the nanoscale could be fabricated [34,65,144]. As far as the asymmetric block copolymers are concerned, dense arrays of nanocylinders with controlled orientation and enhanced uniformity are obtained using hexagonal arrays of dots chemically patterned on the supporting-substrate [58,62,112,127]. Square arrays of vertical cylinders, instead of the hexagonal array typically found in

bulk, can also be produced using a chemically patterned surface with a square array of spots, instead[97].

With regard to the sphere-forming BCP in thin films, long-range order structures are achieved on topographically modified surfaces forming wells and mesas, which yield crystal-like structures[116]. On the other hand, when assembling spheres in V-shaped grooves, well-ordered domains are obtained with a face-centered cube close-packing symmetry, with the (111)-planes of the array parallel to the groove walls[26]. Additionally, hexagonally arranged posts or semi-dense hole patterns[14,141] can be used to form arrays of spherical domains whose periodicity is higher than the one of the substrate, in a phenomenon referred to as *density multiplication*. The orientation and periodicity of the resulting array of spherical microdomains is found to be governed by the commensurability between the block copolymer period and the template periodicity. Alternatively, well-aligned spherical domains, build using a chemically striped patterned surface, also with a periodicity commensurate with the BCP natural periodicity, are reported in ref. [96]. Furthermore, the film thickness is also a key parameter to draw long-range order of spherical BCP domains, as can be inferred from the transitions between the typical 3D BCC arrangement of spheres found in the bulk and the 2D hexagonal arrangement encountered under confinement[126,147].

Recent efforts have been addressed to increase the accuracy of the control over the shapes and dimensions of the equilibrium morphologies[139,142], to improve defect-free long-range order arrangements, aiming at obtaining high density multiplication, together with pattern quality rectification, fabrication of new complex structures never found in in the bulk[23,77,78,106,146]. Müller et. al.[86] recently introduced a new procedure to drive the self-assembly towards desired geometries through a process-directed mechanism in which the kinetics of structure formation is externally led to achieve the sought long-life metastable state.

From the theoretical viewpoint, two main approaches have been widely used to describe the microphase separation of BCP. On the one hand, the self consistent field theory (SCFT) deals with coarse-grained models of the BCP, in which bonded interactions are described as flexible Gaussian chains, while non-bonded interactions are introduced through the local densities, which are the mean fields. Many calculations in 2- and 3D for relatively small systems have been carried out aiming at understand-

ing the formation of BCP structures[15,32,53,82,132]. Particularlly, simulations of confined systems, with chemically activated or topographically modified substrates, were performed in refs. [62, 71, 98, 143, 145]. Although the method permits to keep some molecular details of the chain, SCFT is still a computationally expensive method when large systems are to be studied. Particularly, the dynamics processes involving domain restructuration are very long as compared with the molecular scales of chain reorganization, whose specific consideration is required in a dynamic implementation of the SCFT described so far.

On the other hand, Ohta and Kawasaki[90], from a molecular description of the BCP, developed a free-energy functional corresponding directly to the monomer concentration fields, with no explicit reference to microscopic details, except in the definition of the coefficients. The final form resembles a Grinzburg-Landau functional, with a long-range contribution that accounts for the chain connectivity. From the free-energy functional a diffusive dynamics can be constructed in the spirit of the Cahn-Hilliard-Cook equation[91] for systems with a conserved order parameter. This coarse-grained level of description allows to observe the microphase separation phenomena in systems whose dimensions are comparable with the ones experimentally addressed. This method is customarily referred to as Cell Dynamics Simulation[46,101]. In the framework of this method the dynamics and structure of BCP on chemically patterned surfaces have also been studied for cylinder and lamellae forming BCP[21,22,37,38,75,76].

However, the theoretical analysis of the self-assembly of spheres on a chemical patterned surface has not been addressed yet. We explore the usefulness of a very simple stripped pattern in guiding the final structure of asymmetric BCP forming spheres in contrast with more sophisticated designs like arrays of spots or other graphoepitaxial techniques. The numerical approach allows us to infer the effect of the commensurability between the pattern periodicity, as well as the slit thickness, and the natural spacing of the formed structures. The analysis permits us to identify the optimal conditions for defect-free assembly of several layers of spheres, with different unit cell. We think that the study reveals some keys for a better structure control in the manufacturing at the nanoscale.

4.2 Fundamentals

4.2.1 The Cell Dynamics Simulation

The Cell Dynamics Simulation (CDS) method was introduced to model interface dynamics in phase-separating systems. Theoretically, CDS is based on the Cahn-Hilliard-Cook (CHC) equation, which is used as the governing differential equation for the time evolution of a conserved order parameter $\Psi(\vec{r},t)$ [46,89]. The CHC equation can be derived from the balance equation for the order parameter, eq. (4.1), together with the linear relationship between the order parameter flux $\vec{J}(\vec{r},t)$ and the local chemical potential, eq. (4.2) [44]. That is,

$$\frac{\partial \Psi(\vec{r},t)}{\partial t} = -\nabla \cdot \vec{J}(\vec{r},t) \tag{4.1}$$

$$\vec{J}(\vec{r},t) = -M\nabla\mu(\vec{r},t) \tag{4.2}$$

The chemical potential can be expressed as a functional derivative of a free-energy functional

$$\mu(\vec{r},t) = \frac{\delta F[\Psi]}{\delta \Psi(\vec{r},t)} \tag{4.3}$$

Hence, the CHC equation is obtained as

$$\frac{\partial \Psi}{\partial t} = M\nabla^2 \left(\frac{\delta F[\Psi]}{\delta \Psi} \right) \tag{4.4}$$

where M is a phenomenological mobility constant taken as $M = 1$. This choice sets the timescale for the diffusive processes (the dimensionless time is tM/a_0^2, where the lattice cell spacing a_0 is taken as the unit of length). The dynamics of eq. (4.4) is consistent with the mean-field theory and would correspond to a situation with negligible thermal fluctuations, namely, BCP of large molecular weight [42,105].

In CDS, the commonly used expression for the order parameter $\Psi(\vec{r},t)$ in terms of the A and B comonomer volume fractions, ϕ_A and ϕ_B, respectively, is [46,101]

$$\Psi(\vec{r},t) = \phi_A(\vec{r},t) - \phi_B(\vec{r},t) + (1-2f), \tag{4.5}$$

where $f = N_A/(N_A + N_B)$ stands for the number fraction of A monomers per chain. The order parameter is then the difference between the local volume fraction of both

monomers, plus a constant such that the integral of $\Psi(\vec{r},t)$ over the entire volume of the system is 0 by construction. For symmetric copolymers, $f = 1/2$, the constant vanishes.

The necessary condition of equilibrium is given by

$$\frac{\delta F[\Psi]}{\delta \Psi}\Big)_{eq} = 0 \tag{4.6}$$

with a positive second functional derivative. Eq. (4.6) is not a sufficient condition because the system can be trapped into local metastable minima during its time-evolution according to eq. (4.4).

The free-energy $F[\Psi]$ (in reduced units such that $kT = 1$) used along this work is given by[7,90]

$$\begin{aligned} F[\Psi(\vec{r})] = \int d\vec{r} \Bigg\{ \left[H(\Psi) + \frac{D}{2}|\nabla\Psi|^2 \right] + \frac{B}{2} \int d\vec{r}\,' G(\vec{r}-\vec{r}\,')\Psi(\vec{r})\Psi(\vec{r}\,') \\ - \sum_i s_i(\vec{r})\Psi(\vec{r}) \Bigg\} \end{aligned} \tag{4.7}$$

The first term, $H(\Psi)$, contains the local contributions to the free-energy, expressed as an expansion in terms of the order parameter, in the spirit of the Ginzburg-Landau theory[74,90]. The expression used along this work is given by[46,108].

$$H(\Psi) = \left[-\frac{\tau}{2} + \frac{A}{2}(1-2f)^2 \right] \Psi^2 + \frac{v}{3}(1-2f)\Psi^3 + \frac{u}{4}\Psi^4 \tag{4.8}$$

Here A, v, and u are phenomenological constants derived by Leibler[74] using the random phase approximation. τ is proportional to the Flory-Huggins parameter χ, which inversely depends on the temperature T. According to Ohta and Kawasaki[74,90], the parameter

$$\tau' \equiv -\tau + A(1-2f)^2 \tag{4.9}$$

can be expressed in terms of physical parameters as

$$\tau' = -\frac{1}{2N}\left(N\chi - \frac{\tilde{s}(f)}{4f^2(1-f)^2} \right) \tag{4.10}$$

where $\tilde{s}(f)$ is an empirical fitting function whose value is of order of 1[90].

Together with the terms contained in $H(\Psi)$, one also has a surface term, $D|\nabla\Psi|^2/2$, to account for the free-energy necessary to create an interface between A and B, which plays a very important role in this system due to the large area of contact between microphases. The coefficient D is a positive constant that scales as $D \sim b^2$, where b is the Kuhn segment length of the polymer. The expression for D reads

$$D = \frac{b^2}{48f(1-f)} \tag{4.11}$$

Finally, chain connectivity introduces a long-range term of the form $\frac{B}{2}\int d\vec{r}\,' G(\vec{r} - \vec{r}\,')\Psi(\vec{r})\Psi(\vec{r}\,')$. The coefficient B scales as N^{-2}, and reads[46,74,90]

$$B = \frac{9}{(2Nbf(1-f))^2} \tag{4.12}$$

where N is the total degree of polymerization. This term in the free-energy carries a chain-length dependence. Notice that the Green function $G(\vec{r} - \vec{r}\,')$ satisfies $\nabla^2 G(\vec{r} - \vec{r}\,') = -\delta(\vec{r} - \vec{r}\,')$.[46,74,90,108] It should be mentioned here that this particular form of the Green function was derived for bulk systems. The presence of hard walls is expected to influence the functional form of the Green function due to the reduction of the number of chain conformations when polymers are near an impenetrable surface, as follows from its derivation[74,90]. However, this effect is small and qualitatively does not introduce significant deviations in the predictions, as can be seen from the comparison with experimental data of related systems later on. For convenience, we define the dimensionless parameters $\tilde{D} = D/a_0^2$ and $\tilde{B} = Ba_0^2$ to be used in the simulations. For simplicity, we write D and B instead of $\tilde{D}$ and $\tilde{B}$ from now on, since no confusion can occur. The parameters in eq. (4.7)-(4.9) will be considered as phenomenological constants.

The last term in eq. (4.7), where i denotes either A or B component, takes into account the interaction of the block copolymer with the confining hard walls. In the studied case, the walls are surfaces presenting a chemically activated mask. Hence, the $s_i(x, y, z)$ term is defined as[39,81]

$$s_i(x, y, z) = h_i\ \phi_i\ \tilde{\delta}_x\ \delta_{z,1} \tag{4.13}$$

$$\tilde{\delta}_x \equiv \begin{cases} -1, & 2nw \leq x < (2n+1)w \\ 1, & (2n+1)w \leq x < 2(n+1)w \end{cases} \tag{4.14}$$

where n is an integer and h_i is the strength of the interaction between the walls and the respective i segments. Moreover, w is the width of an individual stripe and δ_{ab} is the Kronecker delta. Notice that ϕ_i can be expressed in terms of the order parameter Ψ, i.e. $\phi_A = f + \Psi/2$ and $\phi_B = 1 - f - \Psi/2$. The pattern on the lower surface thus corresponds to long stripes of width w parallel to the y-direction.

4.2.2 The Numerical Cell Dynamics Simulation

The numerical scheme to implement the dynamic model described so far is based on the definition of the fields in a cubic lattice, together with an appropriate discretization of the Laplacian in eq. (4.4) [109]. We propose

$$\Psi(i,j,k\,;t+1) = \Psi(i,j,k\,;t) - \{\langle\langle \Gamma(i,j,k\,;t)\rangle\rangle - \Gamma(i,j,k\,;t) + B\Psi(i,j,k\,;t)\} \tag{4.15}$$

Here (i,j,k) stands for the set of indexes of a given grid point on the lattice, and $\langle\langle\Gamma\rangle\rangle - \Gamma$ stands for a discrete Laplacian defined by [46,122]

$$\langle\langle\Psi\rangle\rangle = \frac{6}{80}\sum_{NN}\Psi + \frac{3}{80}\sum_{NNN}\Psi + \frac{1}{80}\sum_{NNNN}\Psi \tag{4.16}$$

where NN denotes nearest neighbors, NNN next-nearest neighbors, and $NNNN$ next-next-nearest neighbors of a point r. This choice of the Laplacian is made to preserve as much as possible the original isotropy of the system in continuous space.

The function Γ is defined as

$$\Gamma(i,j,k\,;t) = g(\Psi(i,j,k\,;t)) - \Psi(i,j,k\,;t) + D[\langle\langle\Psi(i,j,k\,;t)\rangle\rangle - \Psi(i,j,k\,;t)] - s_i(z) \tag{4.17}$$

Finally, the so-called map function $g(\Psi(i,j,k\,;t))$ is directly related to the functional derivative of H given in eq. (4.8). g ultimately contains the tendency of the order parameter to the phase separation. For our particular system g reads, [7,107]

$$g(\Psi(i,j,k\,;t)) = [1 + \tau - A(1-2f)^2]\Psi - v(1-2f)\Psi^2 - u\Psi^3 \tag{4.18}$$

4.2.3 The Free Energy Functional in the Lattice

The pass from the continuous space to the lattice introduces necessary prescriptions for the evaluation of the Laplacian and the non-local contribution appearing in the definition of the free-energy functional, defined in continuous space in eq. (4.7). As a consequence, we cannot construct the corresponding free-energy functional model on the lattice by the direct discretization of the right hand side of eq. (4.7), expecting that this model will have the required properties for the discrete field, namely, that the dynamics implemented in eq. (4.15) progresses monotonously lowering the value of the free-energy functional to its minimum at equilibrium. The discrete counterpart of the functional derivative of the free-energy functional sought should be compatible with the second term on the right hand side of eq. (4.15), after the discrete Laplacian is taken, according to eqs. (4.3) and (4.4).

Let $F[\Psi(i,j,k)]$ be the free-energy functional of the field $\Psi(i,j,k)$ defined on the lattice. The functional differentiation in the lattice is simply the partial derivative with respect to the field at every grid point, so that the chemical potential in a given point (i,j,k) reads

$$\mu(i,j,k) = \frac{\partial F}{\partial \Psi(i,j,k)} \tag{4.19}$$

Accordingly, the dynamic equation eq. (4.15) can be written as

$$\Psi(i,j,k\,;t+1) = \Psi(i,j,k\,;t) + \langle\langle \mu(i,j,k)\rangle\rangle - \mu(i,j,k) \tag{4.20}$$

Therefore, the key point is to provide a discrete free-energy whose functional derivative on the lattice, eq. (4.19), gives a chemical potential field such that eq. (4.20) is identical to eq. (4.15). We thus propose

$$F[\Psi(i,j,k)] = \sum_{i,j,k} \left(H[\Psi] - \frac{D}{2}\Psi\left[\langle\langle\Psi\rangle\rangle - \Psi\right] + \frac{B}{2}\mu^{(lr)}\Psi + s_A\left[\frac{\Psi}{2} + f\right]\right) \tag{4.21}$$

where both Ψ and $\mu^{(lr)}$ on the right hand side of eq. (4.21) are calculated at the grid point (i,j,k). Furthermore, $\mu^{(lr)}$ is the solution of the algebraic set of equations defined from the relation

$$\langle\langle \mu^{(lr)}(i,j,k)\rangle\rangle - \mu^{(lr)}(i,j,k) = -\Psi_{i,j,k} \tag{4.22}$$

which corresponds to the discrete Laplacian of the long-range term equated to the thermodynamic force used on eq. (4.15), according to eq. (4.20).

Therefore, when the free-energy of a given state is required during the calculation, from the actual value of the field $\Psi(i,j,k)$ we iteratively solve the set of equations (4.22) and substitute the field as well as the resulting $\mu^{(lr)}$ in eq. (4.21) to obtain the numerical value of the functional for a given $\Psi(i,j,k)$.

4.3 Results and Discussion

4.3.1 Model System

In this study we consider a sphere-forming diblock copolymer (BCP) in liquid phase without added solvent, thus corresponding to a polymer melt. The CDS parameters are $f = 0.4$, $u = 0.38$, $v = 2.3$, $B = 0.01$, $D = 0.5$, $A = 1.5$, $\tau = 0.2$, which are known to produce spherical domains[100,102]. The morphological characteristics of the spherical domains are: the spacing between spheres $d \simeq 11$ and their average diameter $\varnothing \simeq 7.8$ in units of lattice spacings a_0 (see Figure 4.1). These parameters are taken from ref.[100], and correspond to the morphology of a monolayer of spheres formed in a slit with homogeneous surfaces selectively attracting the A-block.

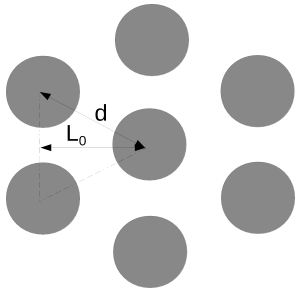

Figure 4.1: *Sphere-froming BCP in a 2D hexagonal distribution with the characteristic dimensions. The natural lateral period for the hexagonal forming system given in ref. [100] is $L_0 \simeq 9.5$ ($L_0 = \sqrt{3}/2d$)*

The system studied along this work consists of the BCP confined in a slit of hard walls. The lower surface is decorated with a mask of chemically active stripes with different affinity to the blocks of the BCP, i.e. different values of s_i in eq. (4.7). In particular, we have chosen $h_A = 0.1$ and $h_B = -0.1$, according to eqs (4.13) and (4.14). The upper surface of the slit is chemically neutral ($s_i = 0$ for all blocks i). These solid walls are located at the position $z = 1$ for the bottom surface and $z = L_z$

for the top surface, as shown in Figure 4.2-a. The pattern on the bottom surface corresponds to a set of alternating parallel stripes along the y-direction, whose width is $w = L_S/2$, as depicted in Figure 4.2-b. Thus, the distance between equal stripes (or band periodicity) is L_S. We have verified that the morphology of the patterns observed is rather insensitive to the attraction energy h if it is kept within the range from 0.1 to 0.4. Hence, for convenience, we have chosen $h = 0.1$ in all the simulations. Periodic boundary conditions (PBC) are set for the x and y-directions. The boundary condition of zero flux of Ψ at the hard surfaces implies that the gradient of the chemical potential eq. (4.3) vanishes at the interfaces[81]. Numerically, such a condition is fulfilled by extending the field inside the wall and demanding $\Psi(x, y, z = 0) = \Psi(x, y, z = 1)$ and $\Psi(x, y, z = L_z + 1) = \Psi(x, y, z = L_z)$, where $z = 0$ and $z = L_z + 1$ are the coordinates of the extended layers[39].

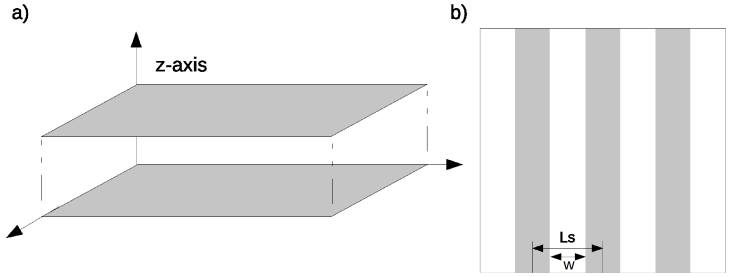

Figure 4.2: *(a): Setup and (b): mask on the bottom surface consisting of chemically activated stripes attractive to A block and B block alternately.*

We have considered systems of lateral size $L_x = L_y = 120$ with different thicknesses L_z ranging from 8 to 36 grid spacings. In every case, three different band periodicity of $L_S = 8$, 10, and 12 have been studied. These values guarantee that L_S is commensurate with L_x, so that L_x/L_S is an integer, to comply with the periodic boundary conditions. In the experimental work ref.[96] the authors have chosen a band periodicity $L_S \simeq L_0$, where L_0 is defined in Figure 4.1. Variations $L_S < L_0$ and $L_S > L_0$ were also studied in this last reference. Our choice of the values of L_S in the simulation aims at reproducing these experimental situations.

The equilibrium structures have been computationally determined by the dynamic evolution of the CDS from an homogeneous state on which we have superimposed a random perturbation to the order parameter field $\Psi = \pm 0.5$ at every grid point. The deterministic dynamics given in eq. (4.15) progresses until a final state, where no variation in the order parameter field is observed. In general, the evolution leads

to spherical domains characterized by values of the field $\Psi \simeq \Psi^{-}$, according to eq. (B.2). This dynamics correspond to a quench of the system at a given temperature below the critical temperature, which in our case is $\tau' = -0.14$ (see the Appendix). The progress of the quench dynamics starts with a fast process, dominated by spinodal decomposition, in which the domains grow from the local initial inhomogeneities. Then, it follows a much slower process of rearrangements of the domains in space and size. While the former process takes between 1000 to 10000 time-steps, the second takes of the order of 10^7 time-steps or longer. We recall that every time-step corresponds to a physical time a_0^2/M.

The approach to equilibrium can be monitored through the free-energy of the system given by eq. (4.21), which is a monotonously decreasing function of time. However, we cannot guarantee that the final structures, even after our long simulation runs, correspond to true equilibrium arrangements, since they could also be metastable states caused by local free-energy minima. To avoid the effect, we have added a random noise ζ [108,133] to the evolution equation eq. (4.15), according to

$$\Psi(i,j,k\,;t+1) = \Psi(i,j,k\,;t) - \{\langle\langle \Gamma(i,j,k\,;t)\rangle\rangle - \Gamma(i,j,k\,;t) + B\Psi(i,j,k\,;t) - \zeta\} \quad (4.23)$$

where ζ is a white noise process with a given amplitude. Fluctuation-Dissipation theorem does not apply here since this term is a computational artifact to overcome local free-energy barriers, and is not intended to reproduce thermal noise. We recall that the physical dynamics is deterministic with the temperature embedded in the parameter τ', which is the control parameter of the phase separation [105]. Hence, there is no inherent physical temperature scale in the amplitude of ζ as we use it along this work. In all cases, the final configuration is obtained after setting $\zeta = 0$ for, at least, 100000 time-steps before the end.

We employ a second dynamic procedure based on annealing. As before, the initial state is a homogeneous field with the same superimposed random inhomogeneities. Here, instead, the value of τ' is linearly lowered with time. We have chosen the system to decrease from $\tau' = 0$ to the final $\tau' = -0.14$ in a given lapse of the order of the total time. When performing the annealing, the free-energy does not significantly change until a threshold, that varies with the system, is reached. Then, the free-energy drops

near the final equilibrium value. Noise is also added to the dynamic evolution and switched off during the last 100000 time-steps.

The initial stages of two representative free-energy trajectories for quenching as well as annealing without added noise are shown in Figure 4.3. In this example the sudden change of slope in the annealing occurs at around $t \simeq 20000$, corresponding to $\tau' \simeq -0.11$. The dynamic routes to equilibrium are very different, depending on whether quenching or annealing is chosen, meaning that the system evolves through different intermediate structures depending on the route. In Figure 4.4 we show a sequence of intermediate structures from the same initial state and leading to the same final state, for both quenching and annealing. The final states are compared with regard to their free-energy, to elucidate which is more stable.

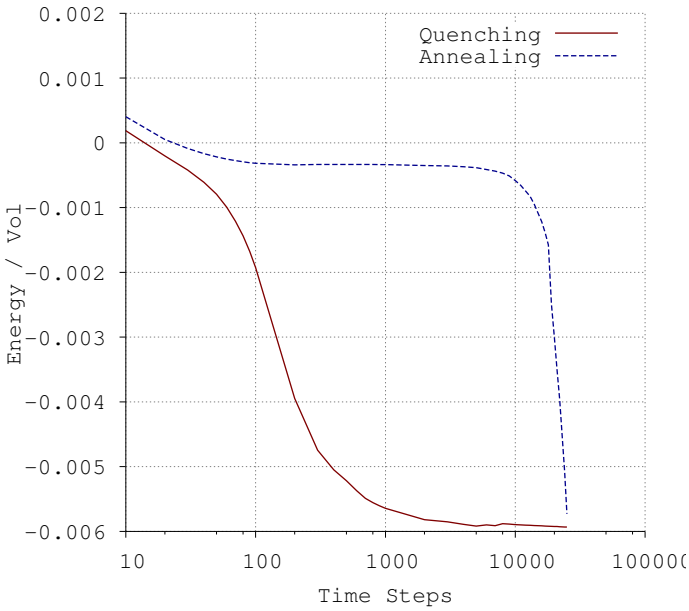

Figure 4.3: *Initial steps of the free-energy evolution for the quenching and the annealing processes without added noise.*

Without the addition of the noise, annealing would invariably produce metastable cylinders even close to the final temperature $\tau' = -0.14$. The noise, however, moves the system towards lower energy configurations consisting of ordered arrangements of spheres. Annealing is particularly useful for frustrated situations where quenching often leads to a final state consisting of a disordered array of spheres. The evaluation of the free-energy of the system permits us to discriminate the more stable configuration when the two routes produce different results for the same system.

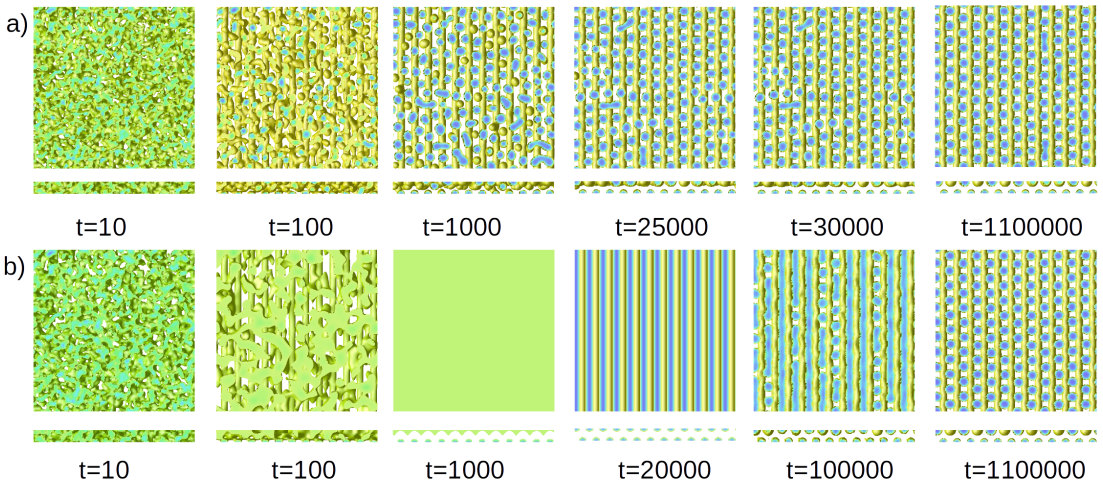

Figure 4.4: *Evolution of the configurations of a sphere-forming BCP confined by solid surfaces obtained by CDS; (a): quenching and (b): annealing. Box size* $L_x = L_y = 120$, $L_z = 10$. *The square frames show the top view, while the rectangles are side views in the* x*-direction, along which the stripes with* $L_S = 10$ *lie. The scale of colors ranges from yellow,* $\Psi^+ = 0.25$, *to blue,* $\Psi^- = -1.46$.

4.3.2 Slits $L_z \leq d$

Let us consider in the first place narrow slits whose thickness is of the order of or smaller than the BCP characteristic length d, which is proportional to the polymer chain length, $d \sim N^{2/3}$, according to eq. (B.11). This analysis permits us to check the validity of the model for the study of BCP systems under confinement.

Park *et al.*[96] experimentally studied P(S-*b*-MMA) block copolymers on chemically patterned surfaces giving spherical domains with $\varnothing \simeq 26.5$ nm and $d \simeq 65.2$ nm. Their experimental systems consist of a slit with different thicknesses and an area of $30 \times 400\ \mu\text{m}^2$, which presents a striped (line-and-space) pattern on the bottom surface, with a periodicity ranging from $L_S = 50.0$ to 60.0 nm (see Figure 2 in ref. [96]). The systems with $L_z = 25$ nm, which correspond to L_z significantly smaller than d, produce scattered spheres with no order, together with a wetting layer on the attractive bands. If we base our comparison between experimental and simulation results on d, these systems would correspond to $L_z \simeq 5$ and L_S from 8 to 10 grid spacings in our simulation.

As seen in Figure 4.5-a and -b, the structure predicted by our simulation $L_z = 6$ and $L_S = 8$ and 10, respectively, agree very well with the experimental results of ref.[96], shown in Figure 2 of this last reference.

Hence, the CDS can be compared with physical systems taking the characteristic

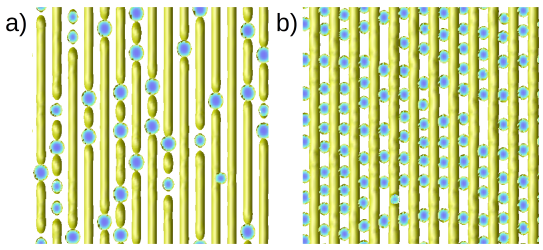

Figure 4.5: *CDS for sphere-forming BCP confined by solid surfaces. Bottom surface chemically activated with stripes and top surface neutral. Box size* $L_x = L_y = 120$, $L_z = 6$. *(a): Top view of the morphology with stripes whose spacing is* $L_S = 8$ *and (b):* $L_S = 10$.

distance d as a reference. Moreover, this good agreement in a narrow slit, where particular structures form, indicates that the free-energy functional given in eq. (4.7) is able to reproduce almost quantitatively the experimental results. Since its derivation is done for bulk systems[74,90], the kernel of the long-range contribution in eq. (4.7) should contain an explicit dependence on the distance z to the hard walls when $z < d$. However, in view of the comparison with experimental results, the effects of such contribution are not relevant and, therefore, one can use the isotropic propagator $G(\vec{r})$ in all cases, as a good approximation.

We next address the case of a thin slit $L_z = 8$ to analyze the effects of the width of the stripes on the structure of the BCP system. For comparison purposes, let us first consider a non-patterned homogeneous lower surface for which the boundary conditions are set to be the same as in the upper surface, as indicated in subsection 4.3.1. In general, these neutral boundary conditions favor the formation of semi-spheres (spherical caps) in contact with the hard walls if no other constraints are applied. Effectively, spherical caps at the surfaces permit the BCP chains close to the surface to lay unstretched parallel to the wall. Spheres tangent to the hard wall are not entropically favored due to the fact that polymer blocks in the corona shell are forced to squeeze between the sphere and the wall. This type of confinement of the BCP system produces frustrated situations when the natural periodicity of the BCP domains does not allow for the formation of such spherical caps at the upper wall.

From Figure 4.6-a we observe that two layers of semi-spheres are formed attached to both, the upper and lower surfaces. These semi-spheres have tendency to arrange in squares although the figure does not show a clear long-range order. This configuration may not correspond to an equilibrium system, which would display a long-range order

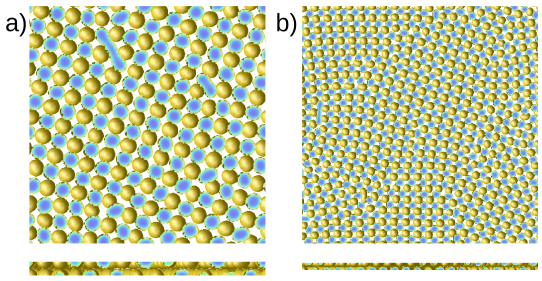

Figure 4.6: *CDS for sphere-forming BCP confined by two homogeneous and neutral solid surfaces. Blue dots correspond to half-spheres on the top suface while yellow caps are half-spheres at the bottom surface. Top and side view. Box size (a):* $L_x = L_y = 120$, $L_z = 8$, *and (b):* $L_x = L_y = 240$, $L_z = 8$.

structure with defects that could spontaneously appear and disappear due to thermal fluctuations. The defects are here a signature of a rather degenerated free-energy landscape and the dynamic process in eq. (4.4) is unable to arrive to the absolute minimum with an ordered phase, in a finite number of time-steps. The explicit consideration of the noise in this kind of situation could significantly change the phase diagram and the nature of the order-disorder transitions[19,67,101]. Figure 4.6-b shows a system four times the size of the one of Figure 4.6-a, after the same evolution time and from the same initial conditions. While isolated dislocations are visible in the smaller system, the larger system shows also grain boundaries. The difference between the two systems is attributed to the finite size effects of the box in the x and y-directions. The influence of PBC's in the system is weaker as the size of the box increases, since the mismatch between the natural periodicity of the BCP structures and the size of the box is shared among a larger number of domains the bigger the box is. Hence, we have to also take into account the ordering effect introduced by these finite-size effects associated to the box.

It may seem surprising that the dominating structure is not hexagonal but square. However, one should bear in mind that the slit thickness L_z is smaller than $d\sqrt{2/3} \simeq 9$, which is the distance between layers of spheres in hexagonal packing. Hence, the system chooses to form a square structure that permits the two layers of spheres to interpenetrate with regularity, in a way that hexagons cannot. Notice that the distance between 100-planes of a BCC whose distance between the central sphere and one at the vertex of the cell is approximately d, is of the order of $d/\sqrt{3} \simeq 6.3$, which is closer to the actual L_z. Therefore, the square structure is the result of the need of the system to accommodate two close layers of spherical caps.

The presence of the pattern of chemical stripes in the lower surface for the same system $L_z = 8$ has in general an ordering effect. However, the impact on the final configuration of spheres depends upon the commensurability of the periodicity of the stripes L_S and the characteristic lengths in the system. Let us first consider a pattern with band periodicity $L_S = 8$, which is approximately equal to the sphere diameter, but smaller than the natural distance between spheres, $d \simeq 11$. The structure with lowest energy in this case is given in Figure 4.7-a. On the bottom surface semi-cylindrical domains form wetting the A-attracting bands, while a layer of semi-spheres forms attached to the upper surface. Unlike for the non-patterned case, the bottom layer cannot freely accommodate to the structure formed on the upper surface due to the presence of the bands. Here the system must find an equilibrium between two competing effects, namely, i) to distribute the spherical caps in the upper layer in a compact ordered way, likely to be hexagonal, and, ii) to find the adequate match between the upper and lower geometrical distribution of domains. Figure 4.7-a shows a case where the former effect i) dominates the equilibrium structure, yielding a non-square layer of semi-spheres on the upper surface, unlike the non-patterned surface case. According to this, rows of semi-spheres form along the y-direction, with spheres separated a distance d. These rows are at a distance $L_0 \simeq 9.5$ from each other, off the band periodicity. For the rows of spheres to lie in the valleys between half-cylinders, the band periodicity should satisfy $L_S \simeq L_0$. Hence, when a row of spheres is in a valley, then the next row is placed slightly on the flank of a lying cylinder (surface reconstruction). The effect is additive across the x-direction, until another row of semi-spheres is located again in a valley n bands apart, where $n(L_0 - L_S) \simeq L_S$. For our system, $n \simeq 6$. The addition of the bands causes a change in the *native* arrangement, as shown in Figure 4.6, yielding a closer packing of spherical domains than in the non-patterned case. The structure, however, has many defects and in some regions square arrangements are also observed. In fact, simulations of larger system sizes, together with 2D Fourier transform of the patterns, indicate that there is no long-range order.

Moreover, we find out that the $L_S = 8$ system has also a rather degenerate free-energy landscape. Effectively, in Figure 4.8-a we show the regular structure obtained from the annealing route for the same system. The value of the free-energy is, however, larger than for the structure in Figure 4.7-a, obtained from quenching. The annealing

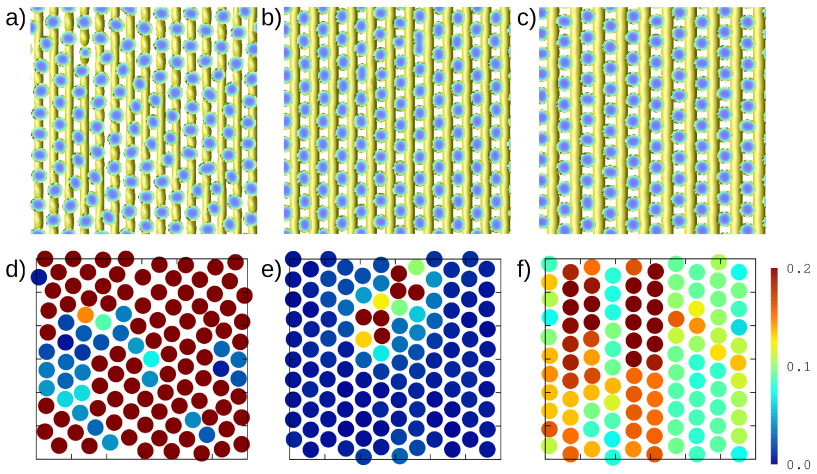

Figure 4.7: *CDS for sphere-forming BCP confined by solid surfaces. Bottom surface chemically activated with stripes and top surface neutral. Box size* $L_x = L_y = 120$, $L_z = 8$. *(a): Top view of the morphology with stripes whose spacing is* $L_S = 8$; *(b):* $L_S = 10$; *(c):* $L_S = 12$. *Euclidean distance of the local environments of each spherical domain to the HEX pattern, using a scale of colors. Dark blue indicates a small distance and dark red indicates a large distance to the HEX pattern; (d)* $L_S = 8$; *(e):* $L_S = 10$; *(f):* $L_S = 12$.

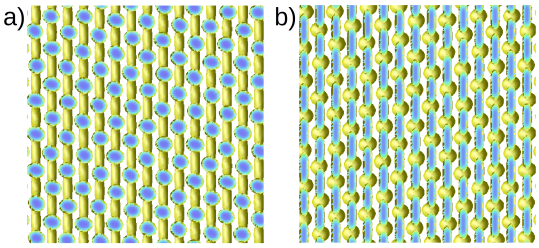

Figure 4.8: *CDS for sphere-forming BCP confined by solid surfaces. Bottom surface chemically activated with stripes and top surface neutral. State obtained from annealing and with* $L_S = 8$. *Box size* $L_x = L_y = 120$, $L_z = 8$. *(a): Top view and (b): bottom view.*

structure is rhomboidal with slightly larger half-spheres and lower surface density of domains than the corresponding quenched structure. In the annealing, the system chooses to place the half-spheres on top of the half-cylinders to allow a distance $l > d$ between them along the bands. The bottom view of the system, shown in Figure 4.8-b, reveals that the cylinders are broken at the position of the semi-spheres. The distance between neighboring semi-spheres on adjacent rows is again d, forming an isosceles triangle giving rise to the rhomboidal structure with $l \simeq \sqrt{4(d^2 - L_s^2)}$, instead of the square arrangement found for the non-patterned surface case. In summary, for this slit thickness and band periodicity, the effect ii) is clearly prevailing over the appropriate packing of the upper layer of spherical caps.

For the case $L_S = 10$ we force the commensurability between the natural distance

for a 2D HEX structure and the periodicity of the stripes $L_S \simeq L_0$, according to Figure 4.1. In this particular case, both requirements i) and ii) are simultaneously satisfied by the pattern formed in the upper layer, which is effectively hexagonal, as can be seen in Figure 4.7-b. Finally, the case $L_S = 12$ yields a regular structure with the spherical caps of the upper surface also lying in the valleys between half-cylinders. However, the structure is forced to comply with the periodicity imposed by the stripes in the x-direction. The structure is slightly stretched yielding a distance between half-spheres belonging to parallel rows approximately $\sqrt{L_S^2 + d^2/4} \simeq 13.2$. The distance between spheres in the same row is hence slightly smaller than d. Here, wider bands seem not to allow spherical caps to form on top, as it was the case for $L_S = 8$ and no surface reconstruction occur. The resulting structure is similar to the hexagonal, as seen in Figure 4.7-c. In Figure 4.7-d, -e, and -f we show the euclidean distance (cf. Appendix) of the local environments of each spherical domain to the HEX pattern. While for the system $L_S = 8$ only some spherical domains are surrounded by a clear hexagonal structure, for $L_S = 10$ Figure 4.7-e indicates that such a structure is dominant, except for a few defects. Finally, when $L_S = 12$ the system shows a clear deviation from a hexagonal symmetry. The distance of the $L_S = 12$ structures to the (110) BCC pattern is even larger than to the HEX.

The next case studied is $L_z = 10$ for which the slit thickness is of the order of d. Firstly, the system $L_S = 8$ in Figure 4.9-a approximately corresponds to $L_z = 57$nm and $L_S = 50$ nm in ref. [96]. As before, we use $d = 11 \approx 65.2$ nm for the comparison. Here, the regions with squares, observed for a thickness of $L_z = 8$, *cf.* Figure 4.7-a, have disappeared. The matching between the patterns in the upper and lower layer for this band periodicity is less stringent for a thickness of the order of the natural distance between spherical domains. Then hexagonal structures are observed, although no long-range order exists, in agreement with the experimental results (see Figure 4 in ref. [96]). Our CDS results thus confirm that the narrow bands are not capable of guiding the assembled BCP spherical domains towards a regular pattern with long-range order. Again, surface reconstruction occurs as an undesirable result causing the mismatch between the natural spacing of the spheres and the band periodicity.

Secondly, the system with $L_S = 10$ (Figure 4.9-b) produces a well ordered upper layer of spherical caps. These results are in perfect agreement with the corresponding

system $L_z = 57$ nm and $L_S = 60$ nm described in Figure 4 from Park *et al.*[96]. As compared with the previous cases, here the system prefers to form a 2D HEX layer of spherical caps which perfectly matches the periodicity of the stripes of the bottom layer.

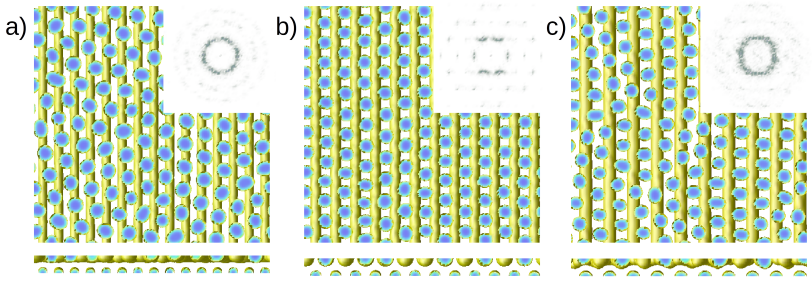

Figure 4.9: *CDS for sphere-forming BCP confined by solid surfaces. Bottom surface chemically activated with stripes and top surface neutral. Top and side view of the morphology when the box size is* $L_x = L_y = 120$, $L_z = 10$ *and the stripes have a spacing of (a):* $L_S = 8$*; (b):* $L_S = 10$*; (c):* $L_S = 12$*. The insets show the corresponding 2D Fast Fourier transform.*

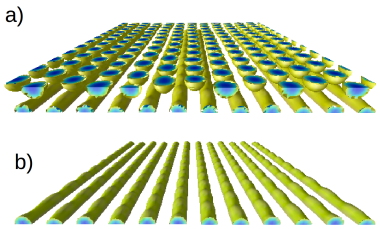

Figure 4.10: *3D view of the system* $L_x = L_y = 120$, $L_z = 10$ *with* $L_S = 10$ *at different heights (a):* $L_z = 4$*, and (b):* $L_z = 10$.

Figure 4.10 shows the system $L_S = 10$ cropped at $z = 4$. One can distinguish knurled cylindrical domains which also reproduce experimental observations[96]. Notice that for this thicker system the influence of the top layer on the bottom one is lower than in the thickness $L_z = 8$. Beyond the band periodicity experimentally studied we have also analyzed, in the third place, the case $L_S = 12$ that would physically correspond to 71 nm. This band periodicity matches approximately with $2d/\sqrt{3} \simeq 12.7$ corresponding to the side length in a BCC unit cell where the shortest distance apex-center is approximately d. For this particular case, the bands are not capable of producing a system with a neat ordered pattern, but rather the structure of the upper layer is locally hexagonal without long-range order. The ordering effect of the upper hard wall determines the preference for the 2D HEX packing on this layer of spherical caps. In this sense, it is different from what we have observed for the same

band periodicity but with a slit thickness of 8 (c.f. Figure 4.9-c). This fact indicates that for this slit thickness and for this band periodicity, the pattern of the upper layer dominates on the complementarity between the patterns in the upper and lower layer, as also happened for the narrow bands. This observation is against the idea that the periodicity in the x-direction is imposed by the band spacing[96].

It is particularly interesting that a slight increase of the slit thickness from $L_z = 10$ to 12 for the same $L_S = 12$ produces a completely different scenario, which is shown in Figure 4.11. The pattern has long-range order and is rectangular, slightly stretched in the y-direction. The new pattern arises by placing an additional layer of complete spheres between the upper and lower layers of half-domains. Then, the periodicity of the arrangements of spheres in the x-direction perfectly matches the band spacing. The dimensions of the unit cell are estimated 12 in the x-direction, which is precisely the band periodicity, and 13.3 in the y-direction, parallel to the stripes. For this last case, therefore, the dominating effect is not the packing of the caps in the upper layer, but the band periodicity which enforces a body-centered orthorhombic (BCO) cell to pack a new layer of complete spheres between the semi-cylindrical structures and the spherical caps at the bottom and top walls, respectively.

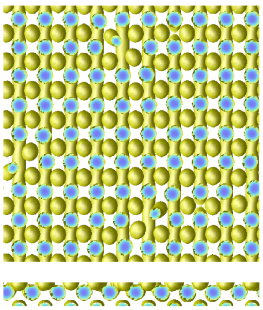

Figure 4.11: *CDS for sphere-forming BCP confined by solid surfaces. Bottom surface chemically activated with stripes and top surface neutral. Top and side view for a system with box size* $L_x = L_y = 120$, $L_z = 12$ *and* $L_S = 12$.

4.3.3 Slit $L_z = 14$

We also investigated the morphology of systems contained in a slit with thickness $L_z = 14$, with striped surfaces with $L_S = 8$, 10, and 12, as in the previous section. This case is particularly interesting because the system is frustrated if 2D HEX layers are to be formed in a slit where L_z is slightly larger than d. The spherical caps forming

2D HEX pattern of the previous $L_z = 10$ case are transformed in a layer of complete spheres almost tangent to the hard wall, which is entropically unfavorable due to the stretching of the corona blocks under this conformation.

The first case $L_S = 8$ produces complete tangent spheres locally ordered in hexagonal arrangements in addition of the half-cylinders formed on the lower hard wall, according to Figure 4.12-a. Some of the domains in the upper layer, however, are deformed into eggplant-like structures due to the aforementioned frustration. The overall behavior is very similar to the previously studied cases for the same band periodicity, with surface reconstruction with a local HEX non-commensurate order with respect to the periodicity of the cylinders (x-direction), and lost of long-range order in larger systems (not shown). Hence, bands cannot guide the assembly of the upper layer of spheres, which is dominated by the i) mechanism.

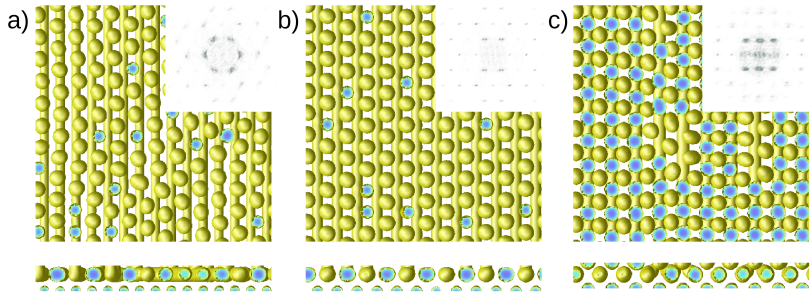

Figure 4.12: *CDS for sphere-forming BCP confined by solid surfaces. Bottom surface chemically activated with stripes and top surface neutral. Top and side view of the morphology when the box size is* $L_x = L_y = 120$, $L_z = 14$ *and the stripes have a spacing of (a):* $L_S = 8$*; (b):* $L_S = 10$*; (c):* $L_S = 12$*. The insets show the corresponding 2D Fast Fourier transform.*

As expected, for the case $L_S = 10$ there is a clear effect of the commensurability $L_S \simeq L_0$, in view of Figure 4.12-b. The arrangement obtained corresponds to upper layer of complete spheres laying tangent to the hard wall, with a long-range 2D HEX symmetry. Some defects in the form of eggplant domains are also present, but the distribution of domains in the upper layer is similar to the previous cases studied for this band periodicity. Our simulation results are in agreement with the patterns encountered in the system $L_S = 60$ nm in a slit $L_z = 70$ nm.[96], although we find a slightly better long-range ordered structures.

Finally, the most interesting situation occurs by increasing the band periodicity to $L_S = 12$. Figure 4.12-c shows an extra layer of domains that are formed in contact with the upper wall. The order is long-range and would correspond to a crop of BCO with

square base. Here, the formation of the new layer and the restructuring of the layer of complete spheres permits to match the periodicity imposed by the bands (mechanism ii)) without jeopardizing the preferred distances between spheres and spherical caps. This is a clear example of the interplay of both, the band periodicity and the slit thickness through the favored 3D cell by the combination of the two causes. In this latter case, the fact that the slit thickness is close to $2d/\sqrt{3} \simeq 12.7$ and that the band periodicity is precisely close to this same length induces the formation of a body-centered unit cell.

4.3.4 Thicker Slits

In the previously analyzed cases we have verified that the sphere-forming BCP are very sensitive to the band periodicity, which should be commensurate with the characteristics distance d of the BCP in order to produce neat ordered arrangements. We have seen that the vertical confinement also plays an important role in determining the final structure. In general, we may further state that the system prefers forming spherical caps and half-cylinders in contact with the solid walls, separated a distance proportional to d. This was approximately the case for $L_z = 10$. However, if the separation between walls is roughly $d\sqrt{2/3}$, the upper layer is forced to produce tangent spheres if the system packs in a 3D HEX, as in $L_z = 14$, instead of spherical caps on the surface. Therefore, in the z-direction, the characteristic length d, together with the type of unit cell, also impose a periodicity that determines the final equilibrium structure, leading to the entanglement of band periodicity and slit thickness. It is this case for the bands satisfying $L_S = 12$, where an extra layer of spherical caps forms in $L_z = 14$, where only one layer of complete spheres existed for smaller band periodicity. In the analysis of thicker systems, addressed in this subsection, is thus convenient to rationalize these rules of thumb, including the needed geometrical prefactors depending on the chosen unit cell.

If the system forms n layers of complete spheres stacked in a 3D HEX ordering, then the appropriate slit thickness is approximately given by

$$L_z(\mathrm{HEX}_1) \equiv (n+1)d\sqrt{\frac{2}{3}} \tag{4.24}$$

We have considered that the distance between neighboring spheres is approximately d and that the distance between layers parallel to the walls is $d\sqrt{2/3}$, corresponding to a 3D HEX packing. An additional layer of spherical caps forms in contact with the top surface. The distance between the half cylinders at the lower surface and the first layer of spheres has been assimilated to the distance between planes. In the same way, if the system is keen to form a BCC unit cell with the base parallel to the hard walls, the appropriate slit thickness should be approximately given by

$$L_z(\mathrm{BCC}) \equiv (n+1)\,\frac{d}{\sqrt{3}} \tag{4.25}$$

Here, the distance between layers is $d/\sqrt{3}$, as it corresponds to (100)-planes of a BCC. Again, a layer of spherical caps is considered to form on the upper wall while the shortest distance between neighboring spheres is assumed to be approximately d, corresponding to the distance between the spheres in one vertex of the cube and the center. Slit thicknesses laying off these periodicities impose some degree of frustration in the system, which may produce slightly stretched or compressed unit cells, or the formation of entropically unfavorable tangent spheres near the upper wall. In particular, a slit thickness given by

$$L_z(\mathrm{HEX}_2) \equiv \left(n+\frac{1}{2}\right) d\sqrt{\frac{2}{3}} \tag{4.26}$$

with HEX packing would produce such a frustrated system with tangent spheres. Eqs (4.24) - (4.26) cannot be taken as exact by different reasons, the most important being that the system can modify its characteristic length under constraint to a given extent. They only give a rough estimate of what one can expect.

In the first place, let us study the structures obtained for the three band periodicities $L_S = 8$, 10, and 12 for systems with slit thicknesses $L_z = 20$, 24, and 36. The particular thicknesses chosen for the first and the third cases correspond to values that approximately comply with eq. (4.24), with $n = 1$ and $n = 3$, respectively. The second thickness roughly corresponds to eq. (4.26) with $n = 2$. In Figure 4.13 we show the structures obtained for the mentioned periodicities and thicknesses.

Firstly, let us center our attention to the case of a band width $L_S = 8$. Here, the structure is dominated by the geometrical confinement. Figures 4.13-a and -g show a 2D hexagonal pattern in the upper layer, with spherical caps. Figure 4.13-d shows

the same structure but for tangent spheres. The mismatch between the band width and the 2D HEX pattern is seen in the lateral sections of the systems in the same set of figures. Although the system shows local order, many defects in the structure are visible for the three thicknesses.

Secondly, Figures 4.13-b, -e, and -h correspond to a band periodicity $L_S = 10 \simeq d\sqrt{3}/2 \equiv L_0$, compatible with the formation of a 2D hexagonal pattern in the first layer of spheres (bottom up). For the three thicknesses, we observe long-range order in all the layers. From $L_z = 36$ we further see that the three and a half layers of spheres are packed in a clear 3D HEX, with a distance between layers of spheres $\delta \simeq 9 \simeq d\sqrt{2/3}$. Effectively, from the top view of Figure 4.13-h we see that the spheres of the top layer of spherical caps and the third layer are located where it corresponds to this structure (see also the lateral view). The calculation of the Euclidean distance at each layer of spheres also reveals that the local structures are indeed hexagons (Euclidean distances to the pattern are of the order of 10^{-2}). The case $L_z = 24$ corresponds to tangent spheres. The system keeps the overall HEX configuration despite the fact that tangent spheres are entropically not favored by the stretching of the corona B-blocks. It is worth to remark that the distance between planes for this latter case is $\delta \simeq 9.6$ instead of 9, slightly stretched with respect to a 3D HEX packing.

Thirdly, Figures 4.13-c, -f, and -i correspond to a band width $L_S = 12$. This band width is close to the lateral size of a BCC cell, as we have described above. With this constraint on the first layer, the system builds a BCO, with a distance between planes $\delta \simeq 6.1$ for the thickness $L_z = 20$, which is very close to the separation between (100)-planes of the BCC lattice, namely, $\delta = d/\sqrt{3} \simeq 6.35$. For the thickness $L_z = 24$, the separation is slightly larger $\delta \simeq 7.7$, as if the system is *stretched* in the z-direction. These two cases present overall long-range order although some defects are visible. However, in Figure 4.13-i we see that the system shows no local order due to the mismatch between the side length of the BCC unit cell and the slit thickness. The system cannot keep the body-centered order and form tangent spheres at the same time.

Before closing the analysis of the results, several comments are in order. It is well known that the sphere-forming BCP organize in bulk in BCC three dimensional structure[8]. The transition between the 2D hexagonal morphology near a non-patterned

surface and the bulk BCC cell has been studied in refs. [125, 126]. These authors find a first order transition at $n \approx 4$ between a 2D HEX and a face-centered orthorhombic unit cell, which smoothly tend to the bulk BCC as the layer lays farther from the hard surface. Our simulations for $L_S = 10$, which favors the HEX pattern, thus agree with this experimental finding, particularly when the slit thickness corresponds to eq. (4.24) and, therefore, the possible distorting effect of the upper hard wall is minimized. We have found, however, deviations from the expected behavior of 3D HEX packing in $L_z = 26$, with the same band periodicity $L_S = 10$. Here the slit thickness is close to but smaller than the one given in eq. (4.24) with $n = 2$, and is therefore frustrated. Notice that with respect to the case $L_z = 24$, where the upper layer is tangent to the upper wall, the system discussed forms an additional layer of spherical caps, but not completely developed as shown in Figure 4.14-a. In Figure 4.14-b, -c and -d, we show the ratio between the Euclidean distances of the local structure to the 2D HEX and the (110)-plane of BCC. Large values of this ratio indicates that the local environment is closer to the (110)-plane of BCC than to the 2D HEX. Despite the fact that the pattern of the lower surface favors the formation of hexagons, the first layer (bottom up) displays a domain arrangement significantly closer to the (110) BCC than to the HEX. The second layer, however, shows some more disperse particles surrounded by a HEX environment, while the upper layer of spherical caps is more hexagonal. Obviously, the upper hard wall also imposes a strong confinement constraint that induces a major packing in this layer, favoring the 2D HEX. However, it is remarkable that the system shows a body-centered structure, close to the bulk BCC, near the lower surface, without passing through intermediate forms of the type of face-centered orthorhombic, as was observed in refs. [125, 126]. For completeness, in Figure 4.14-e,-f,-g we show the histograms of the distances between every sphere in a given layer to its six closest neighbors. Two peaks are clearly distinguished corresponding to the two characteristic distances of the (110) BCC plane, in the first and second layer. The ratio, a_1/a_2, between these two main distances is the order parameter used to describe the transition from HEX to BCC in the aforementioned references. From the histograms we approximately obtain $a_1 \simeq 10.8$ and $a_2 \simeq 12.4$, yielding $a_1/a_2 \simeq 1.15$, which confirms that the layer indeed corresponds to a (110)-plane of a BCC. One can then argue that the formation of partial spherical caps on the upper surface *compresses* the structure in the z-direction, since

$\delta \simeq 8$ instead of 9, as it would correspond to the distance between (110) BCC planes. This distance is precisely also the separation between layers for a 3D HEX packing. Therefore the structure is a part of a body-centered rhombohedron (BCR), instead of the previously observed BCO, due to this compression. It is quite surprising that the surface density of spheres is the same, despite the fact that the distance between planes is smaller, as in the close system $L_z = 24$, which displays a clear 3D HEX packing of the layers. This can be observed from the ratio of the Euclidean distances as well as from the histograms in Figure 4.15. This behavior is rather counterintuitive, since the 3D HEX permits a larger packing density than a BCC for hard spheres. The presence of the bands seems to hinder the displacements of the system in the x-direction. Hence, with respect to the HEX arrangement in the $L_z = 24$ system, here the first layer presents a slight shift of the rows of spheres in the y-direction to produce the (100) BCR plane. The next layer is then allocated at the corresponding position for a (100) BCR plane, as observed. Hence, the BC rhombohedron seems to have more capacity to absorb *pressure* on the structure by favoring displacements along the bands.

A second frustrated system with $L_S = 10$ corresponds to the case $L_z = 34$, which corresponds to a slit thickness complying with the formation of three layers of complete spheres, but not thick enough to form spherical caps. Hence, we have an upper layer of tangent spheres with some egg-plant defects. The interesting feature of this system is that the domains adopt an 2D hexagonal packing, but when analyzing the 3D packing, one observes that is not 3D HEX, but closer to a (111)-plane of face-centered cubic phase, since the first and the third layer are not superposed in the xy plane. The packing density of both 3D structures is, however, the same. Thus, the reason for this new structure is difficult to find out and it is even possible that the equilibrium for this thickness is degenerated with two possible structures of maximum packing.

We have also analyzed systems of $L_z = 54$ and 56 with the band periodicity $L_S = 10$, capable of allocating 5 layers of complete spheres, tangent to the upper wall or with spherical caps in it, respectively. The 3D HEX order is maintained in the $L_z = 56$, with a plane separation approximately $\delta = 9.3$. As before, the system with tangent spheres, $L_z = 54$, produces (111)-planes of a face-centered body, with $\delta \simeq 9.8$, and many egg-plant defects at the upper layer. However, for $L_S = 12$ we obtain disordered systems for $n \leq 4$ layers of complete spheres, even with the appropriate L_z as given in

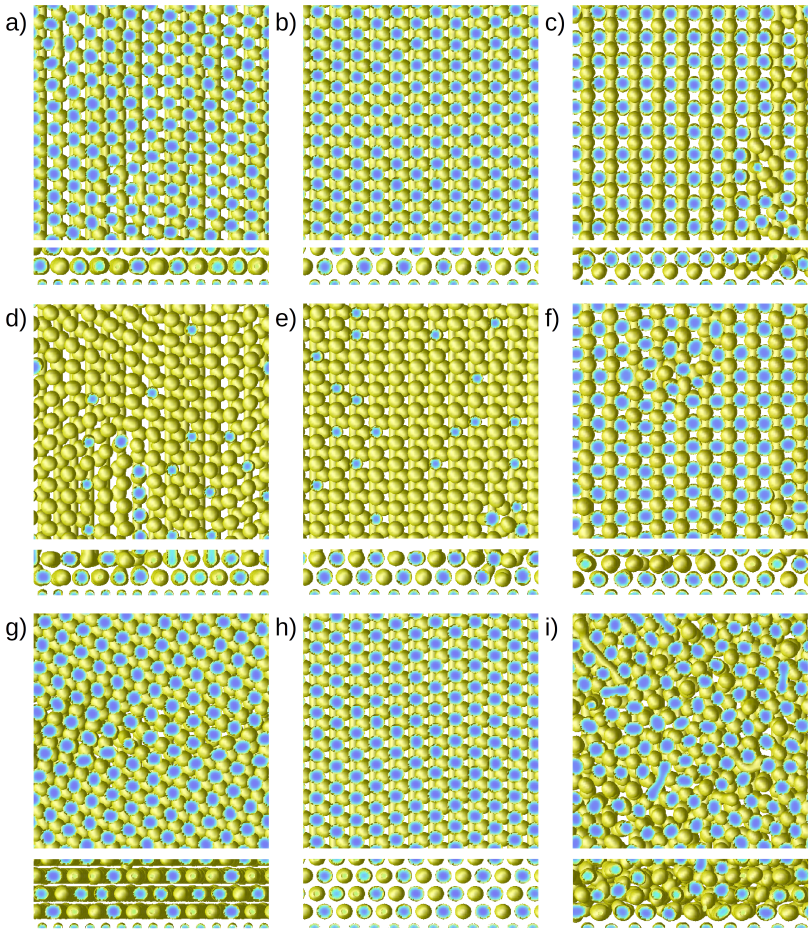

Figure 4.13: *CDS for sphere-forming BCP confined by solid surfaces. Bottom surface chemically activated with stripes and top surface neutral. Top and side view of the morphology when the box size is* $L_x = L_y = 120$, $L_z = 20$ *and the stripes have a spacing of (a):* $L_S = 8$*; (b):* $L_S = 10$*; (c):* $L_S = 12$*. Box size* $L_x = L_y = 120$, $L_z = 24$ *and lattice spacing of the stripes (d):* $L_S = 8$*; (e):* $L_S = 10$*; (f):* $L_S = 12$*. Box size* $L_x = L_y = 120$, $L_z = 36$ *and lattice spacing of the stripes (g):* $L_S = 8$*; (h):* $L_S = 10$*; (i):* $L_S = 12$*.*

eq. (4.25), for both, quenching and annealing.

4.4 Conclusions

In this chapter we have shown that the CDS is a powerful tool to predict the self-assembly of block copolymers into complex structures. The simulations of sphere-forming BCP on patterned surfaces confined in a slit, addressed in this work, have been compared with the experimental data from Park *et. al.*[96] and an almost quantitative agreement is shown. The comparison is done in terms of only one single characteristic length, namely, $d \sim N^{2/3}$. The size of the domains of a given block seems to play a secondary role provided that the domain geometry keeps being spherical.

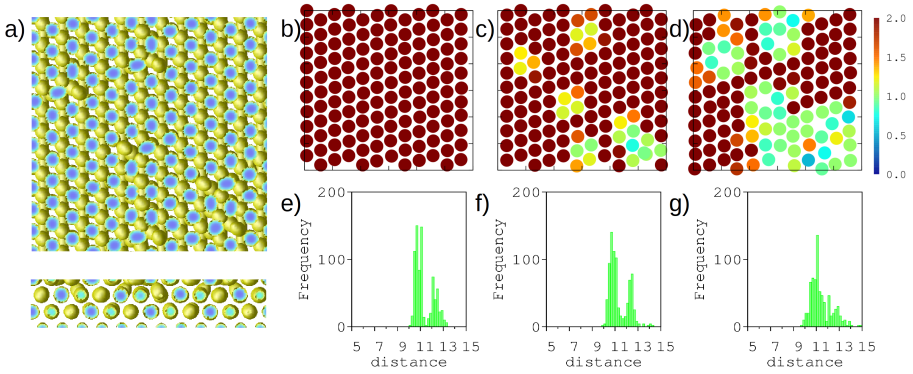

Figure 4.14: *CDS for sphere-forming BCP confined by solid surfaces. Bottom surface chemically activated with stripes and top surface neutral. Box size $L_x = L_y = 120$, $L_z = 26$ and stripes with a spacing of $L_S = 10$. (a): Top and side view of the morphology. Ratio of the Euclidean distance to HEX symmetry and distance to BCC symmetry ($d_{\mathrm{HEX}}/d_{\mathrm{BCC}}$)(b): lower layer; (c): middle layer; (d): upper layer. Histogram of the distances of each sphere with its 6 next nearest neighbors (e): lower layer; (f): middle layer; (g): upper layer.*

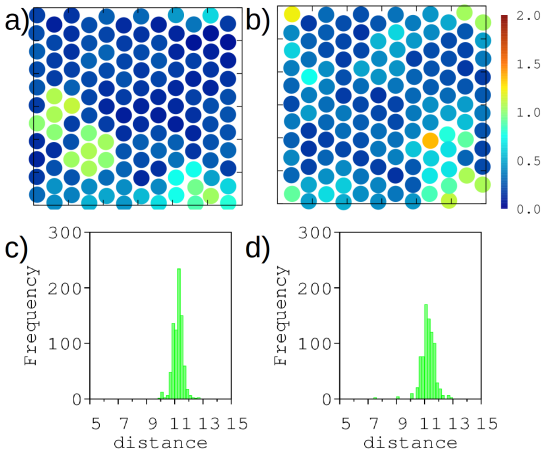

Figure 4.15: *CDS for sphere-forming BCP confined by solid surfaces. Bottom surface chemically activated with stripes and top surface neutral. Box size $L_x = L_y = 120$, $L_z = 24$ and stripes with a spacing of $L_S = 10$. Ratio of the Euclidean distance to HEX symmetry and distance to BCC symmetry ($d_{\mathrm{HEX}}/d_{\mathrm{BCC}}$)(a): lower layer; (b): upper layer. Histogram of the distances of each sphere with its 6 next nearest neighbors (d): lower layer; (e): upper layer.*

Due to this inner simplicity of the problem, the structures that can be formed are rather limited by the bulk BCP equilibrium configuration and the hexagonal packing produced by the presence of a hard wall. The main result of this work lies in the fact that we have shown how chemically patterned surfaces together with suitable slit thicknesses can select one of these two arrangements and form long-range order structures, at least of the order of the size of the simulated systems. Along with the minimal distance between domains d, the system is sensitive to the band periodicity in relation with the 3D structure that one wishes to promote. In this way, if the band

periodicity is approximately $L_0 = d\sqrt{3}/2$, the first layer of complete spheres (bottom up) will naturally be hexagonal. It is additionally required, however, that the slit thickness is appropriate for a 3D hexagonal cell to develop without conflict with upper surface constraint, as described in eq. (4.24). On the contrary, if the band periodicity is approximately $2d/\sqrt{3}$ and the slit thickness is approximately given by eq. (4.25), the system will naturally develop a BCO structure already from the first layer. This fact is significantly different from what occurs in the presence of a non-patterned lower surface, where the confining effect of the hard wall imposes a preference for a hexagonal structure. This result is a pure prediction of the CDS since no experiments have been done under these conditions, to the best of our knowledge.

We have also analyzed frustrated situations to explore the possibility of existence of exotic structures generated by the constraints, for the same physical system. On one hand, we have encountered hexagonally packed ordered systems with spheres tangent to the upper wall, formed on stripes with band periodicity $L_S = L_0$, by tuning the slit thickness to approximately that of eq. (4.26). This type of situations have been also observed in the experiments. For this type of frustration, the layer separation $\delta > d\sqrt{2/3}$ as it would correspond to the perfect 3D HEX. This effect can be caused by the presence of egg-plant defects, which are deformed domains cut by the upper wall, to favor the conformation of the BCP chains near the wall, pulling the whole system up. On the other hand, we also have studied systems whose thickness is in between the values given by eqs (4.24) and (4.26), both with $n = 2$ layers of complete spheres. We have analyzed only the case $L_S = L_0$. We have observed that the first and second layers have a clear structure of a (110)- plane of a BCC instead of an expected HEX, probably due to a subtle effect of the bands on the possible displacements of the spheres under changing external conditions, which deserves further investigation. This case shows a distance between the layers slightly compressed $\delta < d\sqrt{2/3}$, which can be attributed to the presence of incomplete spheres, cut by the wall between its pole and equator, that push the whole system down. Hence, the fine tuning of the slit thickness is also of crucial importance to obtain the desired ordered three-dimensional structures.

The analysis carried out in this work suggests that the use of chemical masks on surfaces, together with the control of the thickness can be a useful tool to create the desired structure from the self-assembly of BCP. We believe that this is a step forward

towards the applications of this systems in well controlled fabrication of nanoscopic devices.

Chapter 5

Conclusions and Future Work

This thesis is divided into two well-defined parts. Here, in this last section we give the most important conclusions of each part.

In Chapter 2, we have found that the mechanical response of the multilayer films of LLDPE/EVOH, in terms of the storage and loss moduli obtained by dynamic mechanical analysis (DMA), can be well predicted by a simple mixing rule based on the mechanical independence of the layers and the negligible role of interfacial effects. Therefore, the response of the different sandwiches with the same overall thickness depends mainly on the volume fraction of EVOH and not on the number of layers. With this mixing rule we can obtain an estimate of the response of a given sandwich from the data of pure components, but only if the sandwich, as well as the films of pure components, have been processed under the same conditions. The analysis of destructive tensile properties indicates that the material is anisotropic with regard to the machine and cross directions, proving the strong non-equilibrium microscopic structure that remains in the material after solidifying. The observed properties are compatible with a material formed by crystallites oriented preferably in a plane orthogonal to the draw direction, perhaps with bundles of rather oriented fibers along the draw direction. Nevertheless, our macroscopic study cannot directly give insight on the particular structural changes giving rise to the differences, and should be complemented with direct observation of the microstructure of the films. We can conclude that the particular properties of multilayered films are not due to the confinement itself but to the effect of the strain and molecular orientation of the film in the solidification process. This fact, however, does not preclude that the confinement may play a role on the analyzed properties, but such

a role is not dominant.

In regard to the modeling analyzed in Chapter 3, we have found that the viscoelastic response of the LLDPE and EVOH bars can be depicted with a simple Generalized Maxwell (GM) model. However, in the case of the stretched films, we introduced a nonlinear term in the model that allow us to obtain a good agreement with the experimental data. These non-linearlities, which we implemented as correction terms to the GM model, take into account the stretching of some particular modes due to the processing conditions, which are customarily assumed to be in the amorphous fraction. The spectra of relaxation-times obtained show some structural information about the studied materials. From the analysis of the spectra one can draw several conclusions. The transformations that the materials suffer with the temperature, known as relaxation transitions and commonly identified with peaks in the $\tan\delta$ curve, are also visible in the spectra of relaxation-times. With the incorporation of the non-linearities in the GM model, to comply with the mechanical response of our stretched films, we gather information about the main changes on the spectra when the films are compared to the bars. We find that, at the higher temperatures studied, the materials behave linearly, i.e., well described by the generalized Maxwell model. As the temperature is lowered, the non-linearites start to become significant, specially for some relaxation modes. With regard to the multilayers films, the construction of spectra through a weighted superposition of the spectra of the pure constituents, making use of the mixing rule, shows a similar trend in comparison with the spectra calculated directly from the experimental storage and loss moduli data. Hence, although the mixing rule depicts the basic behavior, the breakdown of the superposition is a clear signature of the fact that intrinsic structural changes occur when we confine the inner layers in the sandwich films.

In view of the analysis done in this thesis regarding the first system, some questions remain open which will be interesting lines for future research. On the one hand, it would be very interesting to find what is the real molecular structure of the stretched films. Obviously, these can only be achieved through microscopy and spectroscopy of different types, like atomic force microscopy, transmission electron microscopy, and small and wide-angle X-ray scattering. Additionally, it would be interesting to have access to a much wider range of frequencies, for example, through dielectric relaxation

measurements. With this data new, broader spectra, could be obtained and compared with the ones given in Chapter 3. Perhaps, important contributions are now hidden inside the lumped asymptotic parameters, which could be revealed with this kind of experiments. In this sense, we could check the reality of the encountered peaks as well as how the nonlinear corrections may change when a much wider spectrum can be straightforwardly obtained. Finally, we are left with the question about what kind of motions are underlying the more important peaks found in our materials and, therefore, clearly identify the mechanical processes responsible for the observed data in the DMA experiments. Large scale simulations, of mesoscopic as well as detailed microscopic elements could be useful for establishing these correlation between spectrum and microscopic behavior.

The last chapter of the thesis, Chapter 4, is devoted to the investigation through Cell Dynamics Simulations (CDS) of the equilibrium structures that are formed by sphere-forming block copolymers (BCP) in thin films onto a chemically patterned surface. The aim is to find the proper conditions to obtain well-ordered arrays of spheres useful for many nanotechnological applications. With this purpose, we use a striped pattern consisting of bands attractive to the one or the other species forming the blocks of the copolymer, in an alternate way, along the lines of the experimental work of *Park et. al.*. We have found that, although the band periodicity has a guiding effect, there is also an important interplay between this band periodicity and the film thickness, which eventually determines the final structure of the system. The key factor is that the BCP brings one important characteristic length, d, that accounts for the separation between spherical domains. Such an intrinsic domain periodicity has to be commensurate with any of the other two periodicities, namely, the one of the chemical substrate and the thickness of the layer as well. Hence, when the band periodicity is commensurate with d, the system organizes its domains into a long-range ordered hexagonal array. It is additionally required, however, that the slit thickness complies with the appropriate proportionality for a 3D hexagonal cell to develop without conflict with upper surface. On the other hand, if the band periodicity is slightly larger, the system is prone to develop a body-centered orthorhombic arrangement of domains when the system thickness is again commensurate with this kind of structure. Additionally, performing a systematic study for the given band periodicities, we have encountered frustrated situ-

ations corresponding to film thicknesses not commensurate with the vertical length of the natural 3D structure. Hence, the fine tuning of the slit thickness is identified to be of crucial importance to obtain the desired ordered 3D structures.

With regard to the perspectives for this part of the work, it would be possible now that a better understanding is reached in terms of the key factors that contribute to the ordering of the spherical domains, to extend the investigation to other kind of designs in the pattern. New complex morphologies could arise and a better control on the ordering could be achieved. From a more fundamental point of view, the fact that the system can change its unit cell under the variation of an external order parameter like the band periodicity opens the door to the study of these structural transitions. One can speculate whether this transitions are of second order in analogy with other morphological transitions occurring, for instance, in metal alloys. From a computational point of view, the introduction of the discrete free-energy in Chapter 4 is an essential tool to achieve this goal, namely, to locate the transitions in the space of parameters and determine its nature. Furthermore, since CDS is a dynamic procedure it would be rather natural to study the dynamics of the transition in the vicinity of the critical point. Finally, it would be of a certain interest to analyze more in depth non-commensurate situations because exotic structures of particular interest could see the light when putting the system under forced frustration.

List of Publications

M. Serral, M. Mangnus, P. Sandkühler, J. Bonet Avalos

Viscoelastic Response of Multilayer Polymeric Films of Linear Low-Density Polyethylene and Ethylene Vinyl Alcohol Copolymer

Polymer Engineering and Science

Published online: November 2014

M. Serral, M. Mangnus, P. Sandkühler, J. Bonet Avalos

Linear low-density polyethylene and ethylene vinyl alcohol copolymer multilayer films

Plastic Research Online

Published online: February 2015

M. Serral, M. Mangnus, P. Sandkühler, J. Bonet Avalos

Modeling of the Viscoelastic Response of Multilayer Polymeric Films of Linear Low-Density Polyethylene and Ethylene Vinyl Alcohol Copolymer: Structural Analysis from the Relaxation-Time Spectra

(In preparation)

M. Serral, M. Pinna, A. Zvelindovsky, J. Bonet Avalos

Cell Dynamics Simulations of sphere-forming diblock copolymers in thin films on chemically patterned substrates

(In preparation)

Appendix A

Viscoelastic model

A.1 Continuous Distribution of Maxwell Elements

Let us assume that each species (polymer segments of different length) in the sample contributes with a single response and that the observed behavior is the superposition of the different responses. Thus, the linear viscoelatic response of one single element n is given by

$$\sigma_n(t) = \int_0^t dt'\, \tilde{E}_n(t-t')\dot{\varepsilon}(t') \tag{A.1}$$

with σ the stress and ε, the unitary elongation. Furthermore, the information concerning time-dependent material behavior is contained in the relaxation modulus,

$$\tilde{E}_n(t) = E_n\, e^{-t/\tau_n} \tag{A.2}$$

where τ_n is the relaxation time and E_n is the Young modulus of this element. The simplest model assumes a Hookean expression for this modulus of the form $E_n \sim k_B T/R_F^2$, with $R_F \sim an^\nu$.

Let $P(n)$ be the distribution of the species n in the system. $P(n)$ is positive definite and normalized such that

$$\int_0^\infty dn\, P(n) = \mathcal{N} \tag{A.3}$$

where $\mathcal{N}$ is the total number of modes in the system. Hence, the response of the entire

system is given by

$$\sigma(t) = \int_0^\infty dn\, \sigma_n(t) = \int_0^t dt' \left[\int_0^\infty dn\, P(n)\, \tilde{E}_n\, e^{-(t-t')/\tau_n} \right] \dot{\varepsilon}(t') \tag{A.4}$$

Therefore, using the Laplace transform we come to the conclusion that the complex Young modulus is

$$E^*(\omega) = \int_0^\infty dn\, P(n)\, (i\omega)\tilde{E}_n(i\omega) \tag{A.5}$$

Then, for a generalized Maxwell model, according to the expression for the Laplace transform of a Maxwell element $\tilde{E}(s) = \frac{E}{s+1/\tau}$ one has

$$E^*(\omega) = \int_0^\infty dn\, P(n)\, \frac{i\omega E_n}{i\omega + 1/\tau_n} \tag{A.6}$$

or, what is the same separating the real and the imaginary parts,

$$E'(\omega) = \int_0^\infty dn\, P(n)\, \frac{(\omega\tau_n)^2 E_n}{1+(\omega\tau_n)^2} \tag{A.7}$$

$$E"(\omega) = \int_0^\infty dn\, P(n)\, \frac{(\omega\tau_n) E_n}{1+(\omega\tau_n)^2} \tag{A.8}$$

By construction, the expressions (A.7) and (A.8) satisfy the Kramers-Kronig relations, due to the causality of the kernel in eq. (A.1). Using the fact that τ_n is a general power law of the polymerization index of the form $a(T)n^\gamma$, the transformation $d\ln\tau_n = \gamma d\ln n$ implies that $dn = \frac{n}{\gamma} d\ln\tau$. Finally, one can define the function

$$H(n) \equiv P(n) E_n \frac{n}{\gamma} \tag{A.9}$$

to arrive at the final expression

$$E'(\omega) = \int_0^\infty d\ln\tau\, \frac{(\omega\tau)^2 H(\tau)}{1+(\omega\tau)^2} \tag{A.10}$$

$$E"(\omega) = \int_0^\infty d\ln\tau\, \frac{(\omega\tau) H(\tau)}{1+(\omega\tau)^2} \tag{A.11}$$

If one assumes that $\nu = 1/2$ and that the dynamics follows the reptation model, as it corresponds to chains in a melt, and that $E_n \sim k_B T/n$, then $H(\tau)d\ln\tau \propto k_B T P(n) dn$, namely, the function $H(\tau)$ is proportional to the spectral distribution of relaxation

times.

A.2 Operational definition of the Storage and Loss Moduli

In the following the storage and loss moduli are defined in an operational manner that allows us to obtain measurable quantities even if the response is non-linear. For completeness, we show that the definition coincides with the customary association of the storage and loss moduli in the Maxwell model.

The Hookean element can be described through a constitutive equation like

$$\sigma = E\varepsilon \tag{A.12}$$

Let us further assume that $\varepsilon = \varepsilon_0 \sin(\omega t)$. Hence, the response reads as

$$\sigma = \varepsilon_0 E \sin(\omega t) \tag{A.13}$$

We now consider the work done by the external forces on the system $dW = \sigma d\varepsilon$. Hence, the total work done by these external forces in a cycle is

$$W = \int_0^{2\pi/\omega} \sigma\dot{\varepsilon}\, dt = \omega E\varepsilon_0^2 \int_0^{2\pi/\omega} \sin(\omega t)\cos(\omega t)\, dt = 0 \tag{A.14}$$

due to the fact that this is a reversible work related to a given energy, i.e.

$$W = \int_{\varepsilon(0)}^{\varepsilon(t)} \sigma\, d\varepsilon = E \int_{\varepsilon(0)}^{\varepsilon(t)} \varepsilon\, d\varepsilon = \frac{1}{2}E(\varepsilon(t)^2 - \varepsilon(0)^2) = 0 \tag{A.15}$$

because $\varepsilon(0) = \varepsilon(t)$, and $d\varepsilon = \dot{\varepsilon}dt$.

For the case of the viscous element, the constitutive law is

$$\sigma = \eta\dot{\varepsilon} \tag{A.16}$$

and the response reads

$$\sigma = \eta\varepsilon_0\omega \cos(\omega t) \tag{A.17}$$

Hence, by evaluating the total work done in a cycle we find

$$W = \int_0^{2\pi/\omega} \sigma\dot{\varepsilon}\, dt = \eta \int_0^{2\pi/\omega} \dot{\varepsilon}^2\, dt = \eta\varepsilon_0^2\omega^2 \int_0^{2\pi/\omega} \cos^2(\omega t)\, dt = \frac{1}{2}\eta\varepsilon_0^2\omega > 0 \qquad \text{(A.18)}$$

In the presence of dissipative forces the external forcing does a positive work on the system every cycle, which eventually rises its temperature (if isolated), according to the second law of Thermodynamics.

The work done on the system in a cycle is a convenient way to discriminate the reversible and irreversible contributions. Hence, in a general case in which one has $\sigma(t)$ caused by a $\varepsilon = \varepsilon_0 \sin(\omega t)$, one can always state that

$$W = \int_0^{2\pi/\omega} \sigma(t)\dot{\varepsilon}\, dt = \int_0^{2\pi/\omega} \sigma(t)\omega\cos(\omega t)\, dt \qquad \text{(A.19)}$$

gives the dissipative contribution, the rest being reversible work recovered at the end of the cycle. Therefore, if one defines a deformation phase vector $\vec{\varepsilon}$ such that its projection along the y-axis is the deformation and its projection along the x-axis gives the phase and amplitude of $\dot{\varepsilon}/\omega$, one can split σ into two components depending on how they project onto the reversible or irreversible work. We can hence operationally define the storage and loss moduli according to

$$E''(\omega) = \frac{\int_0^{2\pi/\omega} \sigma(t)\cos(\omega t)\, dt}{\varepsilon_0/2} \qquad \text{(A.20)}$$

and analogously,

$$E'(\omega) = \frac{\int_0^{2\pi/\omega} \sigma(t)\sin(\omega t)\, dt}{\varepsilon_0/2} \qquad \text{(A.21)}$$

In the following lines we show how this can be applied to a Maxwell element. To obtain the functional form of the long-time solution of the constitutive equation,

$$\frac{\dot{\sigma}}{E} + \frac{\sigma}{\eta} = \dot{\varepsilon} \qquad \text{(A.22)}$$

let us write $\varepsilon(t) = \varepsilon_0 e^{i\omega t}$ and $\sigma(t) = \sigma_0 e^{i(\omega t+\delta)}$ and substitute it into eq. (A.22). One has,

$$\left(\frac{i\omega\sigma_0}{E} + \frac{\sigma_0}{\eta}\right) e^{i\delta} = \varepsilon_0 i\omega \qquad \text{(A.23)}$$

Equating real and imaginary parts of each member, one arrives at

$$\sigma_0(\omega) = \frac{E\varepsilon_0\omega\tau}{\sqrt{1+(\omega\tau)^2}}; \quad \tan\delta = \frac{1}{\omega\tau} \tag{A.24}$$

Therefore,

$$\sigma(t) = \sigma_0(\omega)\sin(\omega t + \delta) \tag{A.25}$$

To obtain E' and E'' we make use of eqs (A.20) and (A.21), then

$$\begin{aligned} E' &= \frac{1}{\varepsilon_0/2}\int_0^{2\pi/\omega} \mathrm{d}t\, \frac{E\varepsilon_0\omega\tau}{\sqrt{1+(\omega\tau)^2}}\sin(\omega t+\delta)\sin(\omega t) && \text{(A.26)}\\ &= \frac{E\omega\tau}{\sqrt{1+(\omega\tau)^2}}\cos\delta && \text{(A.27)}\\ E'' &= \frac{1}{\varepsilon_0/2}\int_0^{2\pi/\omega} \mathrm{d}t\, \frac{E\varepsilon_0\omega\tau}{\sqrt{1+(\omega\tau)^2}}\sin(\omega t+\delta)\cos(\omega t) && \text{(A.28)}\\ &= \frac{E\omega\tau}{\sqrt{1+(\omega\tau)^2}}\sin\delta && \text{(A.29)} \end{aligned}$$

We use $\tan\delta = 1/\omega\tau = \sin\delta/\cos\delta$, to find that

$$\cos\delta = \frac{\omega\tau}{\sqrt{1+(\omega\tau)^2}} \qquad \sin\delta = \frac{1}{\sqrt{1+(\omega\tau)^2}} \tag{A.30}$$

Finally,

$$\begin{aligned} E'(\omega) &= \frac{E\omega\tau}{\sqrt{1+(\omega\tau)^2}}\frac{\omega\tau}{\sqrt{1+(\omega\tau)^2}} = \frac{E(\omega\tau)^2}{1+(\omega\tau)^2} && \text{(A.31)}\\ E''(\omega) &= \frac{E\omega\tau}{\sqrt{1+(\omega\tau)^2}}\frac{1}{\sqrt{1+(\omega\tau)^2}} = \frac{E\omega\tau}{1+(\omega\tau)^2} && \text{(A.32)} \end{aligned}$$

q.e.d.

It is crucial to realize that the phase δ is taken with respect to ε and not to $\dot{\varepsilon}$.

A.3 Solution for the Eyring type Equation

To solve eq. (3.16) we use a dimensionless stress $\sigma^* \equiv \sigma/\sigma_v$ and time $t^* \equiv t/\tau$. We consider $\dot{\varepsilon} = 0$ for $t > 0$ since the perturbation is considered as a step function, i.e.

$\varepsilon = \varepsilon_0 \Theta(t)$, where $\Theta(t)$ is Heaviside's step function. Consequently $\dot{\varepsilon} = \varepsilon_0 \delta(t)$. Hence,

$$\dot{\sigma}^* + \sinh \sigma^* = 0 \tag{A.33}$$

We know that the final regime is given by the exponential relaxation, that is the solution of the problem for $\sigma^*(0) \ll 1$ that we have already analyzed. To study the initial nonlinear regime, let us first consider the approximation $\sigma^*(0) \gg 1$. In this case, $\sinh \sigma^* \simeq (e^{\sigma^*} - e^{-\sigma^*})/2 \simeq e^{\sigma^*}/2 \gg 1$, then

$$\dot{\sigma}^* + \frac{e^{\sigma^*}}{2} = 0 \tag{A.34}$$

that yields a solution

$$\sigma^*(t) = \sigma^*(0) - \ln\left(\frac{e^{\sigma^*(0)} t^*}{2} + 1\right) \simeq -\ln t^* \tag{A.35}$$

with $t^* < 1$. The last equality follows after an initial regime.$t^* > 2e^{-\sigma^*(0)}$. Moreover, the crossover between the nonlinear and linear regime is estimated to be given by $t^* \sim 1$, i.e., $t \sim \tau$.

On the other hand, the analytical solution of eq. (A.33) is

$$\sigma^*(t) = \ln\left(\frac{1 + \tanh(\sigma^*(0)/2) e^{-t^*}}{1 - \tanh(\sigma^*(0)/2) e^{-t^*}}\right) \tag{A.36}$$

However, to implement the model, we look for the solution when the extension (deformation) is sinusoidal. We rewrite the differential equation (3.16) in terms of the dimensionless variables, yielding

$$\frac{d\sigma^*}{dt^*} + \sinh \sigma^* = \frac{E\varepsilon_0}{\sigma_v} \omega^* \cos(\omega^* t^*) \equiv \sigma_{00}^* \omega^* \cos(\omega^* t^*) \tag{A.37}$$

with $\sigma_{00}^* \equiv E\varepsilon_0/\sigma_v$. Since we are interested in small deviations from linearity, we can consider that $\sigma_{00}^* < 1$ and propose a Taylor series for the nonlinear term up to the first correction, yielding

$$\dot{\sigma} + \sigma + \frac{\sigma^3}{3} = \sigma_{00} \omega \cos(\omega t) \tag{A.38}$$

where we have omitted the asterisk from now on, since we only work with dimensionless

variables unless explicitly indicated. We then propose a perturbative solution of the problem in terms of the small parameter σ_{00}. The zeroth order term is the solution of the linear equation, which is precisely the solution of a Maxwell element, given in eq. (A.24), with (A.23). We will neglect transient terms of the order of e^{-t} in the calculations since only the stationary solution is of our interest.

Hence, the first order correction satisfies the differential equation

$$\dot{\sigma_1} + \sigma_1 = -\frac{\sigma^3}{6} = -\frac{1}{6}\sigma_0^3(\omega)\sin^3(\omega t + \delta) \tag{A.39}$$

It is convenient to rewrite the right hand side of eq. (A.39) using the trigonometric equality

$$\sin^3(x) = \frac{1}{4}\left(3\sin(x) - \sin(3x)\right) \tag{A.40}$$

We finally write

$$\dot{\sigma_1} + \sigma_1 = -\frac{1}{24}\sigma_0^3(\omega)[3\sin(\omega t + \delta) - \sin(3(\omega t + \delta))] \tag{A.41}$$

The final solution reads

$$\sigma(t) = \sigma_0(\omega)\sin(\omega t + \delta) - \frac{1}{8}\sigma_0^3(\omega)\left(\frac{\sin(\omega t + \delta) - \omega\cos(\omega t + \delta)}{1 + \omega^2} + \frac{1}{3}\frac{\sin(3(\omega t + \delta)) - 3\omega\cos(3(\omega t + \delta))}{1 + 9\omega^2}\right) \tag{A.42}$$

The loss and storage moduli can be obtained from the integrals (A.20) and (A.21). We find

$$E' = \frac{E}{\sigma_v}\frac{(\omega\tau)^2}{1 + (\omega\tau)^2} - \frac{E^3\varepsilon_0^2}{4\sigma_v^3}\frac{(\omega\tau)^4}{(1 + (\omega\tau)^2)^3} \tag{A.43}$$

$$E'' = \frac{E}{\sigma_v}\frac{\omega\tau}{1 + (\omega\tau)^2} - \frac{E^3\varepsilon_0^2}{8\sigma_v^3}\frac{(\omega\tau)^3(1 - (\omega\tau)^2)}{(1 + (\omega\tau)^2)^3} \tag{A.44}$$

Notice that the term proportional to 3ω has no effect in the operational storage and loss moduli that can be obtained in a DMA experiment. This fact does not imply that such a harmonic response is not present in the stress but that its cumulative effect in a cycle is zero and, therefore, does not appear in the moduli. Moreover, eq. (A.43) and (A.44), as they stand, are not the representation of any causal function. This is due to the fact that the complete solution cannot be cast in a linear relationship

between stress and strain, due precisely to the cubic contribution of the stress. Hence, the operational storage and loss moduli are not the Fourier transform of a causal kernel that should comply with the causality condition, namely, having all the poles such that $i\omega > 0$. The calculation performed here, however, does respect causality and is physically flawless. The issue that we want to emphasize is that the operational moduli, including the nonlinear contribution, cannot be cast under the form of a *causal kernel* satisfying Kramers-Kronig relations because the relation between stress and strain is not linear.

A.4 Simulated Annealing Algorithm

The simulated annealing algorithm is a metaheuristic method for global optimization that introduces variations of the spectrum of relaxation-times $H(\tau)$ until the given cost function $\mathcal{E}$ reaches its minimum. The cost function used in this work is given in eq. (3.20), and is quadratic in the variables and has an absolute minimum at $\mathcal{E} = 0$. The method is close to the Monte Carlo algorithm which, from an arbitrary initial state $H_0(\tau)$, at every step a certain variation $H_{n+1} = H_n + \Delta H$ is proposed. The new state is accepted or rejected according to the Metropolis rule, namely, that it is accepted always that $\mathcal{E}_{n+1} < \mathcal{E}_n$. Moreover, if this condition is not fulfilled, still the movement can be accepted if a uniform random number $r \in (0, 1)$ is smaller than $\exp[-(\mathcal{E}_{n+1} - \mathcal{E}_n)/T_0]$, where T_0 is a scale for the permitted jumps in the cost function, which is analogous to the temperature in a physical system. Allowing uphill jumps in the cost function permits intermediate solutions to escape from local minima if they are not much deeper than T_0. Constraints, like the positiveness of $H(\tau)$, can easily be imposed during the search without having to impose the detailed balance condition, because we are not aiming at sampling the equilibrium state of a physical system. Hence, at large enough T_0 large jumps are permitted. The simulated annealing proposes a progressive decrease of T_0 during the search to reduce the height of the jumps uphill, so that the system does not escape from the minimum when close to the end. One more comment is in order: since the range of relaxation-times covers several decades and the values of the storage and loss moduli are very large, the cost function is very sensitive to variations in the region $\tau > 1/\omega_{min}$. Hence, among all the trials, we propose moves that keep

invariant one of the following moments of the relaxation-time spectrum in the long relaxation-time region at one time

$$M' = \sum_{\tau} \Delta \ln \tau H(\tau) + k \tag{A.45}$$

$$M'' = \sum_{\tau} \Delta \ln \tau \frac{H(\tau)}{\tau} \tag{A.46}$$

Then, after proposing a $\Delta H(\tau)$ for a given τ, the overall ensemble of relaxation-times is rescaled according to

$$H'(\tau) = H(\tau) \left(1 - \frac{\Delta H(\tau) \Delta \ln \tau}{\sum_{\tau} H(\tau) \Delta \ln \tau} \right) \tag{A.47}$$

when M' is selected. If M" is chosen, one imposes instead a rescaling of the form

$$H'(\tau) = H(\tau) \left(1 - \frac{\Delta H(\tau) \Delta \ln \tau}{\tau \sum_{\tau} H(\tau) \Delta \ln \tau / \tau} \right) \tag{A.48}$$

This kind of trials permits us to determine peaks located outside the more sensitive range of the spectrum, given the collection of experimental frequencies.

We checked that the procedure works rather well by creating a set of values of $E'(\omega)$ and $E''(\omega)$ from a given simple spectrum with two relaxations times $\tau_1 = 0.1$ and $\tau_2 = 12$, and the corresponding $H(\tau_1) = H(\tau_2) = 100$. Then, we used the algorithm to recover the spectrum from the values $E'(\omega)$ and $E''(\omega)$ and, as expected, the peaks of the spectrum are found to be precisely in the same position where they were previously set. In the right hand side of the spectrum, however, the original peak is $\tau_2 > 1/\omega_{min}$. The search algorithm finds the peak but lower than the original one. Moreover, it is significantly broadened.

Therefore, it is important to analyze the sensitivity of the cost function to see how the search of relaxation-times outside $1/\omega_{max} < \tau < 1/\omega_{min}$ can provide useful results. Let us calculate the variation of $\mathcal{E}$, as given in eq. (3.20), with a change in the spectrum.

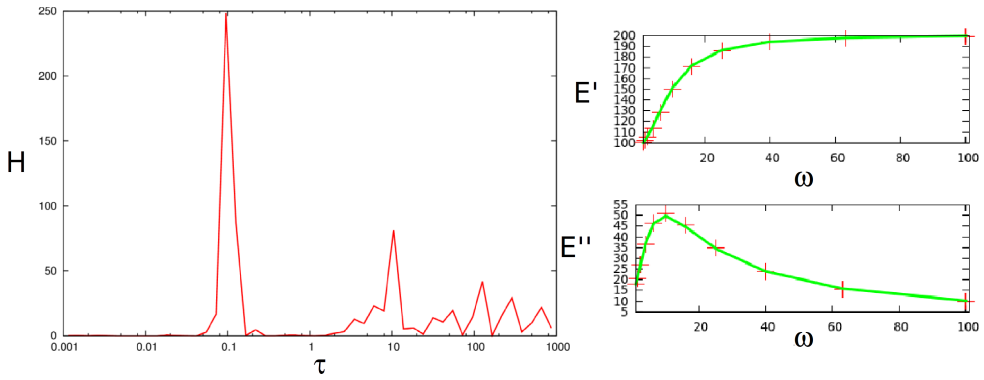

Figure A.1: *On the left-hand side, spectrum of relaxation-times for a set of data of $E'(\omega)$ and $E''(\omega)$ created to be analog to our experimental data using $E^* = \frac{i\omega\tau_1 H(\tau_1)}{1+i\omega\tau_1} + \frac{i\omega\tau_2 H(\tau_2)}{1+i\omega\tau_2}$ with $\omega \in [1, 100]$, $\tau_1 = 0.1$ and $\tau_2 = 12$, and the corresponding $H(\tau_1) = H(\tau_2) = 100$. On the right-hand side, the generated values are represented by the red crosses, while the recovered values from the model are represented by a green solid line.*

That is,

$$\Delta\mathcal{E} = \frac{\partial\mathcal{E}}{\partial H(\tau_\alpha)}\Delta H(\tau_\alpha) = \sum_\beta \left[2\left(1 - \frac{E'_\beta}{E'_{\text{exp},\beta}}\right)\frac{\Delta \ln \tau_\alpha}{E'_{\text{exp},\beta}}\frac{(\omega_\beta\tau_\alpha)^2}{1+(\omega_\beta\tau_\alpha)^2} + 2\left(1 - \frac{E''_\beta}{E''_{\text{exp},\beta}}\right)\frac{\Delta \ln \tau_\alpha}{E''_{\text{exp},\beta}}\frac{\omega_\beta\tau_\alpha}{1+(\omega_\beta\tau_\alpha)^2}\right]\Delta H(\tau_\alpha) \tag{A.49}$$

where β runs over the experimental frequencies and α indexes the relaxation-time. In the region $\tau << 1/\omega_{max}$, this expression can be cast under the form

$$\Delta\mathcal{E} = \left[A\,\tau_\alpha^2 + B\tau_\alpha\right]\Delta H(\tau_\alpha) \tag{A.50}$$

where A and B are constants, independent of the relaxation-times. Hence, the sensitivity of the cost function with the relaxation-time decreases as $\tau_\alpha \to 0$. Then, the error in the estimate of the height of $H(\tau)$ thus increases inversely proportional to $1/\tau_\alpha$. In the other side of the spectrum, $\tau_\alpha >> 1/\omega_{min}$, one has

$$\Delta\mathcal{E} = \left[C + D\frac{1}{\tau_\alpha}\right]\Delta H(\tau_\alpha) \tag{A.51}$$

In this case, the sensitivity is practically constant, independent of the relaxation-time. Thus, in this part of the spectrum the uncertainty is not in the high of $H(\tau)$ but in the location of the peaks, due to the fact that the variation of the cost function with the location of the peaks goes to zero as $1/\tau_\alpha$. These features are perfectly seen in

the obtained spectra, which are particularly flat in the large τ region, reflecting this insensitivity. In Figure A.1 we observe exactly this effect.

A.5 Asymptotic Coefficients of the Model

T(°C)	k	η	R_1'	R_2"
90	4.77×10^6	1.07×10^4	0.0013	1.37×10^3
70	1.14×10^6	2.61×10^4	0.0028	3.30×10^2
50	9.43×10^6	3.31×10^4	0.0078	1.07×10^3
30	5.98×10^7	2.99×10^4	0.0170	2.95×10^4
10	1.42×10^8	3.66×10^4	0.0216	8.02×10^4
-10	2.45×10^8	8.62×10^4	0.0260	1.09×10^5
-30	4.36×10^8	1.06×10^3	0.0386	1.75×10^5
-50	7.05×10^8	8.51×10^2	0.0317	2.08×10^5
-70	8.56×10^8	1.57×10^3	0.0606	3.79×10^5
-90	1.01×10^9	2.32×10^3	0.0916	4.92×10^5

Table A.1: *Asymptotic coefficients for the LLDPE bar as obtained from the GM model trough equation* (3.20)

T(°C)	k	η	R_1'	R_2"
90	1.67×10^8	7.45×10^4	0.0198	7.43×10^4
70	2.77×10^8	2.11×10^5	0.0496	6.46×10^4
50	6.29×10^8	2.29×10^5	0.1083	2.75×10^5
30	1.32×10^9	1.41×10^5	0.2032	6.43×10^5
10	1.58×10^9	1.85×10^5	0.1497	7.36×10^5
-10	1.79×10^9	1.52×10^5	0.2688	9.84×10^5
-30	1.95×10^9	3.50×10^4	0.1790	1.02×10^6
-50	2.22×10^9	5.34×10^3	0.2254	9.42×10^5
-70	2.53×10^9	6.34×10^3	0.2487	9.67×10^5
-90	2.74×10^9	5.26×10^3	0.1728	1.13×10^6

Table A.2: *Asymptotic coefficients for the EVOH bar as obtained from the GM model trough equation* (3.20)

T(°C)	k	η	R_1'	R_2"
90	1.85×10^{7}	4.50	0.0001	1.29×10^{4}
70	2.58×10^{7}	5.57×10^{3}	0.0075	1.08×10^{4}
50	4.08×10^{7}	3.99×10^{4}	0.0046	2.10×10^{4}
30	4.33×10^{7}	1.29×10^{5}	0.0331	2.02×10^{4}
10	6.25×10^{7}	1.04×10^{5}	0.0306	3.30×10^{4}
-10	2.33×10^{8}	1.44×10^{3}	0.0599	1.14×10^{5}
-30	7.12×10^{8}	5.16×10^{5}	0.1469	2.00×10^{5}
-50	1.25×10^{9}	4.66×10^{5}	0.1791	5.64×10^{5}
-70	1.63×10^{9}	1.36×10^{5}	0.2009	6.37×10^{5}

Table A.3: *Asymptotic coefficients for the LLDPE* $25\mu m$ *film as obtained from the GM model trough equation* (3.30)

T(°C)	k	η	R_1'	R_2"
50	3.58×10^{8}	1.64×10^{3}	0.0681	1.57×10^{5}
30	1.38×10^{9}	7.87×10^{5}	0.2896	5.38×10^{5}
10	2.65×10^{9}	2.35×10^{6}	0.4129	8.26×10^{5}
-10	2.98×10^{9}	2.77×10^{6}	0.3743	5.07×10^{5}
-30	3.73×10^{9}	2.88×10^{6}	0.5856	2.45×10^{6}
-50	4.32×10^{9}	1.61×10^{6}	0.3703	1.17×10^{6}
-70	4.90×10^{9}	1.23×10^{4}	0.5591	2.11×10^{6}

Table A.4: *Asymptotic coefficients for the EVOH* $25\mu m$ *film as obtained from the GM model trough equation* (3.30)

Appendix B

Cell Dynamics Simulation

B.1 Qualitative analysis of the system

To have an intuitive idea about the meaning of the parameters that we use in the simulations, let us address here a qualitative analysis.

The extremes of $H[\Psi]$, eq. (4.8), are given by

$$\Psi^0 = 0 \tag{B.1}$$

$$\Psi^{\pm} = -\frac{v(1-2f)}{2u} \pm \sqrt{\left(\frac{v(1-2f)}{2u}\right)^2 - \frac{\tau'}{u}} \tag{B.2}$$

Hence, the critical point is given by $\tau'_c = v^2(1-2f)^2/4u$, where the second term in (B.2) vanishes. If $\tau' < \tau'_c$, the two roots in eq. (B.2) are real and correspond to two minima of $H[\Psi]$. The third root $\Psi = 0$ corresponds to a maximum. Instead, if $\tau > \tau'_c$, only one real solution $\Psi = 0$ exists, which corresponds to a minimum. Approximately, the values of $\Psi^{\pm}$ set the relative volume occupied by each block, due to the order parameter conservation and that the integral of Ψ over the volume is zero. Hence, due to this latter fact, it has to be further required that $\tau' < 0$ to have $\Psi^+ > 0$, which is the only situation with physical meaning for the problem formulated by eq. (4.7). We consider that $\tau' < 0$ from now on. For some of the values of τ' the fields $\Psi^{\pm}$ are not in agreement with eq. (4.5). This is a drawback of the used mapping function, which should be interpreted as an expansion for small Ψ of a more complex H, in the spirit of the Ginzburg-Landau theory. However, the the free-energy functional is still physically meaningful and therefore, the simulation results are qualitatively significant. Although

one could not extract precise values of the volume fractions of each block from Ψ, the field indicates the separation between A-rich regions Ψ^- from B-rich regions Ψ^+.

Secondly, if $\tau' < 0$ the system separates into the aforementioned $A-$ and $B-$rich regions, which will take characteristic form and size. Let us consider that the system forms spheres which distribute in space in an ordered structure with a unit cell, whose lateral size d characterizes the distance between spheres. The volume of such unit cell is of the order of d^3, since prefactors are ignored along the analysis. Hence, the conservation of the order parameter implies

$$m\frac{4\pi}{3}R_s^3\Psi^+ - \left(L^3 - m\frac{4\pi}{3}R_s^3\right)|\Psi^-| \sim 0 \tag{B.3}$$

where m is the number of cells in the system and L^3 is the total volume. Hence,

$$m \sim \frac{L^3}{d^3} \tag{B.4}$$

Therefore,

$$R_s \sim d\,\rho^{1/3} \tag{B.5}$$

where we have introduced the parameter

$$\rho \equiv \left(\frac{|\Psi^-|}{\Psi^+ + |\Psi^-|}\right) \tag{B.6}$$

Therefore, the relative size of the domains of each block are determined not only by the characteristic size of the cell d, but also by the values taken by $\Psi^{\pm}$.

The scaling of the lateral dimension of the cell as well as the characteristic size of the Ψ^+ region in the model parameters is determined by the balance between the interface F_s and connectivity F_{lr} free-energy terms, since the effect of the mapping function is to cause the phase separation into two bulk phases. Thus,

$$F_s[\Psi(\vec{r})] + F_{lr}[\Psi(\vec{r})] = \int d\vec{r}\left\{\frac{D}{2}|\nabla\Psi|^2 + \frac{B}{2}\int d\vec{r}\,' G(\vec{r}-\vec{r}\,')\Psi(\vec{r})\Psi(\vec{r}\,')\right\} \tag{B.7}$$

In the strong segregation limit[90] the interface thickness between Ψ^+ and Ψ^-, namely ξ, is much smaller than the polymer size. Thus, we can derive the scaling form of the

first term F_s

$$\int d\vec{r}\frac{D}{2}|\nabla\Psi|^2 \sim D\frac{\Psi^2}{\xi^2}\xi R_s^2 m \sim DL^3\frac{\Psi^2}{\xi}\frac{\rho^{2/3}}{d} \tag{B.8}$$

where use has been made of the fact that the integrand is of the order of Ψ^2/ξ^2 and is only different from zero in the volume occupied by the interfacial region $\xi R_s^2 m = \xi R_s^2 L^3/d^3$. Eqs. (B.4) and (B.5) are also used in the last similarity. On the other hand, the second term in eq. (B.7) scales as

$$\frac{B}{2}\int d\vec{r}\int d\vec{r}\,' G(\vec{r}-\vec{r}\,')\Psi(\vec{r})\Psi(\vec{r}\,') \sim BL^3\frac{\Psi^2}{d}d^3 \sim BL^3\Psi^2 d^2 \tag{B.9}$$

where we have assumed that the outer integral is of the order of L^3 and that the inner integral of the propagator is of the order of $(\Psi^2/d)\times d^3$, since beyond d the alternation of Ψ makes its contribution to the inner integral very small. Such scaling form is independent of whether the geometry is spherical, cylindrical or lamellar, since the inner integral is dominated by the shortest distance due to the $1/r$-dependence of the integrand. Hence, using in eq. (B.7) the scaling forms of the surface and long-range contributions given, respectively, in eqs. (B.8) and (B.9), yields

$$F \sim DL^3\frac{\Psi^2}{\xi}\frac{\rho^\nu}{d} + BL^3\Psi^2 d^2 \tag{B.10}$$

with $\nu = 2/3$ for spheres. Minimizing this last equation with respect to d, one can estimate that the characteristic distance between structures scales as

$$d \sim \left(\frac{D\rho^{2/3}}{B\xi}\right)^{1/3} \equiv d_0\rho^{2/9} \tag{B.11}$$

The last equality is a definition of d_0 to highlight the dependence in ρ. Since $B \sim N^{-2}$, according to eq. (4.12), we recover the scaling $d \sim N^{2/3}$ of Ohta and Kawasaki[90], as well as the dependence in the interfacial thickness. The weak segregation limit can be recovered by realizing that the surface contribution scales as $B\Psi^2L^3/d^2$ since the interfacial thickness is $\xi \sim d$ itself. Thus, in this latter case we also recover the scaling form for the weak segregation limit $d \sim (D\rho^{2/3}/B)^{1/4} \sim N^{1/2}$[74]. We will only consider the strong segregation limit from now on.

Repeating the calculation but assuming that the system arranges in parallel cylin-

ders, one also finds an estimate of the radius R_c of the cylinder $R_c \sim d\,\rho^{1/2}$, and the exponent $\nu = 1/3$. d is found to scale as

$$d \sim \left(\frac{D\rho^{1/2}}{B\xi}\right)^{1/3} = d_0\rho^{1/6} \tag{B.12}$$

Similarly, lamellae thickness is given by the relation $R_l \sim d\,\rho$ and $\nu = 0$. Then

$$d \sim \left(\frac{D}{B\xi}\right)^{1/3} = d_0 \tag{B.13}$$

Notice that the scaling law $N^{2/3}$ is the same as for the spherical case for both cylinders and lamellae[90].

The scaling analysis cannot predict the relative stability of the different structures, which can be found in[90], due to the importance of the neglected prefactors. However, inserting the obtained scaling forms of d, given in eqs. (B.11), (B.12), and (B.13) into the scaling form of the free energy, one obtains

$$F \sim \Psi^2 L^3 B d_0^2\,\rho^{\mu} \tag{B.14}$$

with $\mu = 4/9 \simeq 0.44$, for spheres, $\mu = 1/3 \simeq 0.33$ for cylinders and $\mu = 0$ for lamellae. Hence, the value of the exponent μ indicates that low values of ρ will favor the formation of spheres, while values close to 1 will produce lamellae, with a transition to cylinders in between. Although the analysis is qualitative, it gives an idea about the role played by the parameters of the model under study. These results are in agreement with the detailed analysis of the phase diagram given in ref.[90]. Moreover, eq. (B.14) also qualitatively explains why within our model and parameters annealing produces cylinders early in the evolution while quenching produces directly spheres.

B.2 Euclidean distance between structures

In order to perform a quantitative analysis of the obtained structures, we introduce an Euclidean distance between the local environment of spheres and two relevant patterns for our system. Focusing on the 2D arrangements, these ideal patterns are the hexagonal (HEX) arrangement and a (110)-plane of a body-centered cube (BCC) distribution. In

Figure B.1 we sketch two layers of spheres arranged according to these two structures

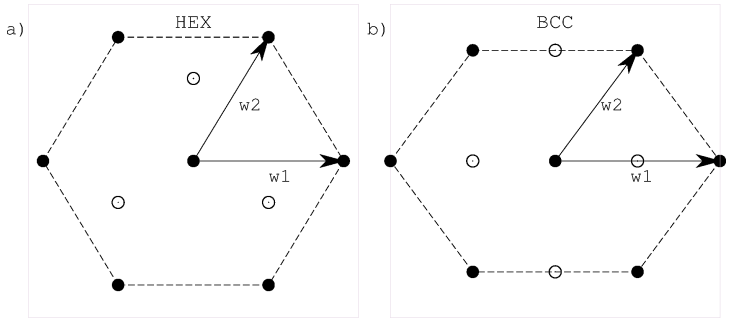

Figure B.1: *Characteristic distribution of spheres; (a): hexagonal symetry, (b): (110)-plane of a BCC symetry. The central sphere with the six coplanar nearest-neighbors are represented by filled circles, while the nearest neighbors of the adjacent layer are represented by open circles.*

To evaluate such a Euclidean distance, we proceed as follows. For each sphere we identify its center and the ones of its 6 nearest-neighbors within the same plane, parallel to the surface, and containing the center of the former (within a tolerance of 4 lattice spacings, corresponding to a half sphere radius up and down its center). To locate these centers we have used a method based on a large collection of code-vectors, which dynamically move down the gradient of Ψ to cluster around the points of low $\Psi \simeq \Psi^{-}$. Then, a clustering identification based on the closeness of the code-vectors permits to discriminate the code-vectors belonging to each domain and assign a centroid to it. Cylinders on the bottom wall are excluded.

The positions of the 6 neighbors' centers with respect to the central sphere's center define a 18-dimensional vector $\vec{v}$ describing the local structure of the central domain. The distance between two of these structures, namely $\vec{v} = (\vec{v}_1, \vec{v}_2, \ldots, \vec{v}_6)$ and $\vec{a} = (\vec{a}_1, \vec{a}_2, \ldots, \vec{a}_6)$, is simply defined as

$$\Delta^2(\vec{v}, \vec{a}) = \sum_{k=1}^{6}{}' \sum_{\alpha=x,y,z} (v_{\alpha,perm(k)} - a_{\alpha,k})^2 \tag{B.15}$$

The prime stands for the fact that a given ordering of the vectors of one of the structures (say $\vec{v}$) is implied. The ordering is defined by simultaneously rotating the six 3D vectors of $\vec{v}$ until $\vec{v}_1$ is parallel to $\vec{a}_1$. Then, we calculate all permutations of the identifiers of the remaining vectors $perm(k)$, to compare with the set $\vec{a} = (\vec{a}_1, \vec{a}_2, \ldots, \vec{a}_6)$, which contains a fixed ordering of the vectors. We further calculate $\Delta_{perm(k)}$ for each permutation. We repeat the operation rotating again the initial structure but now aligning $\vec{v}_2$ with $\vec{a}_1$

and calculating the permutations of all remaining vectors and the associated distances. After the rotation of all six vectors, Δ is taken as the minimum of all the calculated Δ's. This procedure is intended to remove any bias in the identification of who is who when comparing two structures.

The norm of $\vec{v}$ is defined as

$$||\vec{v}||^2 \equiv \sum_{k=1}^{6} \sum_{\alpha=x,y,z} v_\alpha^2 \tag{B.16}$$

To calculate the distance according to eq. (B.15), $\vec{v}$ has been previously normalized such that $||\vec{v}|| = \sqrt{6}$, which is the norm of the HEX and BCC patterns as we have defined them in Table 1.

A pattern is thus also defined as a 18-dimensional vector whose norm, from eq. (B.16) is taken to be 6 by definition. The two planar patterns considered are defined by the six positions given in Figure B.1.

Hence, the distance between the obtained local structure and the HEX (or BCC) pattern is calculated as $\Delta(\vec{v}, \vec{w})$ where the vectors $\vec{w}$ defining the pattern are given in Table B.1.

	HEX			BCC		
	x	y	z	x	y	z
$a_1\,\mathcal{N}$	1	0	0	1	0	0
$a_2\,\mathcal{N}$	$1/2$	$\sqrt{3}/2$	0	$1/2$	$1/\sqrt{2}$	0
$a_3\,\mathcal{N}$	$-1/2$	$\sqrt{3}/2$	0	$-1/2$	$1/\sqrt{2}$	0
$a_4\,\mathcal{N}$	-1	0	0	-1	0	0
$a_5\,\mathcal{N}$	$-1/2$	$-\sqrt{3}/2$	0	$-1/2$	$-1/\sqrt{2}$	0
$a_6\,\mathcal{N}$	$1/2$	$-\sqrt{3}/2$	0	$1/2$	$-1/\sqrt{2}$	0

Table B.1: *Characteristic vectors defining a hexagonal arrangement (HEX) and a (110)-plane of a body-centered cubic (BCC) arrangement. $\mathcal{N}$ is the norm of the 18-dimensional vector, according to eq.* (B.16)*, divided by $\sqrt{6}$. For the HEX $\mathcal{N} = 1$, while for the BCC $\mathcal{N} = \sqrt{5/6}$*

Bibliography

[1] H. Abe, Y. Kikkawa, T. Iwata, H. Aoki, T. Akehata, and Y. Doi. *Polymer*, 41:867, 2000.

[2] M. Alcoutlabi and J.J. Martinez-Vega. *Polymer*, 44(23):7199 – 7208, 2003.

[3] D.E. Angelescu, C.K. Harrison, M.L. Trawick, R.A. Register, and P.M. Chaikin. *Phys. Rev. Lett.*, 95:025702, 2005.

[4] A.C. Arsenault, D.A. Rider, N. Ttreault, J.I.L. Chen, N. Coombs, G. A. Ozin, and I. Manners. *Journal of the American Chemical Society*, 127(28):9954–9955, 2005. PMID: 16011331.

[5] E. Baer, A. Hiltner, and H.D. Keith. *Science*, 235(4792):1015–1022, 1987.

[6] E. Baer, A. Hiltner, and R. Morgan. *Physics Today*, 45:60–67, October 1992.

[7] M. Bahiana and Y. Oono. *Phys. Rev. A*, 41:6763, 1990.

[8] F. S. Bates and G. H. Fredrickson. *Annu. Rev. Phys. Chem*, 41:525, 1990.

[9] M. Baumgaertel and H.H. Winter. *Rheologica Acta*, 28(6):511–519, 1989.

[10] M. Baumgaertel and H.H. Winter. *Journal of Non-Newtonian Fluid Mechanics*, 44(0):15 – 36, 1992.

[11] T.E. Bernal-Lara, R.Y.F. Liu, A. Hiltner, and E. Baer. *Polymer*, 46:3043, 2005.

[12] T.E. Bernal-Lara, R. Masirek, A. Hiltner, E. Baer, E. Piorkowska, and A. Galeski. *J. Appl. Polym. Sci.*, 99:597, 2006.

[13] R.B. Bird, R.C. Armstrong, and O. Hassager. *Dynamics of Polymeric Liquids*. John Wiley and Sons, 1987.

[14] I. Bita, J. K. W. Yang, Y. S. Jung, C. A. Ross, E. L. Thomas, and K. K. Berggren. *Science*, 321:939, 2008.

[15] A. W. Bosse, C. J. Garcia-Cervera, and G. H. Fredrickson. *Macromolecules*, 40:9570, 2007.

[16] R.H. Boyd. *Macromolecules*, 17(4):903–911, 1984.

[17] R.H. Boyd. *Polymer*, 26:1123, 1985.

[18] R.H. Boyd. *Polymer*, 26:323, 1985.

[19] S. A. Brazovskii. *Sov. Phys. JETP*, 41:85, 1975.

[20] M.L. Cerrada, J.M. Pereña, R. Benavente, and E. Perez. *Polymer*, 41:6655, 2000.

[21] A. Chakrabarti and H. Chen. *Journal of Polymer Science: Part B: Polymer Physics*, 36:3127, 1998.

[22] L. Q. Chen and J. Shen. *Computer Physics Communications*, 108:147, 1998.

[23] P. Chen, H. Liang, R. Xia, J. Qian, and X. Feng. *Macromolecules*, 46(3):922–926, 2013.

[24] W.Q. Chen, H. Wei, S.L. Li, J. Feng, J. Nie, X.Z. Zhang, and R.X. Zhuo. *Polymer*, 49:3965, 2008.

[25] K. Cho, D. Kim, and S. Yoon. *Macromolecules*, 36:7652, 2003.

[26] V.P. Chuang, J.Y. Cheng, T.A. Savas, and C.A. Ross. *Nano Letters*, 6(10):2332–2337, 2006.

[27] J.C. Coburn and R.H. Boyd. *Macromolecules*, 19(8):2238–2245, 1986.

[28] P.G. De Gennes. *Scaling Concepts in Polymer Physics*. Cornell University Press, 1979.

[29] R. Diaz-Calleja, A. Garcia-Bernabe, M.J. Sanchis, and L.F. Del Castillo. *Phys Rev E*, 72:051505, 2005.

[30] P. Dobriyal, H. Xiang, M. Kazuyuki, J.T. Chen, H. Jinnai, and T. P. Russell. *Macromolecules*, 42:9082–9088, 2009.

[31] M. Doi and S.F. Edwards. *The Theory of Polymer Dynamics*. Oxford University Press, 1988.

[32] F. Drolet and G.H. Fredrickson. *Phys. Rev. Lett.*, 83:4317–4320, 1999.

[33] J.C. Dyre. *Phys. Rev. E*, 48:400–407, Jul 1993.

[34] E.W. Edwards, M. Mller, M.P. Stoykovich, H.H. Solak, J.J. de Pablo, and P.F. Nealey. *Macromolecules*, 40(1):90–96, 2007.

[35] I. Emri and N.W. Tschoegl. *International Journal of Solids and Structures*, 32(67):817 – 826, 1995. Time Dependent Problems in Mechanics.

[36] M. J. Fasolka and A. M. Mayes. *Ann. Rev. Mat. Res.*, 31:323, 2001.

[37] J. Feng, H. Liu, and Y. Hu. *Macromol. Theory Simul.*, 11:549, 2002.

[38] J. Feng, H. Liu, and Y. Hu. *Macromol. Theory Simul.*, 11:556, 2002.

[39] J. Feng and E. Ruckenstein. *J. Chem. Phys.*, 121:1609, 2004.

[40] J.D. Ferry. *Viscoelastic Properties of Polymers*. John Wiley and Sons, 1980.

[41] G.H. Fredrickson. *Macromolecules*, 20(10):2535–2542, 1987.

[42] G.H. Fredrickson and E. Helfand. *The Journal of Chemical Physics*, 87(1):697–705, 1987.

[43] U.W. Gedde and A. Mattozzi. *Adv. Polym. Sci.*, 169:29, 2004.

[44] S.R. De Groot and P. Mazur. *Phys. Rev.*, 94:218–224, 1954.

[45] I. W. Hamley. *The Physics of Block Copolymers*. Oxford University Press, (Oxford), 1998.

[46] I. W. Hamley. *Macromol. Theory Simul.*, 9:363, 2000.

[47] I. W. Hamley. *Nanotechnology*, 14:R39–R54, 2003.

[48] I. W. Hamley. *Progress in Polymer Science*, 34:1161–1210, 2009.

[49] S. Havriliak and S. Negami. *Polymer*, 8(0):161 – 210, 1967.

[50] N. Heymans. *Signal Processing*, 83:2345, 2003.

[51] J. Honerkamp and J. Weese. *Rheologica Acta*, 32(1):65–73, 1993.

[52] E. Huang, T. P. Russell, C. Harrison, P. M. Chaikin, R. A. Register, C. J. Hawker, and J. Mays. *Macromolecules*, 31:7641, 1998.

[53] S. M. Hur, C. J. Garcia-Cervera, E. J. Kramer, and G. H. Fredrickson. *Macromolecules*, 42:5861, 2009.

[54] K.H. Illers. *Koll. Z. Z. Polym.*, 251:394, 1973.

[55] M. Jakobsen and J. Risbo. *Packag. Technol. Sci.*, 21:207, 2008.

[56] D. Jarus, A. Hiltner, and E. Baer. *Polymer*, 43(8):2401 – 2408, 2002.

[57] K. Jeon and R. Krishnamoorti. *Macromolecules*, 41:7131, 2008.

[58] S. Ji, U. Nagpal, W. Liao, C.C. Liu, J.J. de Pablo, and P.F. Nealey. *Advanced Materials*, 23(32):3692–3697, 2011.

[59] Y. Jin, M. Rogunova, A. Hiltner, E. Baer, R. Nowacki, A. Galeski, and E. Piorkowska. *J. Polym. Sci. Pol. Phys.*, 42:3380, 2004.

[60] S. Kalakkunnath, D.S. Kalika, H. Lin, and B.D. Freeman. *Journal of Polymer Science Part B: Polymer Physics*, 44(15):2058–2070, 2006.

[61] G. J. Kellogg, D. G. Walton, A. M. Mayes, P. Lambooy, T. P. Russell, P. D. Gallagher, and S. K. Satija. *Phys. Rev. Lett.*, 76:2503, 1996.

[62] H. Kim, E. S. Daniels, S. Li, V. K. Mokkapati, and K. Kardos. *Journal of Polymer Science: Part A: Polymer Chemistry*, 45:1038–1054, 2007.

[63] H.C. Kim and W.D. Hinsberg. *Journal of Vacuum Science & Technology A*, 26(6):1369–1382, 2008.

[64] J.K. Kim, S.Y. Yang, Y. Lee, and Y. Kim. *Progress in Polymer Science*, 35(11):1325 – 1349, 2010.

[65] S. O. Kim, H. H. Solak, M. P. Stoykovich, N. J. Ferrier, J. J. Pablo, and P. F Nealey. *Nature*, 424:411, 2003.

[66] A. Knoll, A. Horvat, K. S. Lyakhova, G. Krausch, G. J. A. Sevink, A. V. Zvelindovsky, and R. Magerle. *Phys. Rev. Lett.*, 89(3):035501, JUL 15 2002.

[67] S. Komura, J.-I. Fukuda, and G. C. Paquette. *Phys. Rev. E*, 53:R5588, 1996.

[68] N. Koneripalli, R. Levicky, F.S. Bates, J. Ankner, H. Kaiser, and S.K. Satija. *Langmuir*, 12(26):6681–6690, 1996.

[69] E.J. Kramer. *Nature*, 437:824–825, 2005.

[70] D.W. Van Krevelen and K. Te Nijenhuis. Chapter 13 - mechanical properties of solid polymers. In D.W. Van KrevelenRevised by and K. Te Nijenhuis, editors, *Properties of Polymers (Fourth Edition)*, pages 383 – 503. Elsevier, Amsterdam, fourth edition edition, 2009.

[71] Y.A. Kriksin, I.V. Neratova, P.G. Khalatur, and A.R. Khokhlov. *Chemical Physics Letters*, 492(13):103 – 108, 2010.

[72] C. Lai, R. Ayyer, A. Hiltner, and E. Baer. *Polymer*, 51:1820, 2010.

[73] H. Leaderman. *Industrial & Engineering Chemistry*, 35(3):374–378, 1943.

[74] L. Leibler. *Macromolecules*, 13:1602, 1980.

[75] W. Li, F. Qiu, Y. Yang, and A.-C. Shi. *Macromolecules*, 43:1644, 2010.

[76] W. Li, N. Xie, F. Qiu, Y. Yang, and A.-C. Shi. *J. Chem. Phys.*, 134:144901, 2011.

[77] C.C. Liu, A. Ramirez-Hernandez, E. Han, G.S.W. Craig, Y. Tada, H. Yoshida, H. Kang, S. Ji, P. Gopalan, J. J. de Pablo, and P.F. Nealey. *Macromolecules*, 46(4):1415–1424, 2013.

[78] G. Liu, F. Detcheverry, A. Ramirez-Hernandez, H. Yoshida, Y. Tada, J.J. de Pablo, and P.F. Nealey. *Macromolecules*, 45(9):3986–3992, 2012.

[79] R.Y.F. Liu, T.E. Bernal-Lara, A. Hiltner, and E. Baer. *Macromolecules*, 38:4819, 2005.

[80] R.Y.F. Liu, A.P. Ranade, H.P. Wang, T.E. Bernal-Lara, A. Hiltner, and E. Baer. *Macromolecules*, 38:10721, 2005.

[81] J. F. Marko. *Phys. Rev. E*, 48:2861, 1993.

[82] M.W. Matsen. *J. Chem. Phys.*, 106:7781, 1997.

[83] M.W. Matsen and F.S. Bates. *Macromolecules*, 29(4):1091–1098, 1996.

[84] K.P. Menard. *Dynamic Mechanical Thermal Analysis. In Encyclopedia of Chemical Processing.* Taylor and Francis: New York, Published online, 2007.

[85] C.D. Mueller, S. Nazarenko, T. Ebeling, T.L. Schuman, A. Hiltner, and E. Baer. *Polym. Eng. Sci.*, 37:355, 1997.

[86] M. Mueller and D.W. Sun. *Phys. Rev. Lett.*, 111:267801, 2013.

[87] O.K. Muratoglu, A.S. Aron, and R.E. Cohen. *Polymer*, 36:2143, 1995.

[88] K.H. Nitta and A. Tanaka. *Polymer*, 42:1219, 2001.

[89] T. Ohta, Y. Enomoto, J. L. Harden, and M. Doi. *Macromolecules*, 26:4928, 1993.

[90] T. Ohta and K. Kawasaki. *Macromolecules*, 19:2621, 1986.

[91] Y. Oono and S. Puri. *Phys. Rev. Lett.*, 58:836, 1987.

[92] F.J. Padden and H.D. Keith. *J. Appl. Phys.*, 37:4013, 1966.

[93] S.J. Pan, J. Im, M.J. Hill, A. Keller, A. Hiltner, and E. Baer. *J. Polym. Sci. Pol. Phys.*, 28:1105, 1990.

[94] C. Park, J. Yoon, and E. L. Thomas. *Polymer*, 44:6725, 2003.

[95] M. Park, C. Harrison, P. M. Chaikin, R. A. Register, and D.H. Adamson. *Science*, 276:1401, 1997.

[96] S.M. Park, Go.S.W. Craig, Y.H. La, and P.F. Nealey. *Macromolecules*, 41(23):9124–9129, 2008.

[97] S.M. Park, G.S. W. Craig, Y.H. La, H.H. Solak, and P.F. Nealey. *Macromolecules*, 40:5084, 2007.

[98] D. Petera and M. Muthukumar. *The Journal of Chemical Physics*, 109(12):5101–5107, 1998.

[99] V. V. Pethe, H. P. Wang, A. Hiltner, E. Baer, and B. D. Freeman. *Journal of Applied Polymer Science*, 110(3):1411–1419, 2008.

[100] M. Pinna, A. V. Zvelindovsky, X Guo, and C. L. Stokes. *Soft Matter*, 7:6991, 2011.

[101] M. Pinna and A.V. Zvelindovsky. *European Physics Journal B*, 85:210, 2012.

[102] M. Pinna, A.V. Zvelindovsky, S. Todd, and G. Goldbeck-Wood. *J. Chem. Phys.*, 125(15):154905, OCT 21 2006.

[103] M. Ponting, A. Hiltner, and E. Baer. *Macromol. Symp.*, 294:19, 2010.

[104] W.H. Press, S.A. Teukolsky, W.T. Vetterling, and Flannery B.P. *Numerical Recipes in Fortran 77: The Art of Scientific Computing*. Cambridge University Press, Cambridge, 2nd edition, 1992.

[105] S. Qi and Z.-G. Wang. *Phys. Rev. E*, 55:1682, 1997.

[106] A. Ramirez-Hernandez, G. Liu, P.F. Nealey, and J.J. de Pablo. *Macromolecules*, 45(5):2588–2596, 2012.

[107] S. R. Ren, I. W. Hamley, P. I. C. Teixeira, and P. D. Olmsted. *Phys. Rev. E*, 63:041503, 2001.

[108] S.R. Ren and I.W. Hamley. *Macromolecules*, 34:116, 2001.

[109] S.R. Ren, I.W. Hamley, G.J.A. Sevink, A.V. Zvelindovsky, and J.G.E.M. Fraaije. *Macromol. Theory Simul.*, 11:123, 2002.

[110] L. Rockford, Y. Liu, P. Mansky, T. P. Russell, M. Yoon, and S. Mochrie. *Physical Review Letter*, 82:2602, 1999.

[111] F. Rodriguez, C. Cohen, C.K. Ober, and L. Archer. *Principles of Polymer Systems*. Taylor & Francis, 5th edition, 2003.

[112] R. Ruiz, H. Kang, F. A. Detcheverry, E. Dobisz, D. S. Kercher, T. R.Albrecht, J. J. de Pablo, and P. F. Nealey. *Science*, 321:936, 2008.

[113] A. Sanz, A. Nogales, T.A. Ezquerra, W. Hussler, M. Soccio, N. Lotti, and A. Munari. *Macromolecules*, 44(20):8124–8128, 2011.

[114] H. Schiessel, R. Metzler, A. Blumen, and T. F. Nonnenmacher. *Journal of Physics A: Mathematical and General*, 28(23):6567, 1995.

[115] T. Schuman, S. Nazarenko, E.V. Stepanov, S.N. Magonov, A. Hiltner, and E. Baer. *Polymer*, 40(26):7373 – 7385, 1999.

[116] R. Segalman, H. Yokoyama, and Kramer E. *Advanced Materials*, 13:1152–1155, 2001.

[117] R.A. Segalman. *Material Science and Enginering R*, 48:191, 2005.

[118] R.A. Segalman, A. Hexemer, and E.J. Kramer. *Physical Review Letter*, 91:196101, 2003.

[119] D. K. Setua, Y. N. Gupta, S. Kumar, R. Awasthi, A. Mall, and K. Sekhar. *Journal of Applied Polymer Science*, 100(1):677–683, 2006.

[120] A.C. Shi and B. Li. In Krzysztof Matyjaszewski and Martin Mller, editors, *Polymer Science: A Comprehensive Reference*, pages 71 – 81. Elsevier, Amsterdam, 2012.

[121] K. Shin, H. Xiang, S. I. Moon, T. Kim, T. J. McCarthy, and T. P. Russell. *Science*, 306:76, 2004.

[122] A. Shinozaki and Y. Oono. *Phys. Rev. E*, 48:2622, 1993.

[123] L.H. Sperling. *Introduction to Physical Polymer Science*. John Wiley and Sons, 2nd edition, 1992.

[124] F.C. Stehling and L. Mandelkern. *Macromolecules*, 3(2):242–252, 1970.

[125] G. E. Stein, E. W. Cochran, K. Katsov, G. H. Fredrickson, E. J. Kramer, X. Li, and J. Wang. *Phys. Rev. Lett*, 98:158302, 2007.

[126] G.E. Stein, E.J. Kramer, X. Li, and J. Wang. *Macromolecules*, 40(7):2453–2460, 2007.

[127] Y. Tada, S. Akasaka, H. Yoshida, H. Hasegawa, E. Dobisz, D. Kercher, and M. Takenaka. *Macromolecules*, 41(23):9267–9276, 2008.

[128] T. Thurn-Albrecht, J. Schotter, G. Kastle, N. Emley, T. Stubauchui, L. Krusin-Elbaum, C. Black, M. Tuominen, and T. Russell. *Science*, 290:2126, 2000.

[129] A. Tobolsky and H. Eyring. *The Journal of Chemical Physics*, 11(3):125–134, 1943.

[130] A.V. Tobolsky and R. D. Andrews. *The Journal of Chemical Physics*, 13(1):3–27, 1945.

[131] A.V. Tobolsky and K. Murakami. *Journal of Polymer Science*, 40(137):443–456, 1959.

[132] D.M. Trombly, V. Pryamitsyn, and V. Ganesan. *The Journal of Chemical Physics*, 134(15), 2011.

[133] D. A. Vega, C. K. Harrison, D. E. Angelescu, M. L. Trawick, D. A. Huse, P. M. Chaikin, and R. A. Register. *Phys. Rev. E*, 71:061803, 2005.

[134] H. Wang, J.K. Keum, A. Hiltner, E. Baer, B. Freeman, A. Rozanski, and A. Galeski. *Science*, 323(5915):757–760, 2009.

[135] Q. Wang. *Nanostructured Soft Matter*. A. V. Zvelindovsky Ed., Springer, Dordrecht, 2007.

[136] Y. Wang, Y. Qin, A. Berger, E. Yau, C. He, L. Zhang, U. Gsele, M. Knez, and M. Steinhart. *Advanced Materials*, 21(27):2763–2766, 2009.

[137] I.M. Ward and D.W. Hadley. *An Introduction to the Mechanical Properties of Solid Polymers*. John Wiley & Sons, Inc., New York, 1993.

[138] H.H. Winter. *Journal of Non-Newtonian Fluid Mechanics*, 68(23):225 – 239, 1997. Papers presented at the Polymer Melt Rheology Conference.

[139] M.W. Wu, R. A. Register, and P. M. Chaikin. *Phys. Rev. E*, 74:040801(R), 2006.

[140] Y. Wu, G. Chen, K. Katsov, S. W. Sides, J. Wang, J. Tang, G. H. Fredrickson, M. Moskovits, and G. D. Stucky. *Nature Materials*, 3:816, 2004.

[141] S. Xiao, X. Yang, S. Park, D. Weller, and T.P. Russell. *Advanced Materials*, 21(24):2516–2519, 2009.

[142] J. Xu, S. Park, S. Wang, T.P. Russell, B.M. Ocko, and A. Checco. *Advanced Materials*, 22:2268, 2010.

[143] G. Yang, P. Tang, Y. Yang, and J.T. Cabral. *The Journal of Physical Chemistry B*, 113(43):14052–14061, 2009.

[144] X.M. Yang, R.D. Peters, P.F. Nealey, H.H. Solak, and F. Cerrina. *Macromolecules*, 33(26):9575–9582, 2000.

[145] B.J. Ye, X.and Edwards and B. Khomami. *Macromolecules*, 43(23):9594–9597, 2010.

[146] X. Ye, B.J. Edwards, and B. Khomami. *Macromolecular Rapid Communications*, 33(5):392–395, 2012.

[147] H. Yokoyama, T.E. Mates, and E.J. Kramer. *Macromolecules*, 33(5):1888–1898, 2000.